ABSTRACT

SIMPSON, JIM A. Underwater Free-Space Optical Communication Using Smart Transmitters and Receivers. (Under the direction of John Muth.)

The number of unmanned vehicles and devices deployed underwater is rapidly increasing. Present underwater systems are acoustic and have relatively limited bandwidth. Underwater free-space optical communication is poised to augment acoustic communication underwater, and to provide high-bandwidth, short-range wireless links. Most underwater optical systems are point to point links with relatively strict pointing and tracking requirements. New communication strategies and networking protocols have the potential to greatly expand the capability to communicate between multiple mobile underwater platforms in water of varying quality.

In this research, compact smart transmitters and receivers for underwater free-space optical communications are demonstrated. The receivers have a segmented wide field of view and are capable of estimating angle of arrival of signals. The transmitters are highly directional with individually addressable light emitting diodes for electronic switched beam steering, and can estimate water quality from the backscattered light collected by a co-located receiver. Together, they form enabling technologies for non-traditional networking schemes in swarms of unmanned vehicles underwater.

Some of the contributions of this dissertation that can be leveraged to improve the performance of underwater free-space optical communication systems are:

1. The use of smart transmitters and receivers to show that strict pointing and tracking requirements typically associated with underwater free-space optical communication can be relaxed. This is a benefit to power and volume limited underwater vehicles.

2. The use of segmented field of view and electronic beam steering that enable the ability to obtain angle of arrival information. This information used with code division multiple access techniques allow the relative position and pose between systems to be obtained, as well as identify the platforms. This allows improved ability to communicate in the presence of other optical signals in a multi-platform environment.

3. Estimation of water quality from backscatter measurements to provide information about the underwater optical channel and to provide information for the system to adapt to a changing environment.

4. Some circuit implementations of how to implement smart transmitters and receivers, including a new digital to analog converter based bias-tee that shows an improved method of driving multiple diode lasers and light emitting diodes at high currents.

© Copyright 2012 by Jim A. Simpson

All Rights Reserved

Underwater Free-Space Optical Communication Using Smart Transmitters and Receivers

by
Jim A. Simpson

A dissertation submitted to the Graduate Faculty of
North Carolina State University
in partial fulfillment of the
requirements for the Degree of
Doctor of Philosophy

Electrical Engineering

Raleigh, North Carolina

2012

APPROVED BY:

Leda Lunardi	Brian Hughes
Edward Grant	John Muth Chair of Advisory Committee

DEDICATION

To Rhea.

BIOGRAPHY

Jim Simpson received the B.S. degree and M.S. degree in electrical engineering from North Carolina State University, Raleigh, NC, in 2006 and 2007, respectively. In January 2008 he began working towards his Ph.D. in electrical engineering at North Carolina State University under the advisement of Prof. John F. Muth. His research interests include digital communication systems and underwater optical communications. Upon completion of his Ph.D. studies he will begin his professional career at Northrop Grumman in their Future Technical Leaders program.

ACKNOWLEDGEMENTS

First and foremost, I would like to thank my advisor, Prof. John Muth, for his guidance and support throughout my graduate school career. I have tremendously benefited from his wisdom, vision, instruction, and friendship. I count myself fortunate to have his mentorship and valuable feedback, especially during endeavors in unconventional thinking. Much of the multidisciplinary approach of this dissertation was made possible through the numerous discussions with my committee members, Profs. Leda Lunardi, Brian Hughes, and Edward Grant. I owe much for each of their continued support towards this dissertation.

I've had the unique opportunity of sharing my Bachelor's, Master's, and Ph.D. journey with my lab-mate, best friend, and surrogate brother, William Cox, who will always be an unparalleled source of support and inspiration. I couldn't have done it without you either. I would also like to thank his wife, Jamie, for all her support and for feeding me healthy food.

Mike Faircloth, Chris Altman, Kory Gray, John Krier, Kevin Wolf, Carlo Domizioli, and Jared Everett, have all, either directly through assisting in research, or outside of research, or both, kept me sane through graduate school. I thank each of them for their continuous support and encouragement. I have also always enjoyed working with all of the past and current members of the NC State Underwater Robotics Club. Their support has been immeasurable and will always be remembered.

I am thankful for the support of Brandon Cochenour and Linda Mullen at Patuxent River Naval Air Station for valuable insight from discussions and laboratory experiments in their test tank. I would also like to thank Will Rabinovich and Rita Mahon at Naval Research Lab for discussions and advice. I have also appreciated discussions with Norm Farr, Jon Ware, and Cliff Pontbriand at Woods Hole Oceanographic Institute.

This dissertation would not have been possible without the love, encouragement, prayers and support of my dad and mom, as well as all of my family. They have instilled in me, all of the qualities that I have drawn from during the many years in graduate school, that has resulted in this dissertation. I thank my brother, Joe Simpson, for always motivating me to be the best that I can be. I am also grateful for my in-laws for countless meals, prayers, and support.

It is also safe to say that, without the sustained effort of my wife Rhea, this dissertation would not exist. Coping with the frustrations of being a Ph.D. spouse has to be trying on the strongest of marriages, yet she strongly supported us both, while maintaining her successful career, all the while being long distance. This dissertation is dedicated to her.

I thank God for giving me wisdom and guidance throughout my life and for his grace and mercy he has blessed us with. I thank him for all the wonderful people He has placed in my life and for their fellowship, prayers, and support.

TABLE OF CONTENTS

List of Tables . . . . . **vii**

List of Figures . . . . . **viii**

Chapter 1 Introduction **1**
1.1 Benefits of Smart Optical Systems 4
1.2 Major Contributions 7
1.3 Overview of Dissertation 7

Chapter 2 Background **9**
2.1 Related Research in Underwater Free-Space Optical Communication 10
2.2 Related Research in Indoor Optical Wireless Communication 12
2.3 The Underwater Optical Channel: Optical Properties of Water 13
2.3.1 Inherent Optical Properties 15
2.3.2 Apparent Optical Properties 18
2.4 The Underwater Optical Channel: Optically Significant Constituents of Water . . 20
2.4.1 Optically Significant Constituents 20
2.4.2 Particle Size Distributions 21
2.5 The Underwater Optical Channel: Electromagnetic Properties of Water 23
2.5.1 Absorption 24
2.6 Link Budget 27
2.6.1 Transmitter to Receiver 27
2.6.2 At the Receiver 28

Chapter 3 Design and Prototype of Smart Transmitters and Receivers **31**
3.1 Design Goals 31
3.1.1 Geometrical Loss in Link Budget 31
3.1.2 Field of View and Pointing 32
3.1.3 Existing Systems and Methods 34
3.2 Smart Receiver 35
3.2.1 Design and Conceptual Operation 35
3.2.2 Design Considerations 35
3.3 Smart Transmitter 39
3.3.1 Design and Conceptual Operation 39
3.3.2 CDMA Coding 39
3.4 Multi-Channel Front-End Electronics 42
3.4.1 Smart Receiver Multi-Channel Front-End Electronics 42
3.4.2 7-Channel Receiver Architecture 43
3.4.3 Smart Transmitter Multi-Channel Front-End Electronics 44
3.4.4 7-Channel Transmitter Architecture 45
3.5 Conclusion 49

Chapter 4 Modeling and Simulation of Smart Transmitters and Receivers . . **50**

4.1 Lens-photodiode Array Modeling . . . 50
4.1.1 Modeling and Simulation Setup . . . 50
4.1.2 Modeling and Simulation Results . . . 55

Chapter 5 Experiments and Applications of Smart Transmitters and Receivers 67
5.1 Characterization of the Lens-photodiode Array . . . 68
5.1.1 Experiment Description . . . 68
5.1.2 Pan and Rotate System . . . 69
5.1.3 Experimental Setup . . . 70
5.1.4 Experimental Results . . . 73
5.1.5 Characterization Analysis . . . 85
5.2 Angle of Arrival Estimation . . . 86
5.2.1 Experiment Description . . . 86
5.2.2 Experimental Results . . . 92
5.3 Backscatter Estimation . . . 93
5.3.1 Experimental Setup . . . 93
5.3.2 Experimental Results . . . 99
5.4 Diversity Combining . . . 100
5.4.1 Experimental Setup . . . 100
5.4.2 Processing . . . 100
5.4.3 Experimental Results . . . 109
5.5 Multiuser: CDMA and SDMA . . . 110
5.5.1 Experimental Setup . . . 110
5.6 Discussion . . . 112
5.7 Adaptive Coordination . . . 113

Chapter 6 Conclusion . . . 115
6.1 Review of Goals . . . 115
6.2 Major Contributions . . . 116
6.3 Prototype Specifications . . . 117
6.4 Future Work . . . 118
6.5 Conclusion . . . 119

References . . . 121

Appendix . . . 127
Appendix A Embedded Real-Time Underwater Free-Space Optical Communication System with Error Correction Coding . . . 128

LIST OF TABLES

Table 2.1 Table of optical constituent contributions (to light in visible wavelengths). 22

Table 4.1 2-D angles for all ϕ 57
Table 4.2 2-D angles for fixed ϕ 57

Table 5.1 Mapping between pan and rotate ranges and characterization geometry ranges. 69
Table 5.2 List of characterization experiments. 73

Table A.1 Summary of parameters for the embedded $\mathcal{C}_{RS}(255, 223)$ RS 134

LIST OF FIGURES

Figure 1.1 Scenario showing swarms of underwater vehicles and sensor nodes. 2
Figure 1.2 Multi-user reception system scenario with three nodes. A & C are transmitting. B is receiving. Note: Only three field of views (channels) per user are shown, for clarity. 4
Figure 1.3 Optical backscatter estimation. The receiver on B is observing backscatter when its co-located transmitter is active. This local water quality measurement complements SNR measurements obtained from data link. . 5
Figure 1.4 Electronic switched pointing & tracking. B can sense the direction of C and beam steer its transmitter towards C. The identity of transmitters can be determined from coding of the data. 6

Figure 2.1 Summary of optical properties of water. 14
Figure 2.2 Example volume scattering functions. 17
Figure 2.3 Example phase functions. 17
Figure 2.4 Range of size for various optically significant ocean water constituents. . . 21
Figure 2.5 Particle size distribution for typical ocean constituents. 22
Figure 2.6 n and k for a range of wavelengths in pure water. 24
Figure 2.7 Absorption from pure water. 25
Figure 2.8 Absorption from phytoplankton. 25
Figure 2.9 Absorption from non-algal particles. 25
Figure 2.10 Absorption from CDOM. 25
Figure 2.11 Example absorption coefficients. 26

Figure 3.1 FOV of a bare photodiode without a lens. (Active area of photodiode used has a diameter of 2.65 mm). 33
Figure 3.2 FOV of single lens-photodiode pair with single 1 inch lens and photodiode at focus of the lens. FOV decreases from $\sim 120^\circ$ to $\sim 10^\circ$. 33
Figure 3.3 Isometric view of solid rendering of lens head. Not shown in rendering is planar photodiode array below the lenses. The truncated pyramid structure houses 7 lenses and 7 photodiodes below. 36
Figure 3.4 Top view of solid rendering of lens head. Not shown in rendering is planar photodiode array below the lenses. The truncated pyramid structure houses 7 lenses and 7 photodiodes below. 36
Figure 3.5 Sketch showing light entering through top lens and falling on multiple photodiodes. 49 such directions ("channels") exist for the prototype lens-photodiode array. 36
Figure 3.6 Sketch showing light entering through the side lens and falling on multiple photodiodes. 49 such directions ("channels") exist for the prototype lens-photodiode array. 36
Figure 3.7 Image of (a) isometric view and (b) top view of the prototype lens array built. 37

Figure 3.8 Picture of lens-photodiode array with light incident normal to the middle lens. Photodiodes array on the PCB can also be seen where focus lies above the middle photodiode. 38
Figure 3.9 Image of (a) isometric view and (b) top view of the prototype LED array built. 40
Figure 3.10 Simulation correlator outputs for the data sequence 111001010 spread using a 32 chip prime code sequence of P = 5 with 7 padding zeros. . . . 41
Figure 3.11 7-Channel receiver PCB. 43
Figure 3.12 7-Channel transmitter PCB. 45
Figure 3.13 Schematic of one of the channels of the 7-Channel transmitter using the DAC-based bias tee LED driver. 47
Figure 3.14 Output (a) voltage and (b) current performance of DAC-based bias tee LED driver. 48
Figure 3.15 7-Channel receiver (left) and 7-Channel transmitter (right) placed side-by-side. 49

Figure 4.1 Geometry used for describing system. 51
Figure 4.2 Origin transformation for each lens. Global co-ordinates are at the center of the middle (top) lens. 52
Figure 4.3 Naming convention for lenses and photodiodes. 52
Figure 4.4 Position and naming convention for photodiode array. 53
Figure 4.5 Angles each lens is sensitive to in three-dimensional space. 58
Figure 4.6 Top view of angles each lens is sensitive to in three-dimensional space. . . 59
Figure 4.7 Visualizing focal points and their corresponding intensities for each lens. . 60
Figure 4.8 Top-view of visualizing focal points and their corresponding intensities. . 61
Figure 4.9 Top-view of visualizing summation of focal points and intensities. 62
Figure 4.10 Top-view of spherical projection of each lens-photodiode pair field of view. 63
Figure 4.11 Field of view plots for all 7 lenses and 7 photodiodes. 64
Figure 4.12 One-axis field of view plots for all 7 lenses and 7 photodiodes. 65
Figure 4.13 One-axis field of view photodiode outputs. 66

Figure 5.1 Geometry used for characterization. 69
Figure 5.2 Perspective side view image of pan and rotate system with 7-channel receiver and lens-photodiode array mounted. Overlay shows axes of rotation. 71
Figure 5.3 Front view of pan and rotate system with 7-channel receiver and lens-photodiode array mounted. Separation between lens-array and photodiode-array is at its maximum experimented position of 70 mm. 72
Figure 5.4 NI USB-6009 digitizer. 73
Figure 5.5 Image of exp_A1 spot size. Note that the spot size is chosen to be slightly less than the active area of each photodiode. 74
Figure 5.6 Image of exp_A2 spot size. Note that the spot size is chosen to be slightly more than the active area of each photodiode. 74
Figure 5.7 Image of exp_A3 spot size. Note that the spot size is chosen to be approximately the inside-to-inside gap of the photodiodes such that the spot enters the next photodiode as it leaves one. 74

Figure 5.8 Image of exp_A4 spot size. Note that the spot size is chosen to be approximately the outside-to-outside gap of the photodiodes such that the spot always includes at least one photodiode. 74
Figure 5.9 Two-dimensional single-axis FOV for Exp_A0: No lens array. 75
Figure 5.10 Two-dimensional single-axis FOV for Exp_A1: Lens-photodiode separation = 40 mm. 76
Figure 5.11 Two-dimensional single-axis FOV for Exp_A2: Lens-photodiode separation = 50 mm. 77
Figure 5.12 Two-dimensional single-axis FOV for Exp_A3: Lens-photodiode separation = 60 mm. 78
Figure 5.13 Two-dimensional single-axis FOV for Exp_A4: Lens-photodiode separation = 70 mm. 79
Figure 5.14 Top-view of three-dimensional FOV in spherical co-ordinates for Exp_A0: No lens array. $\theta = 0^\circ$ lies at the center and increases outwardly till $\theta = 90^\circ$ at the edge of the hemisphere. $\phi = 0^\circ$ points south and increases clockwise. $\phi = 180^\circ$ points north. 80
Figure 5.15 Top-view of three-dimensional FOV in spherical co-ordinates for Exp_A1: Lens-photodiode separation = 40 mm. $\theta = 0^\circ$ lies at the center and increases outwardly till $\theta = 90^\circ$ at the edge of the hemisphere. $\phi = 0^\circ$ points south and increases clockwise. $\phi = 180^\circ$ points north. 81
Figure 5.16 Top-view of three-dimensional FOV in spherical co-ordinates for Exp_A2: Lens-photodiode separation = 50 mm. $\theta = 0^\circ$ lies at the center and increases outwardly till $\theta = 90^\circ$ at the edge of the hemisphere. $\phi = 0^\circ$ points south and increases clockwise. $\phi = 180^\circ$ points north. 82
Figure 5.17 Top-view of three-dimensional FOV in spherical co-ordinates for Exp_A3: Lens-photodiode separation = 60 mm. $\theta = 0^\circ$ lies at the center and increases outwardly till $\theta = 90^\circ$ at the edge of the hemisphere. $\phi = 0^\circ$ points south and increases clockwise. $\phi = 180^\circ$ points north. 83
Figure 5.18 Top-view of three-dimensional FOV in spherical co-ordinates for Exp_A3: Lens-photodiode separation = 60 mm. $\theta = 0^\circ$ lies at the center and increases outwardly till $\theta = 90^\circ$ at the edge of the hemisphere. $\phi = 0^\circ$ points south and increases clockwise. $\phi = 180^\circ$ points north. 84
Figure 5.19 Estimates (y-axis) vs. actual (x-axis) angle of arrival for Exp_A1: Lens-photodiode separation = 40 mm using look-up table (LUT) algorithm. See plot below for error metrics. 88
Figure 5.20 Absolute estimate error (top plot) and number of options in LUT, both as a function of actual angle of arrival for Exp_A1: Lens-photodiode separation = 40 mm. 88
Figure 5.21 Estimates (y-axis) vs. actual (x-axis) angle of arrival for Exp_A2: Lens-photodiode separation = 50 mm using look-up table (LUT) algorithm. See plot below for error metrics. 89
Figure 5.22 Absolute estimate error (top plot) and number of options in LUT, both as a function of actual angle of arrival for Exp_A2: Lens-photodiode separation = 50 mm. 89

Figure 5.23 Estimates (y-axis) vs. actual (x-axis) angle of arrival for Exp_A3: Lens-photodiode separation = 60 mm using look-up table (LUT) algorithm. See plot below for error metrics. 90
Figure 5.24 Absolute estimate error (top plot) and number of options in LUT, both as a function of actual angle of arrival for Exp_A3: Lens-photodiode separation = 60 mm. 90
Figure 5.25 Estimates (y-axis) vs. actual (x-axis) angle of arrival for Exp_A4: Lens-photodiode separation = 70 mm using look-up table (LUT) algorithm. See plot below for error metrics. 91
Figure 5.26 Absolute estimate error (top plot) and number of options in LUT, both as a function of actual angle of arrival for Exp_A4: Lens-photodiode separation = 70 mm. 91
Figure 5.27 Prototype system experimental setup outside water tank window for backscatter estimation. Picture taken before experiment with clear water in tank. Room lights are on for photographing setup. 94
Figure 5.28 Prototype system experimental setup outside water tank window for backscatter estimation. Picture taken before experiment with clear water in tank. Some room lights are on for photographing setup. 94
Figure 5.29 Measured attenuation coefficient using the transmissometer as Maalox was added in increments of 25 ml for Exp_B1. 95
Figure 5.30 Backscatter optical power observed by the commercial-off-the-shelf (COTS) receiver for Exp_B1 plotted as a function of attenuation length calculated from transmissometer measurements. The use of the COTS receiver allows to measure an absolute value of the return light collected. 96
Figure 5.31 Backscatter optical power observed by the commercial-off-the-shelf (COTS) receiver for Exp_B1 plotted as a function of attenuation coefficient measured from transmissometer. The use of the COTS receiver allows to measure an absolute value of the return light collected. 97
Figure 5.32 Backscatter optical power observed by the prototype 7-channel transmitter and receiver for Exp_B2 plotted as a function of attenuation coefficient measured from transmissometer. 98
Figure 5.33 Estimate (y-axis) vs. actual (x-axis) SNR plotted to show estimator performance. 102
Figure 5.34 Squared error of SNR estimator to show range of reliable estimates. . . . 102
Figure 5.35 SNR and noise floor of the power spectral density (PSD), for equal gain combining (EGC) and selection combining (SEL), as the number of channels are added incrementally. Only one receiver is pointed towards and actively receiving data from the transmitter in this experimental scenario. 103
Figure 5.36 Eye diagram of received signal in high SNR (>20 dB). The prime code used for CDMA spreading does not have any 1 to 0 or 0 to 1 transitions. . 104
Figure 5.37 Eye diagram of received signal when EGC is used and no. of channels = 1. 105
Figure 5.38 Eye diagram of received signal when EGC is used and no. of channels = 2. 106
Figure 5.39 Eye diagram of received signal when EGC is used and no. of channels = 3. 106
Figure 5.40 Eye diagram of received signal when EGC is used and no. of channels = 4. 107

Figure 5.41 Eye diagram of received signal when EGC is used and no. of channels = 5. 107
Figure 5.42 Eye diagram of received signal when EGC is used and no. of channels = 6. 108
Figure 5.43 Eye diagram of received signal when EGC is used and no. of channels = 7. 108
Figure 5.44 Correlation of the received signal at User B from two different transmitters, User A and User C, with their outputs spread using the respective CDMA codes 1 and 3. Only User A is transmitting in (a), only User C is transmitting in (b), and both Users A and C are transmitting in (c). Graph shown is for a bit "1" spread using two different 32-chip prime codes. The bits are intentionally synchronized between the two transmitters for the sake of comparison, although synchronization between the transmitters is not required. 111
Figure 5.45 Closed-loop system architecture of smart-transceiver. The transmitter is capable of direction, output power, and rate control, based on feedback from backscatter and angle of arrival estimator at the receiver. 113

Figure A.1 1000 gallon water tank built and used for underwater free-space optical communication experiments done at NCSU. 130
Figure A.2 Relationship between attenuation coefficient and SNR for experiments in laboratory test tank. Attenuation and albedo are controlled by introducing measured amounts of scattering particles such as liquid Maalox and Nigrosin dye to mimic ocean water. 131
Figure A.3 Experimental performance of various error correction codes implemented for underwater free-space optical communication at NCSU as a function of code rate vs. performance in E_b/N_0 at a BER of 10^{-4}. 131
Figure A.4 Block Diagram of Transmitter. 132
Figure A.5 Block Diagram of Receiver. 133
Figure A.6 The expected BER improvements for two Reed-Solomon codes are compared. 134
Figure A.7 First 4 bytes of NRZ header. 135
Figure A.8 Signal acquisition and clock and byte recovery. 136
Figure A.9 Packaged transmitter. 137
Figure A.10 Inside view of the packaged transmitter. 137
Figure A.11 Front view of the packaged receiver. 137
Figure A.12 Back view of the packaged receiver. 137
Figure A.13 Transmitter on the unmanned underwater vehicle (UUV) Seawolf III. . . 139
Figure A.14 Receiver mounted at pool side during pool test. 139

Chapter 1

Introduction

Underwater communication is of great interest to military, industry, and scientific communities. Underwater vehicles, sensors, and observatories require a communications interface with data rates in the few to tens of Mbps. While fiber optic or copper cabling can be used for sufficiently large or stationary devices, a wireless link is desirable in many situations. Radio frequencies are heavily attenuated in seawater. Acoustic communication is the existing prevalent method but suffers from low data rates, high latencies, and multipath issues. For short-range links, free-space optical communications is a promising alternative.

Recently, underwater free-space optical communication has witnessed a surge in interest from developments in blue-green sources and detectors [1],[2],[3],[4]. These take advantage of the "blue-green optical window" of relatively low attenuation of blue-green wavelengths of the electromagnetic spectrum underwater. Laser-based systems have been demonstrated for extended ranges, high data rates and low latencies [5]. LED-based systems have been demonstrated for low-cost, low-power, and compact systems [6].

Underwater free-space optical communication is typically considered point-to-point and, thus far, most researchers have treated it as such. Point-to-point links require strict pointing and tracking, especially on mobile platforms. This is reasonable in systems that use collimated laser links and are typically large enough to afford dedicated gimbal systems. Some systems also use very large aperture ($\sim$20 inch) photomultiplier tubes (PMTs) that increase the receiver field of view (FOV)[1].

In some situations, however, compact systems are desired. Smaller platforms with compact systems do not have the volume or energy budget for sophisticated pointing and tracking. Large-area PMTs can be expensive and bulky. In the presence of multiple users or strong background ambient light, a single-output wide FOV could also be a disadvantage.

For such situations, it is useful to develop low-cost, compact solutions to these problems. In traditional RF wireless, smart antennas are an integral part of most mobile communications

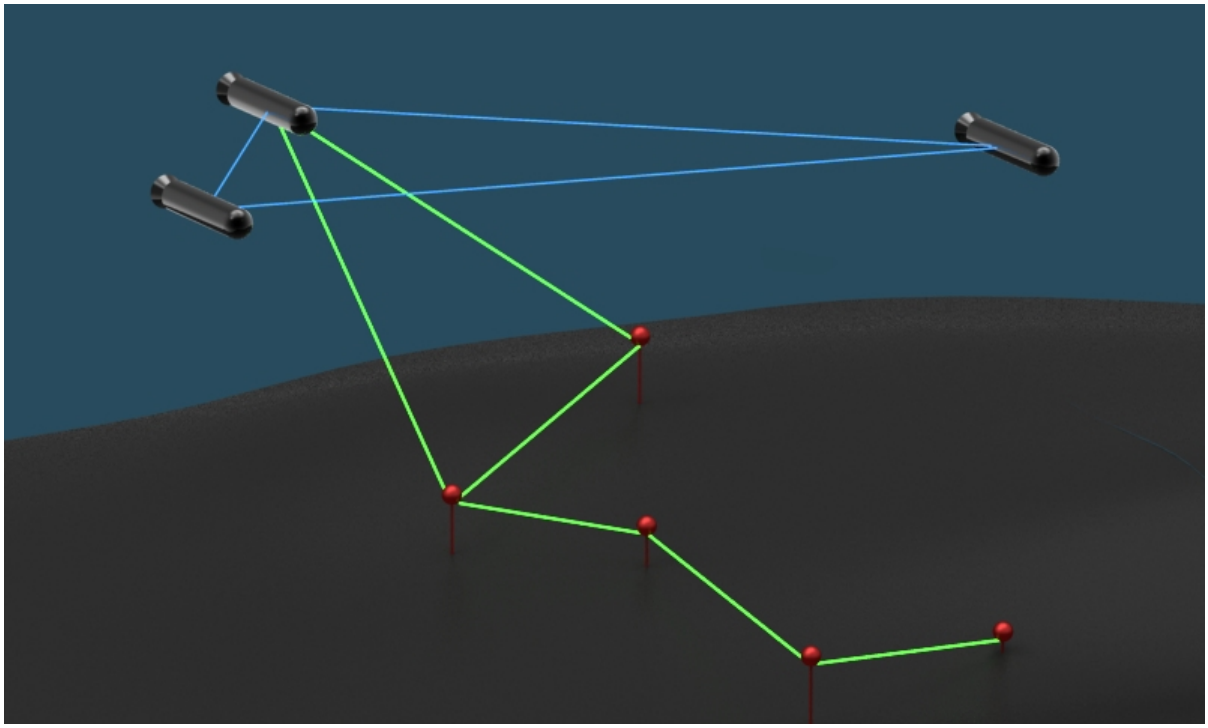

Figure 1.1: Scenario showing swarms of underwater vehicles in formation and sensor nodes using wide field-of-view smart transmitters and receivers to form free-space optical communication networks underwater.

standards, such as 4G LTE Advanced. Smart antennas are capable of signal processing to provide angle of arrival information and transmit beamforming. In indoor optical wireless, multiple antennas with spatial and angular diversity are used for non-line-of-sight communications, ambient light rejection, electronic pointing and tracking, relative localization, and multi-hop networking. It is natural to consider the benefits of such techniques extended to the underwater environment.

In this dissertation, we propose a new optical front-end for underwater free-space optical communication. The new front-end introduces the concept of smart receivers and transmitters. The smart receivers have segmented wide FOV and are capable of detecting angle of arrival of signals in order to adjust and orient FOV towards the desired signal. The smart transmitters are capable of using this information to electronically steer its output beam towards a particular direction. The smart transmitters are also capable of estimating water quality from its backscattered light collected by its co-located receiver, which is used to adapt to changing water conditions. The transmitter outputs are also code division multiple access (CDMA) coded for operation in a multi-user environment.

The overarching goal of this research is to design and prototype smart receivers and transmitters capable of coordinated sensing and communicating.

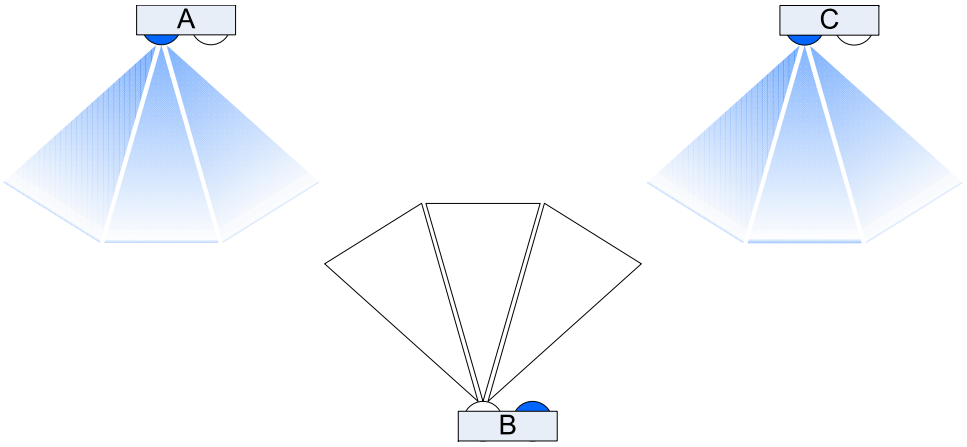

Figure 1.2: Multi-user reception system scenario with three nodes. A & C are transmitting. B is receiving. Note: Only three field of views (channels) per user are shown, for clarity.

1.1 Benefits of Smart Optical Systems

Smart receivers and transmitters are the physical layer enabling technology for coordinated sensing and communicating, and the focus of this research. As an example, consider smart optical transmitters and receivers that can estimate the apparent optical properties of water, send a beam of light in a desired direction, and determine the direction and identity of light that is being received.

This information can then be used in many different phases of an underwater vehicle's operation. Determining the water quality can be used to adaptively change the power of transmission or gain of the receiver during detection and acquisition of another platform. Knowledge of vehicle orientation, identity, and relative angle can be used to localize and determine the relative positions of vehicles. Following are brief descriptions of potential benefits.

1.1.1 Non-mechanical pointing and tracking on a moving underwater vehicle

Depending on the sea state and the controls of an underwater vehicle, an optical transmitter or receiver mounted on it can go in and out of alignment with another stationary or mobile platform as the vehicle moves. An optical front-end capable of changing its effective FOV, detecting angle of arrival at its receiver, as well as electronically steer its output beam, can potentially maintain a communications link in such an environment. Furthermore, one can utilize signal diversity techniques to improve signal reliability.

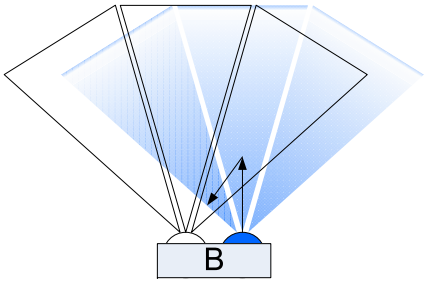

Figure 1.3: Optical backscatter estimation. The receiver on B is observing backscatter when its co-located transmitter is active. This local water quality measurement complements SNR measurements obtained from data link.

1.1.2 Maintaining link with a stationary node as an underwater vehicle does a drive-by

Station keeping and maintaining a precise relative position can be energy intensive and difficult for underwater vehicles. The ability to interrogate and collect data from a stationary sensor node as a vehicle drives by can add significant operational capability. Thus, a quasi-omnidirectional receiver capable of continually adapting its FOV and optical power is of value.

1.1.3 Providing sensory information to underwater vehicles

In a swarm environment, localization information can be gathered from angle of arrival information as various nodes talk to each other. This information can be passed to the vehicle to augment its other sensory information for navigation and collision avoidance purposes. A smart optical front-end can also provide other sensory information such as water quality measurements obtained from the communications link.

1.1.4 Duplex multi-user system

Each transceiver consists of a smart receiver and a smart transmitter. Spatial diversity allows for simultaneous reception from two non-co-located transmitters. Since each transmitter is CDMA coded, the smart receiver at B is also capable of associating A and C data streams with their corresponding directions. In the event that A and C are co-linear, the CDMA code still allows for separating the two transmit streams at the receiver on B.

In a mesh network scenario, as illustrated in Fig. 1.2, users A and C are not within range of each other. Assuming localization information from angle of arrival is kept at each node, B can relay messages between A and C through a hop network. If B is a mobile node, it can be positioned to effectively extend the optical communication range between A and C when needed.

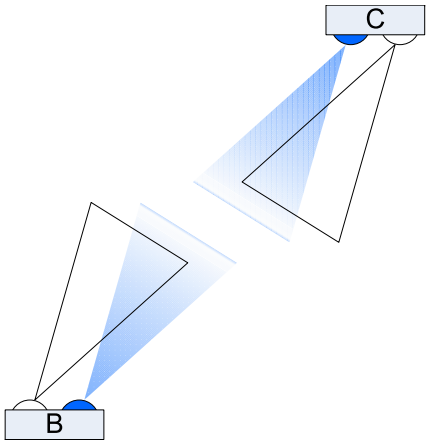

Figure 1.4: Electronic switched pointing & tracking. B can sense the direction of C and beam steer its transmitter towards C. The identity of transmitters can be determined from coding of the data.

1.1.5 Optical backscatter estimation to assess water quality

The duplex system provides a way for a receiver to monitor optical backscattering while its co-located transmitter is active, as illustrated in Fig. 1.3. Based on the modulation scheme used, steps would need to be taken to isolate background, interference, and unmodulated light. Using volume scattering information, an estimate of the attenuation coefficient can be made based on the measured amount of backscatter. This complements SNR measurements that can be obtained from the tx/rx signals.

1.1.6 Electronic Switched Pointing & Tracking

Angle of arrival information at a receiver is passed along to its co-located transmitter. The transmitter can then switch to a beam that points its output in the direction of the incoming beam to optimize the link, as illustrated in Fig. 1.4.

1.1.7 Segmented wide field of view for ambient light rejection

A segmented wide field of view with multiple outputs, as compared to a single-output detector with the same combined field of view, can tolerate background light while continuing to receive signals from a transmitter that is not co-located with the background source.

1.2 Major Contributions

The four major contributions of this research are:

1. **Smart receiver**: The receiver has a segmented wide field of view for efficiently receiving from multiple directions and multiple users.

2. **Smart transmitter**: The transmitters are highly directional with individually addressable LEDs for electronic switched beam steering.

3. **Sensing through angle of arrival estimation**: The smart receivers are capable of estimating angle of arrival of incident light from the transmitters for localization in swarms.

4. **Sensing through backscatter estimation**: The smart transmitters are capable of estimating water quality from its backscattered light collected by its co-located receiver.

1.3 Overview of Dissertation

We begin, in **Chapter 2**, by first providing an overview of underwater free-space optical communication. This includes a literature survey of some of the active areas of research relevant to this thesis. This is followed by a paraphrased summary to serve as an introduction to the physics of light underwater for the new researcher. Finally, a link budget is provided to the practicing engineer to aid in designing an underwater communications link.

In **Chapter 3** we propose a design and describe a prototype smart transmitter and receiver system. However, a discussion of some of the challenges of such a design with the design goals in perspective is first discussed. This is followed by a description of the design and the considerations involved. Finally, the new electronics front-end that helps leverage the capabilities of the optical front-end is presented.

Chapter 4 describes a model of the receiver front-end built in MATLAB and used to simulate the behavior of the smart receiver as light is incident on it. The model is useful for understanding and visualizing the responsivity of the smart receiver, that is not possible from experimental data alone. The model also helps select design parameters and their effects as they are changed.

Chapter 5 details all of the experiments conducted with the prototype smart transmitter and receiver. This includes a thorough characterization of the devices, followed by proof-of-concept experiments of the angle of arrival and water quality through backscatter estimation experiments.

Finally, **Chapter 6** summarizes the major findings and concludes the dissertation. A list of suggestions for future work are also provided to outline some of the extensions of this dissertation.

Appendix A reviews some of the prior work directly related to this dissertation. Prior work involves implementation of a free-space optical communications link on an underwater vehicle and its limitations in effectively pointing and tracking, alleviating which, has been the primary motivation of this research.

Chapter 2

Background

The goal of the background section is to provide an overview of some of the active areas of research relevant to this thesis. This background chapter is organized as follows:

- Related Research
  - In Underwater Free-Space Optical Communication
  - In Indoor Optical Wireless Communication
- Underwater Optical Channel
  - Optical Properties of Water
  - Optically Significant Constituents of Water
  - Electromagnetic Properties of Water
- Link Budget
  - Signal-to-Noise Ratio
  - System Tradeoffs

The related research section outlines some of the literature published in this research area. The underwater optical channel section provides a paraphrased summary to serve as an introduction to the physics of light underwater for the new researcher. Finally, a link budget is provided to the practicing engineer to aid in designing an underwater communications link.

2.1 Related Research in Underwater Free-Space Optical Communication

Historically, interest in free-space underwater optical communication has been in submarine to satellite laser communications [7]. Some of the first attempts at characterizing the channel for this purpose was published by Karp in 1976 [8]. The first system architecture to use blue/green laser sources from a satellite to submarine is discussed by Wiener and Karp [9]. The first duplex laser communication between a submerged submarine and and aircraft was conducted in 1991 by Stotts et al. [10]. Snow et al. conducted some of the first studies on spatial and temporal spreading of modulated optical pulses at rates as high as 100 MHz [11].

Underwater applications for free-space optical communication have grown more popular in recent years with the creation of reliable, low-cost light sources, like LEDs [6] and diode lasers [5], that take advantage of the comparatively low attenuation of light in the 400 nm – 550 nm range in seawater [12].

At NCSU, research has also focused on implementing Forward-error-correction (FEC) for such links. FEC is a well known technique commonly used in communications to detect and correct errors. In principle, FEC allows the system to operate at a lower SNR for a given BER. The use of FEC has also been examined in acoustic underwater systems [13, 14] as well as in atmospheric optical communication systems [15, 16]. Underwater optical systems can benefit from FEC in a variety of ways. FEC can reduce power requirements at the transmitter, extend the range of feasible communication for a given water condition, and/or increase the reliability of the link over a varying degree of water and environmental conditions. An underwater optical communication system using FEC based on a Reed-Solomon (RS) error correcting scheme was previously investigated by the authors [17]. The encouraging results led to the investigation of the more modern, state-of-the-art Universal Mobile Telecommunications System (UMTS) and Consultative Committee for Space Data Systems (CCSDS) turbo codes as well as DVB-S2 Low-Density Parity-Check codes [18]. A real-time practical implementation of the RS code was also implemented for interfacing with an underwater vehicle at 5 Mbps [19]. Research has also been done on using polarization as a modulation scheme [20] and a MEMS retroreflecting modulator that operates in the Blue/Green spectrum [21]. A precursor to this research was also done through the investigation of spatial diversity to understand optical fading in the underwater optical channel [22].

At Woods Hole Oceanographic Institute, Farr et al., in 2005, proposed a design and tradeoffs for a directional and omni-directional underwater optical communication to use diode lasers or arrayed LEDs [23]. A 17-inch diameter aperture omni-directional receiver and arrayed LED-based transmitter link was developed with experiments conducted in Bermuda where data rates as high as 5 Mbps was achieved in ranges as long as 200 m in very clear water and at 2.5 Mbps at

a range of 40 m in 0.67 m^{-1} water [1]. A full-duplex 10 Mbps system was also constructed by the authors and demonstrated real time video transfer in dock tests [24]. Recently the authors also deployed a system as a data-mule application for collecting seismic data from a seafloor borehole at a range of 100 m at up to 10 Mbps [25].

At MIT's Computer Science and Artificial Intelligence Lab, Rus et al. has been working on optical communication in integration with Autonomous Underwater Vehicles (AUVs). Their first prototype has a range of 2.2 m in clear water to 1.2 m in turbid waters with a data rate of 320 kbps [26] and was demonstrated as a sensor-robot interaction platform. The sensor nodes were deployed for creek monitoring collecting pressure and temperature data. The system is expanded to work for a swarm of vehicles in a coordinated data muling application where optical communications is used to augment acoustics communications for high data rate communication between the vehicles [27]. The authors also describe the longer range (up to 400 m in clear ocean) system operating at the same data rate and using TDMA for multiple access [28]. Two newer versions of the system were then developed. A short-range system uses a Si photodiode at the receiver and a longer range system uses an avalanche photodiode at the receiver. Both systems use an array of six 5 W LEDs at the transmitter and has a data rate of up to 1.2 Mbit/s [3]. The new system is used in a command and control application to control an AUV the receiver is mounted on [29]. A second, and latest, generation of their system is bi-directional, uses software defined radio principles and has a data rate of up to 2.28 Mbps [30].

At Patuxent River Naval Air Systems Command, Mullen et al., in 2002, experimentally validated volume scattering function measurements for the phase function of Maalox against mie scattering theory on polystyrene microsphere measurements and a Monte Carlo simulation. The authors also validated the use of Maalox as a scattering agent by comparing its measured phase function against two different in situ measurements in the ocean [31]. Cochenour et al. conducted some initial studies on the effects on multiple scattering on subcarrier intensity modulated BPSK communications link (on modulation depths) and found the effects to be not detrimental to the link, at least in short ranges (3.3 m) for small pointing inaccuracies ($< 5°$) [32]. Further experiments were also conducted for higher order modulation schemes (up to 32-QAM at 5 Mbps) with similar results, although pointing inaccuracies were not considered in this experiment [2]. A more thorough look at this spatial spreading of the optical beam was conducted by the authors and compared with a small angle approximation theoretical model for validating and to extrapolate received optical powers for a range of up to 100 m. Results show deviation from Beer's law in expected receiver power at higher attenuation lengths increased by the presence of multiply scattered photons captured at the receiver that are not accounted for by Beer's law, but aide the overall non-temporal performance of the system [33]. The effect of scattering on the degree of depolarization an well as its variability on the scattering albedo is also studied. As the addition of Maalox does not change the absorption, the scattering albedo is changed by

the addition of Nigrocin as an absorbing agent [34]. These results were also studied for, and used to polarize the return beam from a retroreflector that uses polarization discrimination in order to increase the contrast of the return beam [35]. Recently, the authors have studied the propagation of 1 GHz intensity modulated optical signals to observe the effect of scattering on the frequency response of the modulation depth as well as the degree of polarization [36]. The results were also extended to variability due to different scattering albedo from the addition of different scattering and absorbing agents [37].

Hanson and Radic did the first measurements on optical communication at a data rate of 1 Gbits/s and observed temporal spreading of the pulses experimentally and at a higher resolution and range using Monte Carlo methods [4]. Hanson and Lasher also studied the coupling efficiency of a focused beam in to a single-mode fiber and its dependance on turbulence as well as its mitigation using a tip-tilt control system [38]. Arnon et al. has looked at non-line-of-sight links for underwater free-space optical communications as well [39] and [40].

2.2 Related Research in Indoor Optical Wireless Communication

This section describes some of the active areas of research from indoor optical wireless (IOW) pertinent to this dissertation. Although the underwater channel is different from the indoor through-air channel, the sources and detectors are similar between the two areas. Notably, Minh et al. has used pre [41] and post [42] equalization techniques to achieve up to 100 Mbps using LEDs as light sources. The use of white LEDs has been further studied for IOW by Cui et al. [43].

Although optics has been leveraged as the phase-controller in X band beamforming phase arrays [44], coherent optical beamforming itself is hard to achieve. Advances have been made in a variety of techniques for non-mechanical beam steering [45] including using polarization gratings [46].

In IOW, in addition to the normal pointing and tracking requirements of free-space optical communications, it is also important to avoid strong background interference from other light sources. Wang et al. has studied the effect of this strong background light [47] and proposed a mechanical steering solution at the receiver [48].

Kahn et al. at UC Berkeley did some of the first work on using multi-beam transmitters and imaging receivers [49]. Their focus has been on replacing diffuse transmitters with multiple narrow beam transmitters to reduce path loss, and on replacing non-imaging receivers with imaging light concentrators with segmented photodetectors to reduce ambient light noise and multipath distortion. They also demonstrate angle diversity reception and spatial multiplexing

using the new scheme [50]. A thorough characterization of such methods are also described by the authors [51]. A prototype using angle diversity and operating in the IR with a data rate of 70 Mbps and achieving near optical performance using maximum ratio combining is also given [52].

Yuksel et al. proposed using a spherical array of LEDs and photodetectors to solve alignment issues in IOW [53]. They also proposed using similar structures and their performance in multi-hop networking [54]. A prototype array is constructed and described [55]. A GPS-assisted 3D localization scheme is also developed [56] and coverage and other performance metrics of their system described [57]. The system does not employ the use of lenses at the transmitter or the receiver for light focusing or collecting. While this reduces complexity, imaging diversity gains are traded for angle diversity. Also, the use of lenses is strictly not required in indoor environments where the channel attenuation is much lower than atmospheric and underwater free-space optical communication.

2.3 The Underwater Optical Channel: Optical Properties of Water

The underwater free-space optical channel is vastly different from the atmospheric channel. There has been a significant amount of studies on the optical properties of water. However, the focus of most of these studies has been for the geo-physical, bio-optical and remote sensing applications. Thus the underwater channel from an optical communication perspective is still very much unknown. Nonetheless, a brief overview of the literature on optical properties of the ocean is beneficial. [58, 59, 60, 61, 62, 63, 64, 65, 66] are all excellent references on this topic and are extensively used throughout the writing of this chapter.

All of the optical properties of water can be divided into two groups called inherent and apparent.

- Inherent optical properties (IOPs) of water are the optical properties that only depend on the medium and not on external light on the medium.
- Apparent optical properties (AOPs) of water are the optical properties that depend on both the medium and the external light on the medium.

A summary of optical properties and their connections are illustrated in Figure 2.1. The radiative transfer theory, including the radiance transfer equation and radiometric quantities, connect the IOPs and the AOPs. Environmental conditions such as the incident radiance, sea state, and bottom conditions provide the boundary conditions for radiative transfer theory.

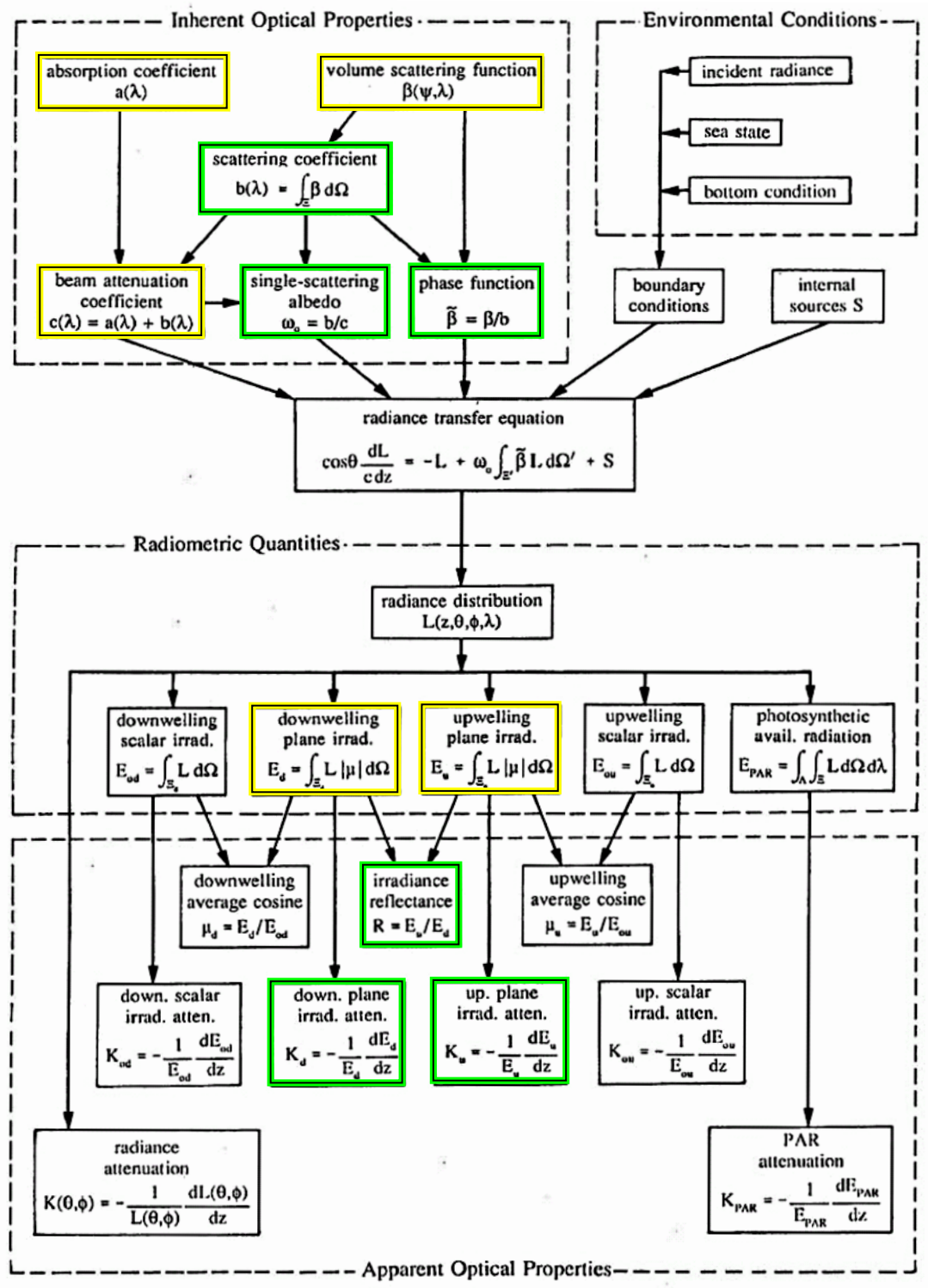

Figure 2.1: Summary of optical properties of water. Yellow highlighting shows properties typically measured. Green highlighting shows quantities typically calculated [67].

2.3.1 Inherent Optical Properties

Electromagnetic radiation such as light interacts with water and the materials dissolved and suspended in it in two different ways: absorption and scattering. Absorption is the change of electromagnetic radiation into other forms of energy. Photons essentially disappear and are converted into other forms of energy such as heat or chemical bonds. Scattering is the redirection of electromagnetic radiation. Photons essentially change its direction by means of reflection, refraction and diffraction. Absorption and scattering do not depend on external lighting conditions and thus, as previously defined, are described by IOPs. Each of these are described below.

Absorption Coefficient

Absorption coefficient is the ratio of energy absorbed from an incident power per unit distance. It has units of m^{-1} and is denoted by $a(\lambda)$.

$$a(\lambda) \equiv \frac{\mathrm{d}(\frac{\Phi_a(\lambda)}{\Phi_i(\lambda)})}{\mathrm{d}r} \tag{2.1}$$

Scattering Coefficient

Scattering coefficient is the ratio of energy scattered from an incident power per unit distance. It has units of m^{-1} and is denoted by $b(\lambda)$.

$$b(\lambda) \equiv \frac{\mathrm{d}(\frac{\Phi_s(\lambda)}{\Phi_i(\lambda)})}{\mathrm{d}r} \tag{2.2}$$

$b(\lambda)$ is also referred to as total scattering coefficient and is the sum of backward scattering coefficient ($b_b(\lambda)$) and forward scattering coefficient ($b_f(\lambda)$).

Beam attenuation coefficient

The ratio of energy absorbed or scattered from an incident power per unit distance is defined as beam attenuation coefficient. It denotes the total energy lost and can be shown to be the sum of the absorption and scattering coefficients. It has units of m^{-1} and is denoted by $c(\lambda)$.

$$c(\lambda) = a(\lambda) + b(\lambda) \tag{2.3}$$

Single-scattering albedo

Single-scattering albedo is defined as the ratio of scattering coefficient to beam attenuation coefficient and denotes the probability that a photon will be scattered, rather than absorbed. It

is a unitless term and is denoted by ω_o. It is defined as

$$\omega_o \equiv \frac{b(\lambda)}{c(\lambda)} \tag{2.4}$$

As expected, highly (primarily) scattering environments results in an albedo close to 1 and highly absorbing (primarily) environments result in an albedo close to 0. Since scattered photons are not converted to other forms of energy, single-scattering albedo is also known as the probability of photon survival.

Volume scattering function

Volume scattering function (VSF), is defined as the fraction of incident power scattered away from the beam as a function of direction ψ into a solid angle $\Delta\Omega$. It has units of $\mathrm{m}^{-1}\mathrm{sr}^{-1}$ and is denoted by $\beta(\psi, \lambda)$.

$$\beta(\psi, \lambda) = \frac{\mathrm{d}(\frac{\Phi_s(\psi,\lambda)}{\Phi_i(\lambda)})}{\mathrm{d}r\,\mathrm{d}\Omega} \tag{2.5}$$

This definition of VSF makes two assumptions. First, it is assumed that the scattering medium is isotropic. This is a reasonable assumption for a homogeneous medium. Second, it is also assumed that the light is unpolarized. A linearly polarized beam would scatter differently in different directions relative to the angle of polarization.

As expected, VSF is related to the previously defined scattering coefficient as the integral of the VSF along all angles.

$$b(\lambda) = 2\pi \int_0^\pi \beta(\psi, \lambda) \sin\psi \; d\psi \tag{2.6}$$

Phase function

Phase function is a normalization of the VSF by the scattering coefficient to give the angular distribution of scattering. Accordingly, it has units of sr^{-1} and is denoted by $\tilde{\beta}(\psi, \lambda)$.

$$\tilde{\beta}(\psi, \lambda) \equiv \frac{\beta(\psi, \lambda)}{b(\lambda)} \tag{2.7}$$

Another parameter related to the phase function is called the asymmetry parameter. It represents the shape of the phase function by averaging the phase function over the cosine of all scattering angles. It is a unitless parameter and is represented by g. The g of typical ocean waters range from 0.8 to 0.95.

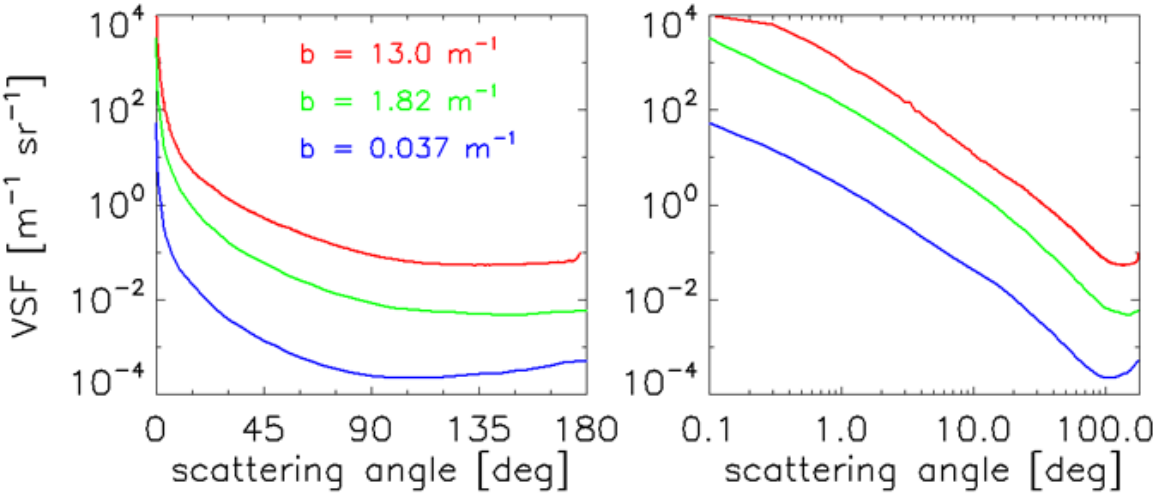

Figure 2.2: Examples of volume scattering functions on a linear (left) and log (right) axis of scattering angles: the blue curve is for clear ocean waters, green for harbor and red for coastal waters [67].

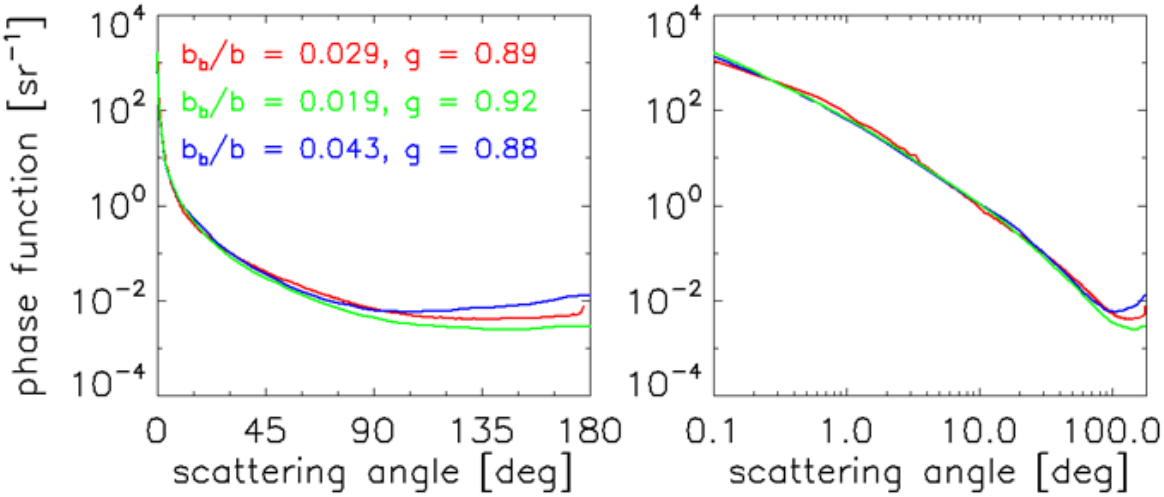

Figure 2.3: Examples of phase functions on a linear (left) and log (right) axis of scattering angles: the blue curve is for clear ocean waters, green for harbor and red for coastal waters [67].

2.3.2 Apparent Optical Properties

Apparent optical properties (AOPs) of water are those that depend on both the medium as well as the lighting that falls on the medium. However, only those properties that are stable enough to not depend on the changing environmental conditions at the time of the measurement are considered.

All of the AOPs are derived from four main radiometric quantities:

- Downwelling plane irradiance
- Downwelling scalar irradiance
- Upwelling plane irradiance
- Upwelling scalar irradiance

When radiant energy from a light source falls on a volume of water, the fundamental radiometric quantity, **radiance**, describes the power on a surface per unit area and unit sold angle. Hence radiance, denoted by L, has the units $\mathrm{Wm^{-2}sr^{-1}}$.

An instrument can be built to measure the radiant energy as it falls on a surface, in which case the radiometric quantity, **irradiance**, describes the power on a surface per unit area. Hence, irradiance, denoted by E, has the units $\mathrm{Wm^{-2}}$.

Although such an instrument, with a wide field of view, is capable of collecting light falling on it from all angles, it is not equally sensitive to light from all angles. This is because the projection of light on a collection surface of area ΔA from a large beam at an angle θ relative to the instrument axis provides an effective collection area of $\Delta A \left|\cos\theta\right|$. Thus the light collected by the instrument is proportional to the cosine of incident photon angle, and the corresponding radiometric quantity, is called **plane irradiance**.

If the instrument were to be equally sensitive to photons arriving from all angles, then the radiometric quantity measured is called **scalar irradiance**. However, such measurements are harder to make *in situ*, which is a fundamental requirement for an AOP.

In either case, the instrument can be pointed towards the surface of this water, in which case the measurement made is called **downwelling plane irradiance** or **downwelling scalar irradiance** or pointed towards the bottom, in which case, the measurement is called **upwelling plane irradiance** or **upwelling scalar irradiance**.

Diffuse attenuation coefficients

Similar to the beam attenuation coefficient previously described, sunlight penetrating the water column experiences an approximate exponential decay with depth. Boundary effects near the

surface or near the ocean floor can alter this behavior slightly, but it's mostly true when far enough from the boundaries.

This exponential relationship between the downwelling plane irradiance at two depths, $E_d(0,\lambda)$ and $E_d(z,\lambda)$, z units apart can be expressed as:

$$\frac{E_d(z,\lambda)}{E_d(0,\lambda)} \equiv \exp\left(-\int_0^z K_d(z',\lambda)dz'\right) \tag{2.8}$$

where K_d is defined as the diffuse attenuation coefficient for the downwelling plane irradiance, which can be solved as:

$$K_d = -\frac{1}{E_d}\frac{\mathrm{d}E_d}{\mathrm{d}z} \tag{2.9}$$

Similarly, other diffuse attenuation coefficients can be obtained from their corresponding irradiance measurements as shown in [67].

Since K_d is independent of absolute values of irradiance, it is mostly not influenced by the environmental conditions at the time of the experiment. However, it's accuracy can be improved by normalizing K_d to some of the environmental parameters. Gordon [68] developed such a method for a simple normalization. His method normalizes K_d values to what would be measured if the sun were at the zenith, if the sea surface were level, and if the sky were black, by dividing K_d by the parameter D_o. Hence the normalized diffuse attenuation coefficient, K_d^I is obtained as:

$$K_d^I = \frac{K_d}{D_o} \tag{2.10}$$

The normalization parameter D_o is obtained using the formula:

$$D_o = \frac{f}{\cos\Theta_{sw}} + 1.197(1-f) \tag{2.11}$$

where

$$f \approx \frac{E_d(sun)}{E_d(sun)+E_d(sky)} \tag{2.12}$$

and

$$\Theta_{sw} = \sin^{-1}\left(\frac{sin\theta_s}{1.34}\right) \tag{2.13}$$

The sun and sky irradiances can be obtained from an instrument on the deck of the ship with and without the instrument shadowed by the sun.

Reflectance

An AOP commonly used in remote sensing is reflectance. Reflectance is defined as the ratio of the upwelling to downwelling plane irradiances and is defined as:

$$R \equiv \frac{E_u}{E_d} \tag{2.14}$$

where E_u is the upwelling plane irradiance and E_d is the downwelling plane irradiance. Reflectance measurements are also typically taking just above and just below the water surface. When taken just above the water surface, it is referred to as the remote-sensing reflectance.

Average cosines

Average cosines are crude measurements of the directionality of the light field in water. It is obtained as the ratio of the plane and scalar irradiances.

The downwelling average cosine is obtained as:

$$\mu_d \equiv \frac{E_d}{E_{od}} \tag{2.15}$$

where E_d and E_{od} are the plane and scalar downwelling irradiances respectively and

$$\mu_u \equiv \frac{E_u}{E_{ou}} \tag{2.16}$$

where E_u and E_{ou} are the plane and scalar upwelling irradiances respectively.

2.4 The Underwater Optical Channel: Optically Significant Constituents of Water

Ocean waters contain a continuous spectrum of materials ranging from dissolved material with sizes below the wavelength of visible light to visible particles such a bubbles. Figure 2.4 shows a plot of range of particles and their sizes.

2.4.1 Optically Significant Constituents

The range of constituents can be broadly divided to **dissolved** and **particulate**. The exact boundary between the two is not fixed and varies based on filter pore sizes used or microscopy resolutions. Dissolved matter consists of dissolved salts and dissolved organic matter. Particulate matter can be further divided to **organic particulates** and **inorganic particulates** based on their biological or physical origin, respectively. Organic particulates consist of colloids, viruses,

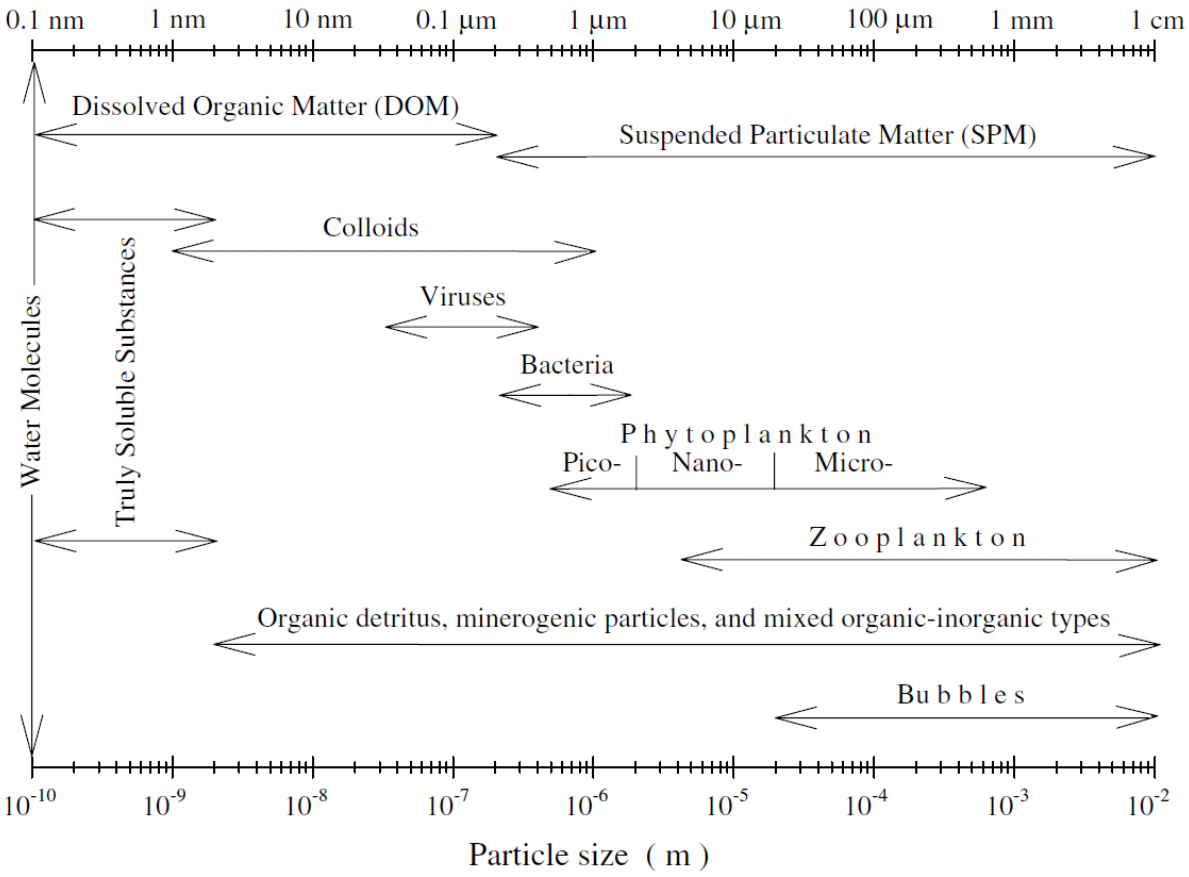

Figure 2.4: Range of size for various optically significant ocean water constituents [69].

bacteria, plankton, organic detritus, and larger organic particles. Inorganic particles consist of minerals, metal oxides, and sediment.

The contributions to optical properties due to these ocean water constituents are broadly overviewed in Table 2.1. Note that this is a broad overview and includes speculated influences since not all of these constituents have been equally studied. Nonetheless the table provides for a simple overview.

2.4.2 Particle Size Distributions

Particle size distributions provide insight on the concentration of each of the ocean water constituents described above.

Table 2.1: Table of optical constituent contributions (to light in visible wavelengths).

	Absorption	Back scattering	Forward scattering
Pure water			
Dissolved matter			
Dissolved salts	Negligible	Moderate	Moderate
Dissolved organic matter	Moderate*	Negligible	Negligible
Particulate matter			
Organic particulates			
Colloids	Negligible	Significant	Negligible
Viruses	Negligible	Significant*	Negligible
Bacteria	Moderate	Significant	Moderate
Phytoplankton	Significant	Moderate	Significant
Organic detritus	Negligible	Significant	Negligible
Larger organic particles	Negligible	Significant	Significant
Inorganic particles	Negligible	Significant	Significant

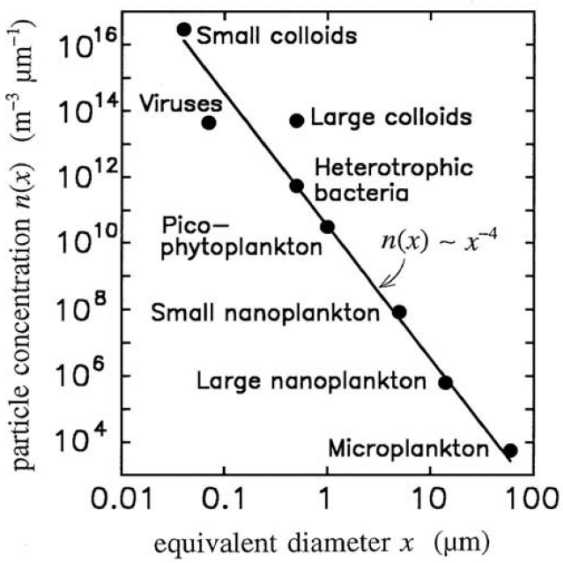

Figure 2.5: Particle size distribution for typical ocean constituents.

2.5 The Underwater Optical Channel: Electromagnetic Properties of Water

The electromagnetic properties of water can be summarized using the measurements: electrical permittivity, magnetic permeability, and electrical conductivity. Permittivity measures the resistance to an electric field formed in a dielectric medium. It is denoted by ε and has units of F/m. In vacuum, the permittivity is $\varepsilon_0 = 8.85... \times 10^{-12}$F/m. Permeability measures the degree of magnetization of a material to an applied magnetic field. It is denoted by μ and had units of H/m. In vacuum, the permeability is $\mu_0 = 4\pi \times 10^{-7}$ H/m. Conductivity is a measure of the ability of a material to conduct electric current. It is denoted by σ and has units of S/m.

Permittivity and permeability depend on the frequency, ν, of the electromagnetic wave. Additionally these parameters also depend on the condition of water, including temperature, pressure, and salinity.

The combined effects of permittivity, permeability, and conductivity are expressed through the complex index of refraction. This is represented as

$$m = n - ik, \tag{2.17}$$

where m is the complex index of refraction, n is the real part and k is the imaginary part. In the absence of an imaginary component, m and n are the same and is simply referred to as the index of refraction.

Kerker [59] provides a relationship between the complex index of refraction and the electromagnetic measurements:

$$m^2 = \mu\varepsilon c^2 - i\frac{2\pi\mu\sigma c^2}{\nu} \tag{2.18}$$

Solving for the square of the complex index of refraction, we obtain:

$$\Re\left\{m^2\right\} = n^2 - k^2 = \mu\varepsilon c^2 \tag{2.19}$$

and

$$\Im\left\{m^2\right\} = 2nk = \frac{2\pi\mu\sigma c^2}{\nu} \tag{2.20}$$

n and k are typically referred to as the optical constants and is dependent on the wavelength of light. Kerker also relates these constants to absorption and scattering.

The real index of refraction, $n(\lambda)$, is related to the scattering coefficient, $b(\lambda)$, of light in water and the imaginary index of refraction, $k(\lambda)$, is related to the absorption coefficient, $a(\lambda)$, of light in water.

The relationship for absorption is shown to be straightforward and is given by:

$$a(\lambda) = \frac{4\pi k(\lambda)}{\lambda} \tag{2.21}$$

The relationship for scattering and n depends on a variety of factors. It is shown that n changes based on the temperature, pressure, and salinity of water. However, extreme values show that this dependence varies by only $\sim 3\%$. n is influenced to a bigger extend from scattering from suspended particulate matter.

Figure 2.6 represents n and k as a function of a spectrum of wavelengths in pure water. Of interest is the window in k near the wavelengths corresponding to visible light. This results in a corresponding window in the absorption coefficient as well as shown by the previous relationship. The window can be simply explained as photons in the visible spectrum being in an energy level where they do not interact with the water molecules.

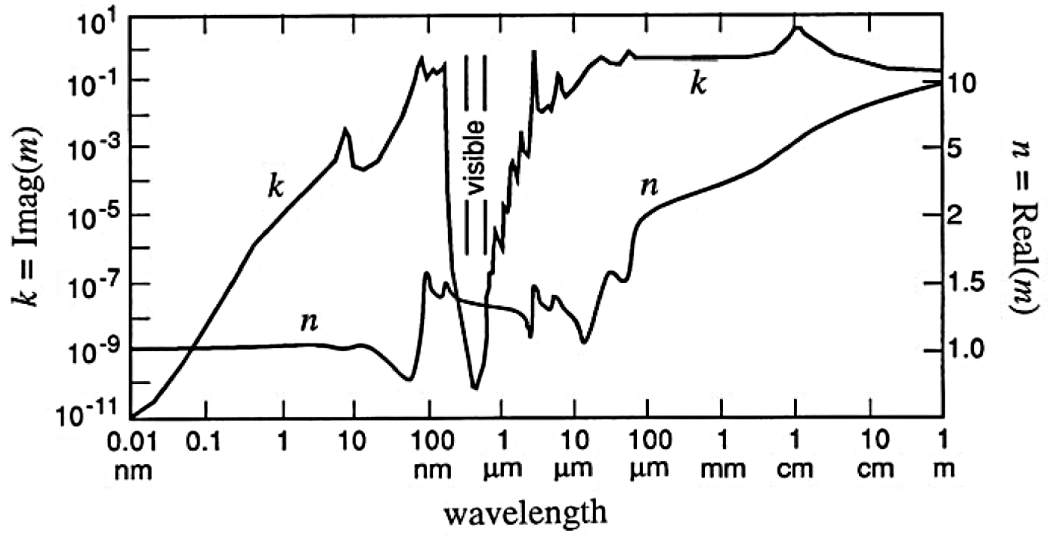

Figure 2.6: n and k for a range of wavelengths in pure water [64].

2.5.1 Absorption

Absorption is related to the imaginary index of refraction and indicates the amount of incident light lost by conversion to other forms of energy. Absorption is also tightly coupled to scattering and hence can be hard to measure. Nonetheless ranges of values of absorption for pure water and water with different classes of optically significant constituents are known. The total absorption coefficient from these different components can be written using Mobley's notations as the sum

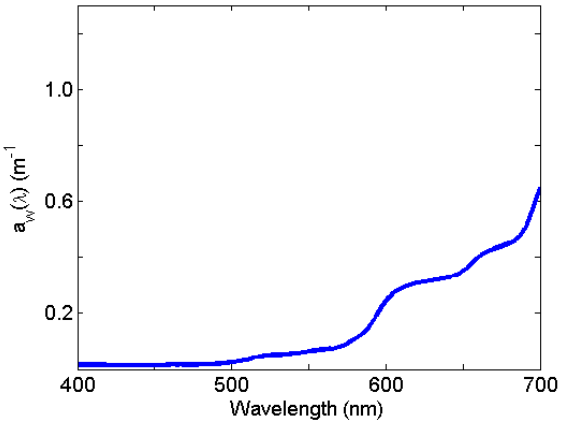

Figure 2.7: Absorption from pure water.

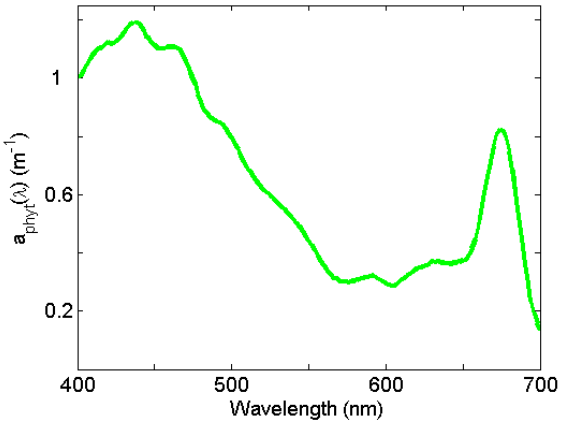

Figure 2.8: Absorption from phytoplankton.

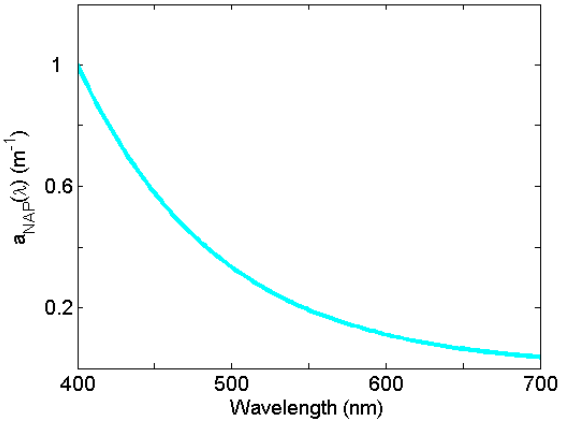

Figure 2.9: Absorption from non-algal particles.

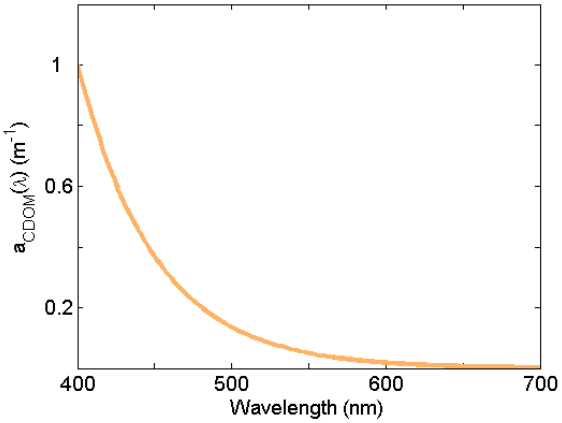

Figure 2.10: Absorption from CDOM.

of the individual absorption coefficients [67].

$$a(\lambda) = a_w(\lambda) + a_{phyt}(\lambda) + a_{NAP}(\lambda) + a_{CDOM}(\lambda) \tag{2.22}$$

where $a_w(\lambda)$ is the absorption from pure water, $a_{phyt}(\lambda)$ is the absorption from phytoplankton, $a_{NAP}(\lambda)$ is the absorption from non-algal particles, and $a_{CDOM}(\lambda)$ is the absorption from color dissolved organic matter (CDOM). Figures 2.7, 2.8, 2.9, and 2.10, show the wavelength dependence of each of these absorption coefficients, respectively.

Absorption by pure water is probably the most studied. An upper bound for absorption coefficient for pure sea water was given by Smith and Baker. The upper bound is set as the diffuse attenuation coefficient subtracted by the backscattering coefficient. The accuracy of this method can be improved by using Gordon's normalization for the diffuse attenuation coefficient.

Absorption by phytoplankton includes absorption from a variety of individual pigments, which adds to the variability of phytoplankton contributions to absorption. This source of absorption is also what leads to the most variability in the absorption between clear ocean waters and eutrophic coastal waters.

Both absorption due to non-algal particles and absorption due to color dissolved organic matter (CDOM) follow exponential curve, with strongest absorption for both in blue. Non-algal components include bacteria and zooplankton, detrital materials, and inorganic particles.

Figure 2.11 shows the combined absorption coefficient (black curve) in clear ocean waters (top plot) and coastal waters (bottom plot). The absorption coefficient in clear oceans waters, as expected, is dominated by the absorption coefficient of pure water. In contrast, the second plot shows the dependence, especially towards the blue-green wavelengths, where a significant contribution from absorption due to phytoplankton, non-algal materials, and CDOM can be seen. This also explains the blue color of clear ocean waters and the green color of more turbid coastal waters.

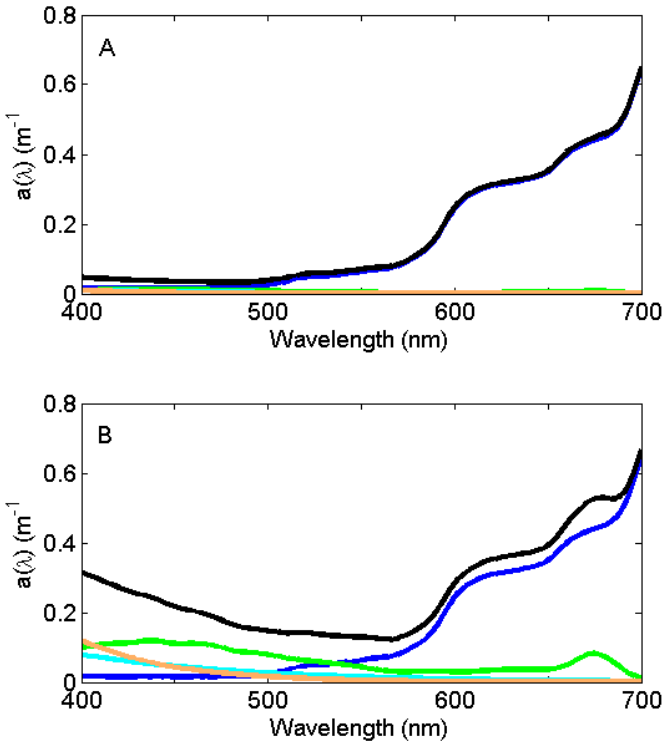

Figure 2.11: Total (black curve) and constituent absorption coefficients for clear oceans waters (top plot) and coastal waters (bottom plot). Coastal waters are more absorbing in the blue-green.

2.6 Link Budget

The goal of the link budget is to provide a baseline estimate of requirement estimates and performance metrics for free-space underwater optical communication. In this section, we first start from the transmitter with a given transmit power and work towards the receiver. We then use desired receiver performance and range to work back towards a required transmitter power. References [70], [71], and [72] were consulted for making this link budget.

2.6.1 Transmitter to Receiver

We assume an aligned point-to-point link. Such a system has three main sources of losses:

- Channel Loss
- Geometrical Loss
- Optical Loss

Hence the power at the receiver can be expressed as:

$$P_{RX}(\lambda, d) = T_C(\lambda, d) \cdot T_G(d) \cdot T_O \cdot P_{TX} \tag{2.23}$$

Although pointing losses are ignored here, they contribute a significant amount and is considered in a later section.

Channel Loss

For a theoretical approximation, Beer's Law provides a simple calculation for path loss. Beer's law is defined as:

$$T_C(\lambda, d) = e^{-c(\lambda) \cdot d} \tag{2.24}$$

where λ is wavelength of the transmitter source, d is the distance between the transmitter and the receiver. $c(\lambda)$ is defined as the attenuation coefficient and is the sum of absorption coefficient and the scattering coefficient and has units of m^{-1}. The product of attenuation coefficient and the distance, $c(\lambda) \cdot d$, is referred to as attenuation length and is a unitless term that expresses the exponential loss of light in water. Each attenuation length indicates an approximate loss of 63% of optical power.

Geometrical Loss

Consider the transmitter beam to have a divergence angle of θ_{div}. Let d between the perpendicular distance between the transmitter and the receiver. At that distance, the transmitted beam would have an area:

$$A_{TX} = \pi \left(d \cdot \tan \left(\frac{\theta_{div}}{2} \right) \right)^2$$

which can be approximated using the small angle approximation to:

$$A_{TX} = \frac{\pi}{4} \left(d \cdot \theta_{div} \right)^2$$

A receiver with diameter D_{RX} has an area:

$$A_{RX} = \frac{\pi}{4} D_{RX}^2$$

Geometric loss is then calculated as the ratio of receiver area to transmitter beam spot area at the receiver as:

$$T_G(d) = \frac{D_{RX}^2}{\left(d \cdot \theta_{div} \right)^2} \tag{2.25}$$

Optical Loss

Optical losses include losses from windows and lenses. Each uncoated surface typically attenuates approximately 4% of the incident light due to reflection.

Received Power

Combining the above loss terms, we can arrive at a simple expression for the optical power at the receiver.

$$\boxed{P_{RX}(\lambda, d) = \left(\frac{D_{RX}^2 \cdot e^{-c(\lambda) \cdot d} \cdot T_O}{\left(d \cdot \theta_{div} \right)^2} \right) P_{TX}} \tag{2.26}$$

2.6.2 At the Receiver

The received optical power is further corrupted by a variety of noise sources. The power calculations for signal and noise power are given below and used to obtain a Signal-to-noise ratio (SNR).

Signal Power

We assume baseband direct detection for the following calculations. As is typical for such a receiver, we assume the optical detector with a load R_L and gain G followed by a low-pass filter with bandwidth B.

The power collected by the receiver can be converted to a photodetector current equal to

$$i_{sig} = \left(\frac{\eta q}{h\nu}\right) P_{RX} \tag{2.27}$$

where i_{sig} is the photodetector output current, P_{RX} is the optical power collected by the receiver, η is the quantum efficiency of the photodetector, q is the charge of an electron, h is Planck's constant, and ν is frequency. The product of Planck's constant and the electromagnetic frequency gives the energy per photon and the combination of terms within the parenthesis is typically referred to as the photodetector intensity-to-current conversion factor.

With a load R_L and gain G the signal power is

$$\begin{aligned} P_{sig} &= (G i_{sig})^2 R_L \\ &= \left(G \left(\frac{\eta q}{h\nu}\right) P_{RX}\right)^2 R_L \end{aligned} \tag{2.28}$$

Noise Power

For the receiver, we assume to use a reverse biased Si PIN photodiode. The typical noise sources associated with such a receiver are flicker noise, current noise, dark current shot noise, photon fluctuation generation-recombination noise, and thermal noise.

Low frequency noises such as flicker noise and current noise can be ignored for AC coupled signals. Shot noise and generation-recombination noise due to noises directly proportional to the received current, background current, and dark current can be lumped together, but can be ignored for systems with gains that are not large.

Thus the total noise power is typically dominated by the thermal noise and can be given as

$$P_{noise} = 4kTB \tag{2.29}$$

where k is the Boltzmann's constant, T is room temperature in Kelvins, and B is the bandwidth of the low-pass filter.

Signal-to-Noise Ratio

Using the above equations for signal power and noise power, the approximate Signal-to-Noise ratio can be given as

$$\boxed{SNR = \frac{\left(G\left(\frac{\eta q}{h\nu}\right)P_{RX}\right)^2 R_L}{4kTB}} \tag{2.30}$$

For a communications receiver using On-Off-Keying (OOK), with a bit interval and employing a matched filter, we express the electrical signal sampled at the output of the matched filter as

$$y_i = P_{sig}T_b x_i + n_i \tag{2.31}$$

where P_{sig} is the received electrical power, T_b is the bit interval, $x_i \epsilon \{0, 1\}$ is the OOK modulated signal, and n_i is the additive white Gaussian noise (AWGN). We can define the electrical SNR, ρ as

$$\rho = \frac{E\left[s_i^2\right]}{E\left[n_i^2\right]} \tag{2.32}$$

Therefore,

$$\boxed{\rho = \frac{2E_s}{N_0}} \tag{2.33}$$

where E_s is the average energy of the signal component and is equal to $P_{sig}^2/2$ and $N_0/2$ is the noise power spectral density of the AWGN.

Thus, the optical SNR can depend on the receiver gain, field of view, efficiency and load. However, the electrical SNR is estimated at the output of the receiver matched filter and provides a consistent point of reference regardless of changes in the optical front-end, and hence is used in the comparison and evaluation of empirical data.

Chapter 3

Design and Prototype of Smart Transmitters and Receivers

This chapter presents the design of the proposed smart transmitters and receivers and discusses the details of the prototype built. First, a few design goals and requirements are discussed, followed by a survey of some existing systems and method that could be leveraged. Next, the design and conceptual operation is given as well as some of the design considerations that were made. Finally, the chapter concludes with a discussion of the front-end electronics that is part of the smart transmitters and receivers.

3.1 Design Goals

The primary goal of the receiver design has been to increase the field of view of a typical free-space optical front-end. As such a discussion of field of view and typical systems is first presented.

3.1.1 Geometrical Loss in Link Budget

The biggest losses in the link budget comes from the exponential path loss of light in water, and then from geometrical losses. In the simplest scenario of a well aligned and pointed system, consider the transmitter beam to have a divergence angle of θ_{div}. Let d be the perpendicular distance between the transmitter and the receiver. At that distance, the transmitted beam would have an area (approximated using the small angle approximation):

$$A_{TX} = \frac{\pi}{4} (d \cdot \theta_{div})^2$$

A receiver with diameter D_{RX} has an area:

$$A_{RX} = \frac{\pi}{4} D_{RX}^2$$

Geometric loss is then calculated as the ratio of receiver area to transmitter beam spot area at the receiver as:

$$Loss_G(d) = \frac{D_{RX}^2}{(d \cdot \theta_{div})^2} \tag{3.1}$$

Thus, it is desirable to have a large receiver aperture size. However, practical size, weight, and cost requirements limit aperture sizes.

3.1.2 Field of View and Pointing

One method of increasing aperture size is to use a light collecting lens in front of the smaller area optical detector. However, this limits the FOV of the receiver, adding additional pointing requirements.

The FOV of a typical photodiode can be between 60 to 120 degrees based on the type of packaging used. Adding a lens restricts the FOV severely, depending on the radius of the photodiode active area $r_{photodiode}$ and the focal length of the lens f_{lens} as:

$$\phi = 2 \cdot \tan^{-1}\left(\frac{r_{photodiode}}{f_{lens}}\right) \tag{3.2}$$

The FOV is mostly limited by the imaging property of the lens: as the incoming beam enters the lens off-axis, the focal point moves laterally as a function of the tangent of the angle. Beyond a particular off-axis angle, the focal point starts to "walk off" the photodiode active area.

Even without the restrictions of a limited FOV at the receiver, free-space optical communications are inherently point-to-point. Hence the performance of a practical system depends on how well aligned the transmitter and receiver are. While bigger platforms can afford dedicated gimbal systems, smaller platforms do not have the volume or energy budget for sophisticated pointing and tracking.

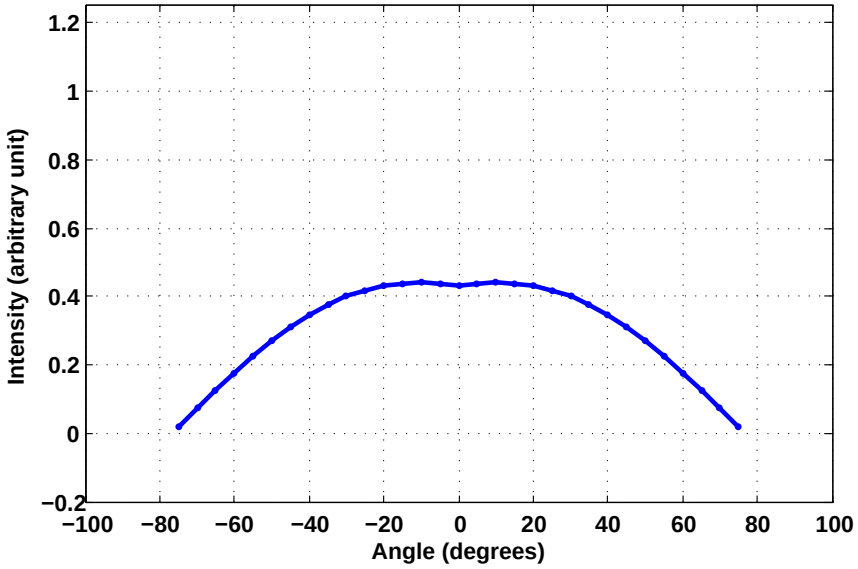

Figure 3.1: FOV of a bare photodiode without a lens. (Active area of photodiode used has a diameter of 2.65 mm).

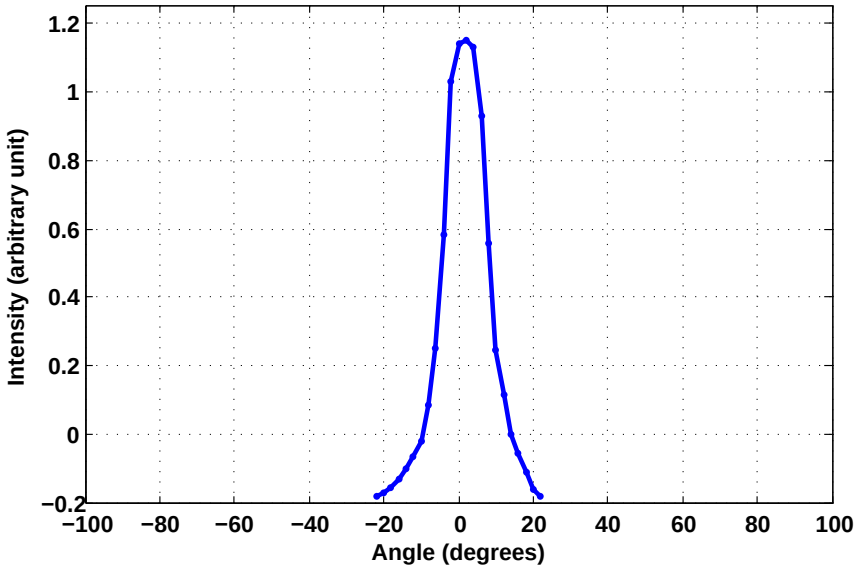

Figure 3.2: FOV of single lens-photodiode pair with single 1 inch lens and photodiode at focus of the lens. FOV decreases from $\sim$120° to $\sim$10°.

3.1.3 Existing Systems and Methods

In underwater optical communication

Wide FOV is typically achieved using very large aperture devices such as photomultiplier tubes (PMT). They have very short rise times and wide spectral response, including the blue-green window of interest in underwater optical communication. PMTs also have a wide range of aperture sizes ranging from 10 mm to as high as 500 mm (20 inches) in diameter. These large-area PMTs have been used in underwater optical communication systems to avoid active pointing and tracking [1].

Modulating retroreflector

A modulating retroreflector (MRR) can be used to address power, size, and pointing requirements at the receiver [73]. A MRR eliminates the need for a transmitting laser on the data-bearing platform and reduces the pointing requirements by retroreflecting the modulated light back to the interrogating source. For the underwater environment, we have built a MEMS Fabry-Perot MRR operating in the blue-green wavelengths and at data rates of 500 kbps and 1 Mbps [21]. This technology can also complement the diversity approaches described in Section III.

In indoor optical wireless

There has been some research in the domain of indoor optical wireless in the use of spherical photodiode arrays for increasing FOV [53]. Initial prototypes have been built and shown to be sufficient in low attenuation channels such as the indoor optical wireless channel [55].

The imaging property of a lens has been leveraged in the low attenuation indoor wireless channel by replacing the traditional single-element photodiode with a larger area segmented-photodiode [49], or by the use of a compound parabolic concentrator array. An improvement in range by a reduction in path loss, multipath distortion, and background noise has been shown by using such a system and by optimally combining the photodiode outputs [52].

In RF communications

Terrestrial RF communications have benefited from recent advancements in spatial diversity and smart antennas. A smart antenna is an antenna array with signal processing capable of 1. estimating direction of arrival and 2. beamforming. Advanced adaptive array systems are capable of focusing towards a desired signal while simultaneously nulling interferences. Mobile communications also provide insight towards some of the applications possible with an antenna with such capabilities. However, in optical systems, we do not have the RF advantage of being able to use coherent beamforming or phased arrays.

3.2 Smart Receiver

The goal of the smart receiver research is to develop a quasi-omnidirectional system to reduce pointing and tracking requirements typically associated with free-space optical systems. The compound eye type lens array that has been developed has segmented wide FOV, which allows for other benefits in addition to the original goals.

In addition to potentially reducing pointing and tracking requirements, this design also potentially allows one to estimate angle of arrival. This can be used in combination with a CDMA type multiple access system. Thus, potentially, signals from different platforms can be distinguished from their coded signals and have an indication of their position. This opens the door for a large number of applications such as localization, navigation assistance, and mesh networking. Using multiple input multiple output (MIMO) techniques, this optical approach potentially also provides angle and spatial diversity for improving the performance of point-to-point links. Previous work in this area shows ideal methods to combine the output of such an array of photodiodes such as to maximize signal and minimize noise, without loss in bandwidth [22].

As such, the smart receiver has the following characteristics:

- Increased field of view
- Angle of arrival estimation

3.2.1 Design and Conceptual Operation

The proposed design consists of a 3-D spherical array of lenses all focusing to a 2-D planar array of photodiodes. Close packing is achieved by using a hexagonal structure for both arrays. A prototype has been constructed using seven lenses and seven photodiodes. Figure 3.3 shows a solid rendering of the prototype lens head.

Figure 3.5 shows a sketch of light entering through a single lens and falling on multiple photodiodes. For the prototype lens head, with 7 lenses and 7 photodiodes, there are 49 such lens-photodiode pairs.

3.2.2 Design Considerations

The following section discusses the different aspects of the design and their importance to underwater free-space optical communication.

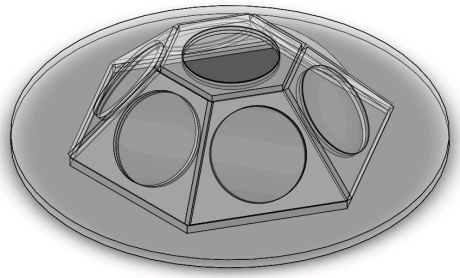

Figure 3.3: Isometric view of solid rendering of lens head. Not shown in rendering is planar photodiode array below the lenses. The truncated pyramid structure houses 7 lenses and 7 photodiodes below.

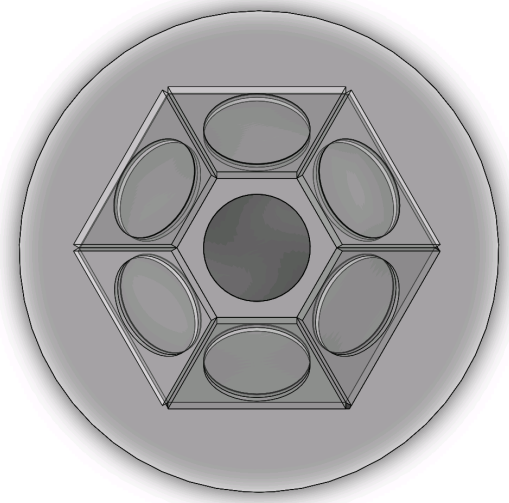

Figure 3.4: Top view of solid rendering of lens head. Not shown in rendering is planar photodiode array below the lenses. The truncated pyramid structure houses 7 lenses and 7 photodiodes below.

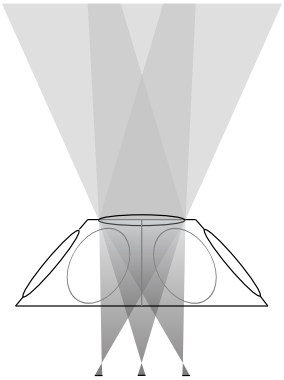

Figure 3.5: Sketch showing light entering through top lens and falling on multiple photodiodes. 49 such directions ("channels") exist for the prototype lens-photodiode array.

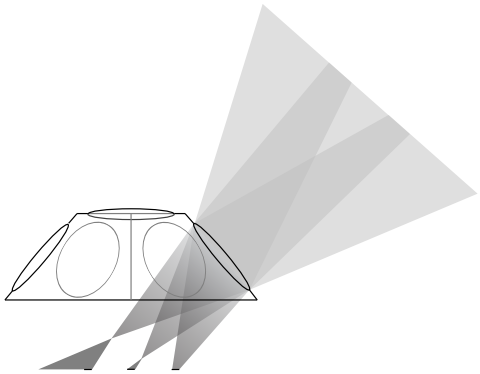

Figure 3.6: Sketch showing light entering through the side lens and falling on multiple photodiodes. 49 such directions ("channels") exist for the prototype lens-photodiode array.

(a) (b)

Figure 3.7: Image of (a) isometric view and (b) top view of the prototype lens array built.

Lens at the Receiver

Existing optical front-end arrays in free-space optics and indoor optical wireless use either photodiode arrays with no lenses, a single lens with multiple photodiodes, or multiple lenses focusing on separate photodiodes. The proposed design is novel in that it uses an array of lenses as well as an array of photodiodes, with multiple combinations of optical paths in between them.

Quasi-omnidirectionality

Increased FOV has been the primary design consideration for the optical front-end. Simulations and early experimental results show that the photodiode array under the middle lens increases the FOV from $\sim 5^\circ$ to $\sim 40^\circ$. The addition of the outer lenses at 130° with respect to the middle lens increases the FOV to $\sim 120^\circ$. The envelope of the combined FOV can be adjusted by additionally intentionally defocusing the photodiode array.

Angle of Arrival Estimation

The intensity of light received by each photodiode can potentially be used to roughly estimate the angle of arrival of light incident on the lens-photodiode array.

Photodiode Output Combining

Output combining is an important consideration for the performance of the system. The simplest interface to the array of photodiodes would be to connect them in parallel. This would allow a

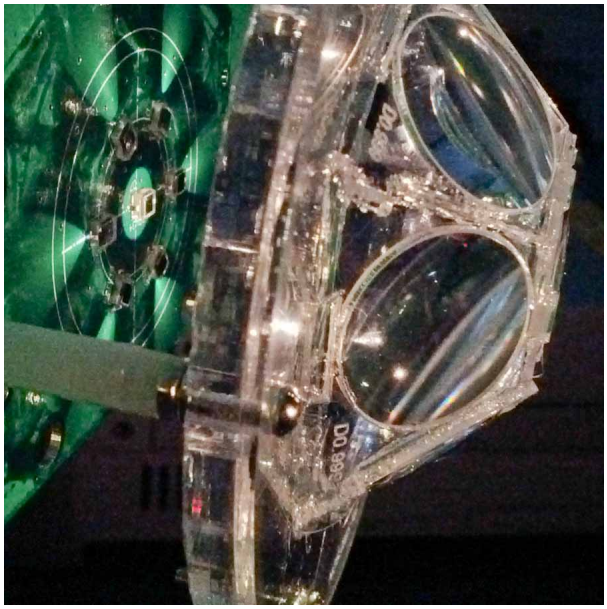

Figure 3.8: Picture of lens-photodiode array with light incident normal to the middle lens. Photodiodes array on the PCB can also be seen where focus lies above the middle photodiode.

single output to be digitized for processing. However, the total capacitance would be the sum of the individual capacitances resulting in a much lower bandwidth. An ideal combining technique would maintain bandwidth, minimize noise, and maximize SNR.

Two simple linear diversity combining techniques are equal gain combining (EGC) and maximum selection combining (SEL). In an equal gain combiner, the receiver output signals are summed with equal weights to generate the combined signal. This can be represented as

$$\hat{y} = y_1 + y_2 + \cdots + y_n \tag{3.3}$$

In selection combining, the receiver with the largest signal power at each instant of time is chosen as the combined signal. The combined signal is therefore

$$\hat{y} = \max\left(y_1, y_2, \cdots, y_n\right), \tag{3.4}$$

where y_1 is the signal at the first receiver, y_2 is the signal at the second receiver, and y_n is the signal at the n^{th} receiver.

3.3 Smart Transmitter

The smart transmitter has the following characteristics:

- Increased directionality
- Electronic switched beam steering

3.3.1 Design and Conceptual Operation

Similar to the smart receiver, the smart transmitter consists of a truncated hexagonal pyramid with seven LEDs. Unlike the receiver, each LED is coupled with its own lens that converges the wide FOV of the LED to a narrower beam in a particular direction. Each LED is uniquely addressed and driven, which allows the modulator to select an output direction. This forms the mechanism for a simple switched beam steering at the transmitter.

For a multi-user environment, it is important to provide multiple access to the medium. LEDs at different wavelengths can be used, but receivers would need multiple filters. Time Division Multiple Access would require synchronous clocks. Among asynchronous methods, Code Division Multiple Access (CDMA) was chosen as the multiple access scheme.

3.3.2 CDMA Coding

CDMA techniques have been extensively studied and used in RF communications. Incoherent optical detection and processing make typical RF maximum length and Gold code sequences not ideal. The on-off-keying modulation methods in optical communication are unipolar as opposed to the bipolar modulation required by Gold codes. Instead optical CDMA typically uses prime codes [74].

Prime codes of length $N = P^2$ are obtained from prime sequences of prime number length P generated from a Galois Field $GF(P)$. Here we use $P = 5$ to generate a code of length 25, which is then zero padded to $N = 32$. The code was simulated for $K = 5$ users. The theoretical SNR can be calculated using the below equation [74] as 14.4 dB.

$$SNR_{prime,th} \approx \frac{1}{0.29}\left[\frac{N}{K-1}\right] \tag{3.5}$$

Figure 3.10 shows the autocorrelation and cross correlation function for the data sequence 111001010 coded with the prime code. The empirical SNR is obtained as the ratio of the square of the maximum of the autocorrelation function to the sum of the variances of the cross correlations with the interferers, and found to match the theoretical SNR.

(a) (b)

Figure 3.9: Image of (a) isometric view and (b) top view of the prototype LED array built.

The particular length prime code chosen allows for 5 simultaneous users. This is sufficient for the initial prototype. A longer code sequence will decrease overall bandwidth but allow for more users with a corresponding increase in SNR.

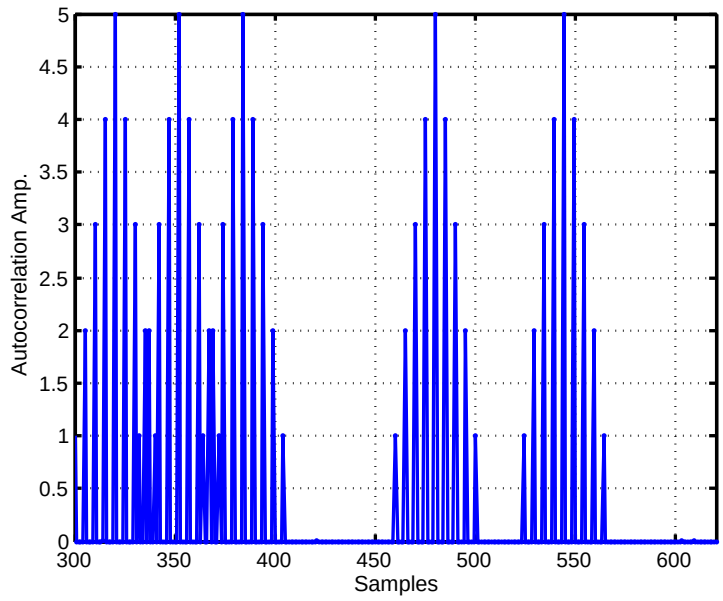

(a)

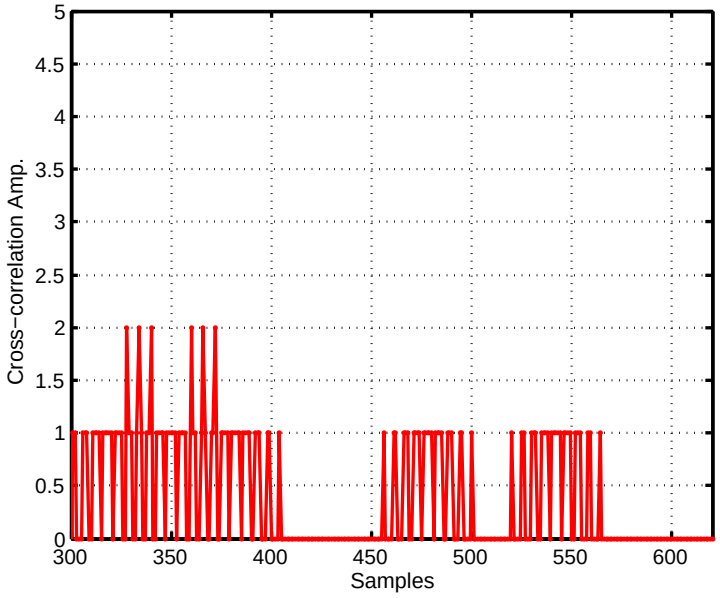

(b)

Figure 3.10: Simulation correlator outputs for the data sequence 111001010 spread using a 32 chip prime code sequence of P = 5 with 7 padding zeros.

3.4 Multi-Channel Front-End Electronics

The smart transmitters and receivers require a multi-channel front-end electronics to interface with the digital signal processor. Keeping the channel path separate is required for most of the benefits of the smart transmitters and receivers as previously mentioned in Sec. 4.1. For the receiver, this implies not combining the received signals till it is digitized, and for the transmitter, this implies being able to send different data streams simultaneously across the different outputs.

3.4.1 Smart Receiver Multi-Channel Front-End Electronics

For the smart receiver, each of the photodiode outputs are digitized separately for the digital signal processor. We have previously mentioned how connecting the photodiodes in parallel to sum the output currents, although simple in implementation, would decrease the bandwidth of the photodiodes. One could convert the individual current outputs to voltage and then use a summing amplifier to add them. However, this would also add unnecessary noise from each channel, decreasing the combined signal to noise ratio. In either case, the digital signal processor would not have access to the separate photodiode outputs.

Hence one of the first requirements of the receiver front-end electronics is to have a multi-channel interface between the lens-photodiode array and the digital signal processor. The front-end also needs to achieve this without limiting the bandwidth per channel. Careful consideration also needs to be given to the gain on the signal path. A variable gain amplifier is useful for implementing an automatic gain control circuit. Also, the gain is required to be high during backscatter estimation of the water quality as the amount of backscattered return light from a co-located transmitter is small. It is also ideal for the receiver to be DC-coupled so as to estimate absolute values of power received by the photodiodes. However, the amount of dynamic range required by the front-end is relaxed by the use of AC-coupling.

Finally, a multi-channel, high-sampling-rate analog-to-digital converter is required to simultaneously digitize the conditioned analog outputs. The challenge of implementing such a system involves handling the huge amounts of data generated. For the 7-channel lens-photodiode array prototyped in this research, the 12-bit analog-to-digital converter, operating at a sampling rate of 65 MSps, generates 7 simultaneous streams of 780 Mbps for a combined rate of 5.46 Gbits/s. This is reasonable for a well designed interface board and a powerful digital signal processor, but also illustrates one of the reasons to limit the number of channels at the front-end.

Based on these requirements, for the purposes of prototyping, two different receiver front-end electronics boards were designed and built. A 7-channel, fixed gain, DC-coupled system with analog outputs, and a 7-channel, variable gain, AC-coupled system with an on-board octal analog-to-digital converter were both designed and built. The receiver with converter outputs the digitized samples over low-voltage differential signaling. In the absence of a fast digital signal

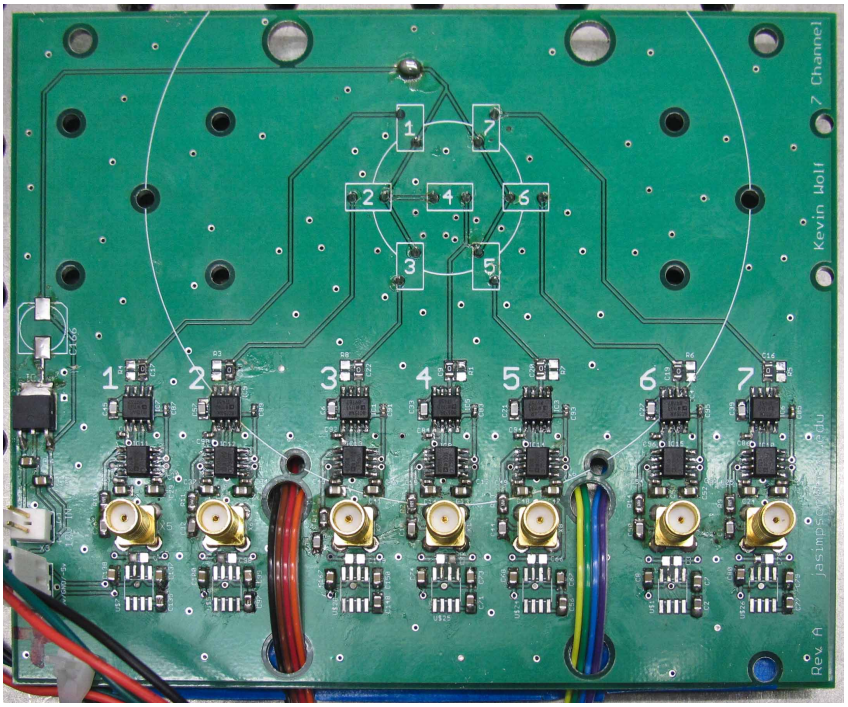

Figure 3.11: 7-Channel receiver PCB.

processor with the same input interface standard, that board is not used for the rest of the work presented in this research. The system architecture of the 7-channel analog-output receiver is next discussed.

3.4.2 7-Channel Receiver Architecture

The 7-channel receiver has seven photodiodes, all of which are referred to negative supply. The current output from the photodiodes are converted to a differential voltage output using a transimpedance amplifier. The transimpedance amplifier has an input bias voltage of 1.8 V below its positive power rail. Therefore, referring the photodiode to the negative supply introduces a larger reverse bias voltage across the photodiode, which decreases the photodiode's capacitance, thereby increasing bandwidth. Using a differential output configuration on the transimpedance amplifier effectively doubles the gain of the amplifier by increasing its trans-resistance from $\sim$10 kΩ to $\sim$20 kΩ. This is also ideal for the variable gain amplifier and the input of the analog-to-digital converter, both of which are differential. However, for the analog-output receiver, a differential receiver amplifier is used to employ differential to single-ended conversion, so as to bring the output to an SMA connector.

The photodiodes used is an Osram BPW34, which has a relatively large active area of

7 mm^2. The rise time of this particular photodiode is 20 ns, corresponding to a bandwidth of ∼17.5 MHz. The photodiodes can be easily changed to faster diodes for wider bandwidth. The transimpedance amplifiers used are the Analog Devices AD8015 and they have a bandwidth of 240 MHz. The differential receivers are the Analog Devices AD8130 and they have a bandwidth of 270 MHz. For the receiver with the on-board analog-to-digital converter, the variable gain amplifiers used are the Analog Devices AD8369, which has a 45 dB range in gain in increments of 3 dB. The data converter used is the Maxim MAX1438 octal converter, which has 12-bits per channel and a simultaneous sampling rate of up to 65 MSps. For external analog-to-digital conversion, two different digitizers are used. The first is a National Instruments NI USB-6009, which has 8 14-bit analog inputs at a maximum sampling rate of 48 kSps. The second, which is used for data transmission tests, only has 2 channels, but has an 8-bit resolution sampling rate of up to 100 MSps per channel.

3.4.3 Smart Transmitter Multi-Channel Front-End Electronics

For the smart transmitter, the digital signal processor is capable of simultaneously sending different streams of data across its multiple LED outputs. Additionally, the LED array has LEDs positioned in different output directions, and the front-end electronics achieves beam steering between the different outputs by switching or selecting between the different output LEDs. Being able to send different data streams across the different outputs will enable the smart transmitter to implement a variety of space-time block codes, and/or also send different data streams to different users in a multiuser scenario. Being able to select and switch between the output LEDs will allow the transmitter to beamform (by focusing its output as opposed to a diffused output) and beam steer (by selecting direction) its output.

Hence, multi-channel outputs are one of the first requirements of the transmitter front-end electronics. The transmitter also needs to be capable of driving a high-current output. The LEDs used are capable of be driven with a continuous current of up to 700 mA, which is used as the target maximum output current requirement per channel. Also to be considered is the total output current of 4.9 A (across the LEDs alone) if and when all output LEDs are switched *on* simultaneously at maximum output. The on-board power conditioning circuits, and off-board power source has to be capable of providing this peak maximum current. Dual-rail power supplies capable of providing instantaneous current outputs at 5 A is hard and hence single-rail devices in the high-current output path are ideal.

The ideal method of driving an LED, as in the case of driving a diode laser, is to use a bias-current to bias the output intensity of the LED and modulate about that current bias. A bias tee network is the preferred method of implementing this. However, in this case, such a bias tee would need to operate in the relatively low bandwidth of the LED as well as handle the

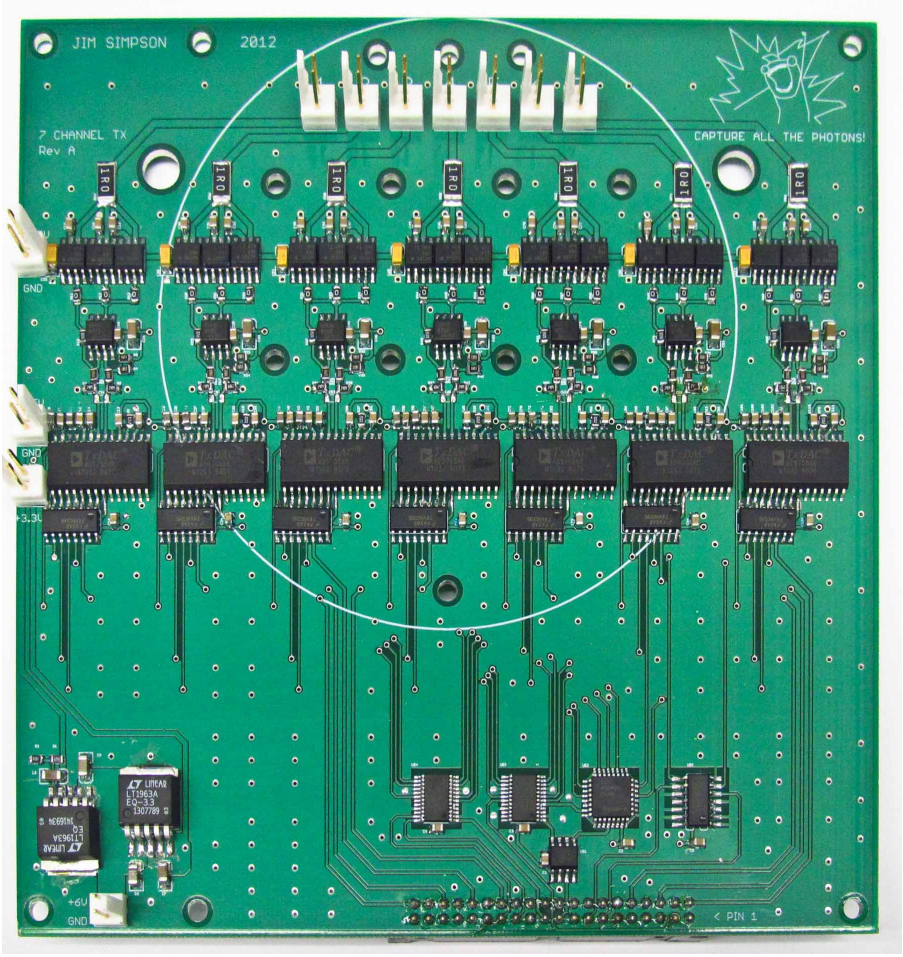

Figure 3.12: 7-Channel transmitter PCB.

high output current required. Based on these requirements, a 7-channel, 10 Mbps, 750 mA/ch. using a new digital-to-analog converter (DAC)-based topology for bias tee is designed and built.

3.4.4 7-Channel Transmitter Architecture

The 7-channel transmitter has 7 LED outputs. The LEDs are driven using a newly designed DAC-based bias tee circuit. As opposed to a conventional bias tee, here a bias voltage is set and modulated in the digital domain on the digital signal processor. The modulated output is converted to an analog voltage using the DAC. This output is then fed to the input of a high-current driver, the output of which drives the LEDs. Most high update rate ($>$ 100 MSps) DACs are current output DACs and hence an intermediate current-to-voltage conversion is implemented on a voltage-feedback amplifier placed between the DAC and the current drivers.

This amplifier also adds an additional gain stage to match the DAC output to the levels needed by the current driver. Finally, the current driver is implemented using high-output current, fixed-gain, buffer amplifiers. Most high-output current buffer amplifiers operate on dual-rail power supplies. Here, instead we use three single-rail 250 mA maximum output current amplifiers in parallel to achieve the desired 750 mA output current per channel.

Each DAC is an 8-bit, parallel-input DAC. For sending different data streams, all 7 DACs will require a total of 56 digital output lines alone for the data bits. This is reasonable for a single board solution. However, in our prototype, the digital signal processor is on a separate board from the transmitter front-end, connected through a ribbon cable that does not support that high number of digital lines. Hence an 8-bit parallel-in serial-out shift-register with output-latches is used to drive each DAC's data bits. The downside of this method is that each serial line operates at 8 times the effective data rate. For a maximum data rate of 10 Mbps this equals 80 Mbps per serial line for each channel. However, this is reasonable for a ribbon cable and the digital signal processor is capable of driving 7 outputs at 80 Mbps for a combined effective output rate of 560 Mbps.

The challenge, however is that there is a total of three clock lines per channel. It is ideal (to maximize rise time of the output signal) to drive the DAC clock at its maximum of 125 MHz. The shift-register has an input clock that operates at 8 times the data rate at up to a maximum of 80 MHz and and output clock that operates at the data rate of up to 10 MHz. Since the clock lines are shared between the channels and are generated off-board, a dedicated clock distribution circuit is necessary to drive the total of 21 clock lines, while minimizing crosstalk between the clock lines. This is achieved using a network of clock distributions ICs composed to the Integrated Device Technology ICS8302, MPC9447, and two IDT5V928 devices.

The LEDs used are from the Luxeon Rebel series and depending on their manufacturing binning up to a maximum constant output power of 740 mW optical power for a maximum constant output current of 700 mA. The shift register with output latches used are the Fairchild Semiconductor 74VHC595, which for the 3.3V VHC logic family has an operating frequency rating of at least 80 MHz, the minimum required in this application for the target data rate, and a typical operating frequency of 150 MHz. The DAC used is an Analog Devices AD9708, 8-bit, 125 MSps DAC. The voltage feedback amplifier is an Analog Devices AD8041 rail-to-rail amplifier which has a bandwidth of 160 Mhz, and the high-output current amplifier is a Texas Instruments OPA 692, which has a bandwidth of 225 MHz.

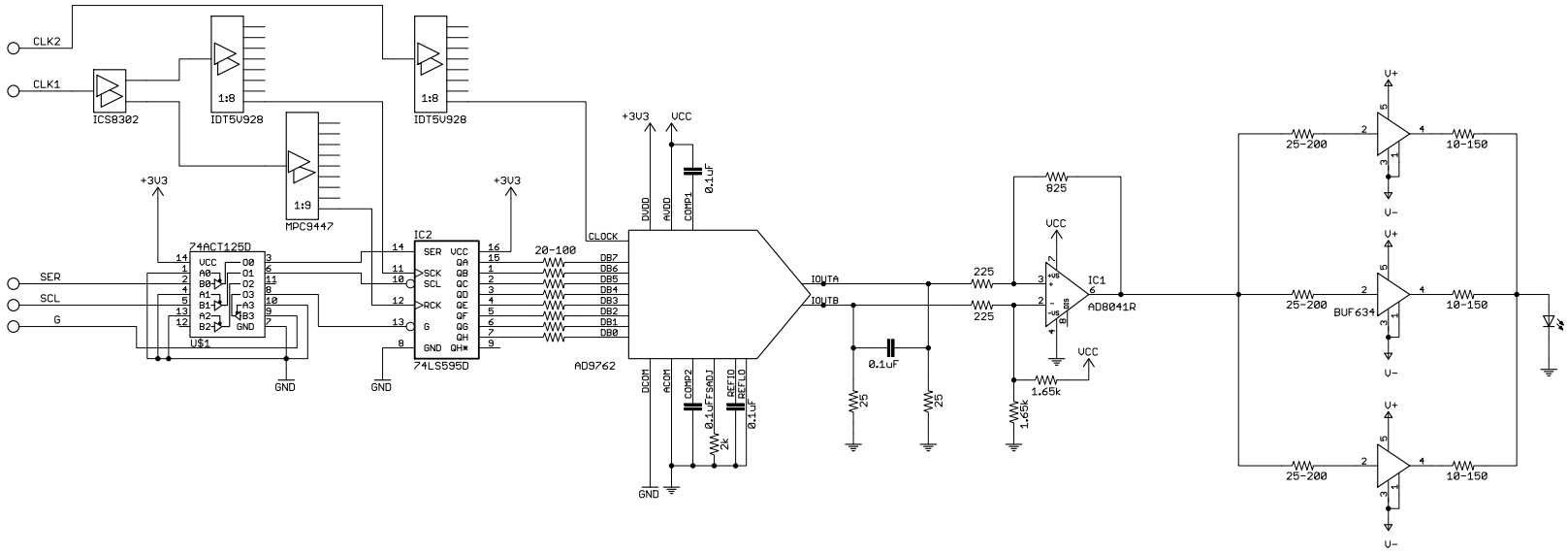

Figure 3.13: Schematic of one of the channels of the 7-Channel transmitter using the DAC-based bias tee LED driver.

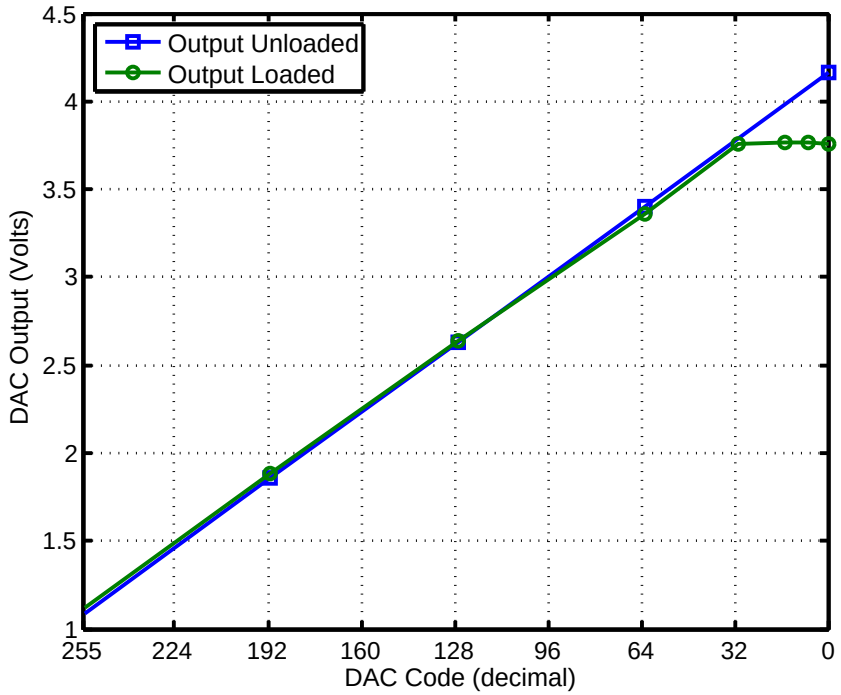

(a)

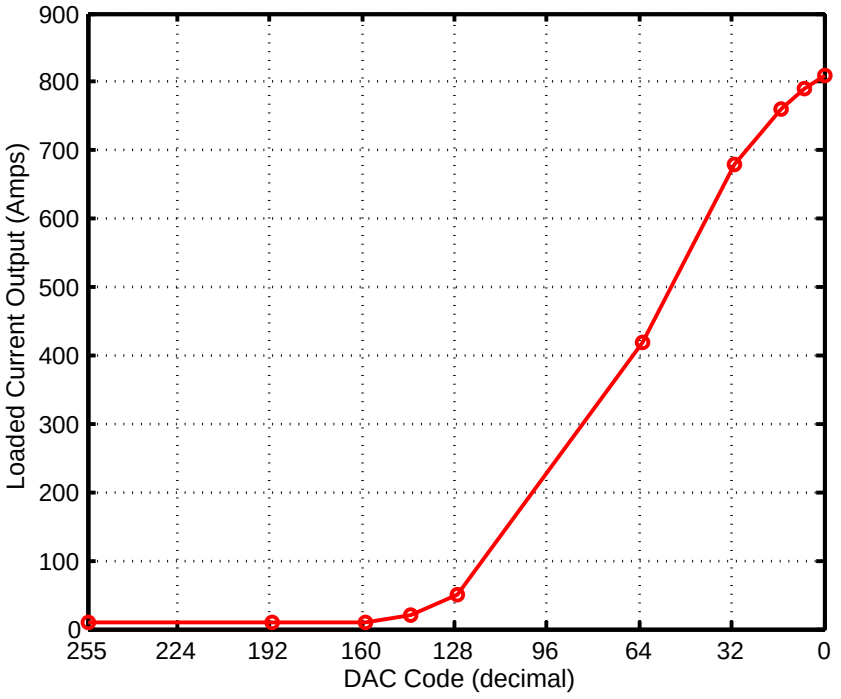

(b)

Figure 3.14: Output (a) voltage and (b) current performance of DAC-based bias tee LED driver.

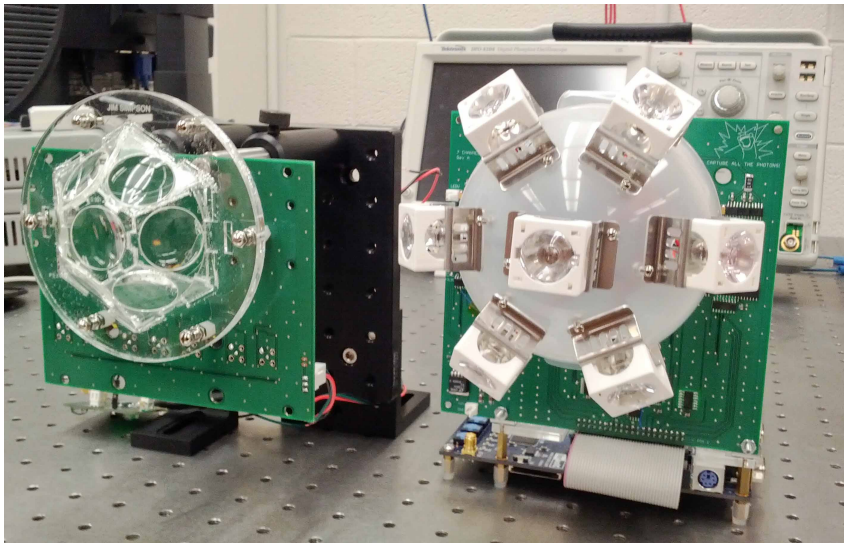

Figure 3.15: 7-Channel receiver (left) and 7-Channel transmitter (right) placed side-by-side.

3.5 Conclusion

We have proposed and demonstrated new optical front-ends for smart transmitters and receivers for underwater free-space optical communication. The smart receivers have increased field of view and the ability to estimate angle of arrival. The transmitters are quasi-omnidirectional, allow electronic switched beam steering, and with an adjacent receiver, enable estimation of water quality by measuring the optical backscatter from transmitted light. This smart transceiver approach mitigates pointing and tracking requirements, which can be difficult for underwater platforms and enable adaptive communication techniques, which are expected to be useful due to the variable dynamic range of the communications signal as platforms change relative range and pose. Thus, we anticipate that implementations such as those presented combined with CDMA and other coding techniques will be useful in enabling a physical layer for networking schemes in swarms of unmanned underwater vehicles in the future.

Chapter 4

Modeling and Simulation of Smart Transmitters and Receivers

The goal of this chapter is to understand the behavior of the lens-photodiode array at the smart receiver front-end and the LED array at the smart transmitter front-end. In either case, a model will primarily allow to visualize the sensitivity pattern of the receiver and the radiation pattern at the transmitter, and help validate the design chosen for the prototype.

4.1 Lens-photodiode Array Modeling

A model of the lens-photodiode array system is built in MATLAB and used to simulate light incident of the system to observe:

- the power at the face of each lens,
- the power at the receiver plane underneath the lens-array,
- and finally, the power at each photodiode.

A description of the model and simulation mechanics is first provided, followed by a discussion of the results.

4.1.1 Modeling and Simulation Setup

The geometry and mechanics of the model and simulation is described. The simulation parameters match those of the prototype constructed and vice-versa. Hence the goal of the model and simulations is to verify and validate the selection of parameters as well as to visualize the intermediate results not obtainable from experimental results.

Geometry

A co-ordinate system is first presented to describe light incident on the lens-photodiode array. The system is based on spherical co-ordinates and uses the conventions as shown in Figure 4.1. Zenith angles, described using θ, start from the z-axis towards the x-y plane, and range between 0 and $\pi/2$. Azimuth angles, described using ϕ, start from the x-axis towards the y-axis, and range between 0 and 2π.

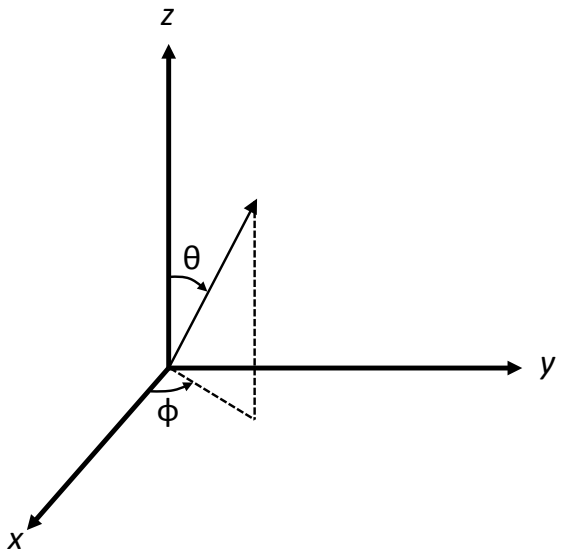

Figure 4.1: Geometry used for describing system.

Field of view (FOV) of the system is described by the solid angle of the inverted cone with apex angle 2θ and is given as:

$$\Omega = 2\pi\left(1 - \cos\theta\right) \tag{4.1}$$

Maximum FOV is achieved for $\theta = \pi/2$ with a corresponding solid angle of $\Omega = 2\pi$ steradian. The global co-ordinate is defined as the co-ordinate system at the center of the middle lens as shown in Figure 4.2. The reason for this is that the middle lens is the only lens that shares a common axis with the imaginary center of the receiver. Thus, no rotation transformations are necessary in describing angles at the middle lens w.r.t. the imaginary center of the receiver. Figure 4.2 also shows the global co-ordinates as transformed on to the other lens faces. Details on the transformation is provided in Section 4.1.1.

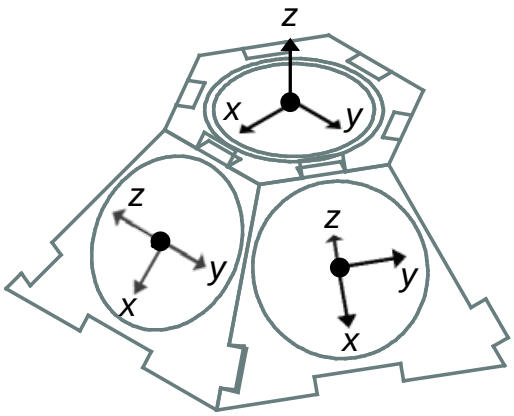

Figure 4.2: Origin transformation for each lens. Global co-ordinates are at the center of the middle (top) lens.

Naming conventions for the 7 lenses and the 7 photodiodes are shown in Figure 4.3 and Figure 4.4 respectively. It is to be noted that lenses 2, 4, and 6 as well as photodiodes 2, 4, and 6 all lie along the same axis (x-axis). Lenses and photodiodes 3, 4, and 7 lie along an axis rotated $\phi = 60°$ from the x-axis. Lenses and photodiodes 5, 4, and 1 lie along an axis rotated $\phi = 120°$ from the x-axis.

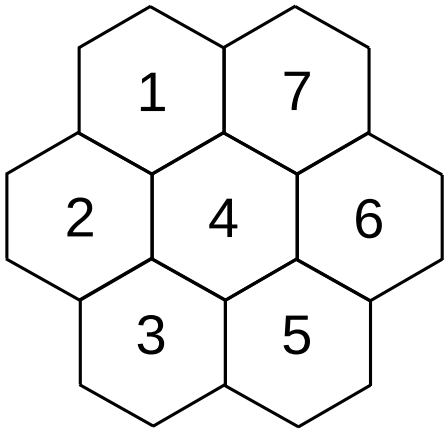

Figure 4.3: Naming convention for lenses and photodiodes.

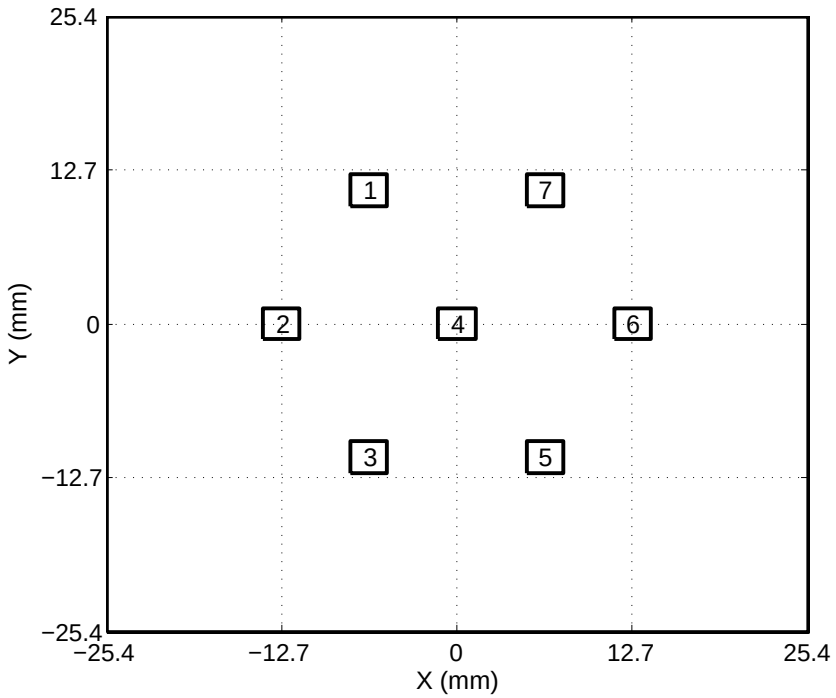

Figure 4.4: Position and naming convention for photodiode array.

Mechanics

The mechanics of the model and its simulations are given below.

1. The simulations runs in a triple nested for-loop. The outermost loop iterates through each of the 7 lenses one at a time. Calculations are done for each separate lens before being combined together. The middle loop iterates through all θ for 0 to $\pi/2$. The innermost loop iterates through all ϕ from 0 to 2π.

2. The power of the light source as observed at the global co-ordinate (middle lens) is first calculated as P_s. It is represented as a vector with the first three components representing its x, y, and z components. The fourth components is useful in accounting for linear translations between the lenses.

$$P_s = \begin{bmatrix} \sin\theta * \cos\phi \\ \sin\theta * \sin\phi \\ \cos\theta \\ 1 \end{bmatrix} \tag{4.2}$$

3. A rotational transformation from the origin of each lens as shown in Figure 4.2 is done to the global co-ordinate to find the power observed at the face of each of the lenses.

$$P_n = R_y \cdot R_z \cdot P_s \tag{4.3}$$

where R_z is the standard rotation matrix about the z-axis:

$$R_z = \begin{bmatrix} \cos\alpha & -\sin\alpha & 0 & 0 \\ \sin\alpha & \cos\alpha & 0 & 0 \\ 0 & 0 & 1 & 0 \\ 0 & 0 & 0 & 1 \end{bmatrix} \tag{4.4}$$

and R_y is the standard rotation matrix about the y-axis:

$$R_y = \begin{bmatrix} \cos\beta & 0 & \sin\beta & 0 \\ 0 & 1 & 0 & 0 \\ -\sin\beta & 0 & \cos\beta & 0 \\ 0 & 0 & 0 & 1 \end{bmatrix} \tag{4.5}$$

From this calculation, and the geometry, the incident light angle, as seen by each lens is

calculated by:

$$\theta_n = \tan^{-1}\left(\frac{\sqrt{P_{n,x}^2 + P_{n,y}^2}}{P_{n,z}}\right) \tag{4.6}$$

The power of that incident as observed across the face of the lens is then calculated as:

$$P\{n\}(\theta,\phi) = Area_{lens} * \cos(\theta_n) \tag{4.7}$$

4. The focal point behind each lens is then calculated using the optical invariant. This point is with respect to the local co-ordinate of the lens. Hence it is transformed back to the global co-ordinates using both rotational and translation transformations similar to the previous step to obtain (x, y) of focal point with respect to global co-ordinates.

5. Since at each iteration point, the corresponding (x, y) and (θ, ϕ) are known, a rearrangement of powers is done.

$$P_{x,y}\{n\}(x,y) = P_{x,y}\{n\}(x,y) + P\{n\}(\theta,\phi) \tag{4.8}$$

Also, since this is analogous to a histogram where powers from different incident angles are placed in (x, y) bins, a weighting of the histogram is done by scaling the final power in each bin by the number of such different incident angles were observed in each bin.

6. Finally, the power at each photodiode active area is calculated by integrating the previously obtained x and y values for the area and location of each photodiode. However, since at each iteration instance, the lens through which the incident light focused on the receiver plane is also known, the power at each photodiode is also stored as a function of the lens.

4.1.2 Modeling and Simulation Results

The results obtained from the modeling and simulation can be grouped in to four main results.

1. Power at the lens surface
2. Power at the receiver plane
3. Power at the photodiodes
4. Power through each lens-photodiode pair

The results are analyzed for each of these sections in detail below. All of the plots discussed in this section appear at the end of the section.

Power at the lens surface

Results for power at the lens surface are given in Figures 4.5 and 4.6. The three-dimensional space is described by a spherical surface with spherical co-ordinates as described in the previous geometry for (θ, ϕ) which are described with respect to the global co-ordinates located at the middle of the middle lens (Lens 4).

Figure 4.5 shows the sensitivity of each lens to solid angles in three-dimensional space. This validates the arrangement and configuration of the lenses to cover (for a zenith angle, $\theta = pi/2$) sensitivities to a solid angle, $\Omega = 2pi$ steradian. This is without consideration of the photodiode array positioning and hence regardless of the receiver arrangement. Figure 4.6 is a top-view of this same set of plots.

Power at the receiver plane

Results for power at the receiver plane are given in Figures 4.7, 4.8, and 4.9. All three sets of plots visualize the receiver plane on the x-y plane as a 50 mm^2 area centered at $(0, 0)$ which lies centered 40 mm underneath the middle lens (global co-ordinate). The intensity in each plot is a normalized intensity at each (x, y).

The three-dimensional plot in Figure 4.7 helps visualize this intensity change. The two-dimensional plot in Figure 4.8 helps visualize the position of the focal points on the receiver plane. Figure 4.9 helps visualize the combined sum of focal points and intensities from all 7 lenses. Both two-dimensional sets of plots also overlay the placement of the photodiodes. The goal is to suggest and validate positioning of photodiodes to maximize light collected while also maximizing separation between photodiodes.

Power at the photodiodes

Results for power at the photodiodes are given in Figure 4.10 as well as the next sub-section. Power at photodiodes are obtained by integrating the intensities on the receiver plane for the location and area of each photodiode. The biggest connection attempted to be made is the connection between this power and the field of view (FOV) of each photodiode. Figure 4.10 illustrates this combined FOV as a function of the spherical global co-ordinates.

Power through each lens-photodiode pair

Results for power at each lens-photodiode pair are given in Figures 4.11, 4.12, and 4.13. As in the previous sub-section, the goal of these plots is to make the connection between photodiode output power and field of view (FOV).

Light enters through each of the 7 lenses and can fall on up to 7 photodiodes for a total of 49 lens-photodiode pair FOVs. Angles on the plot x-axis span -90° to 90° with its connection to the global spherical co-ordinates shown in Table 4.1.

Table 4.1: 2-D angles for all ϕ

Angles	Zenith angles	Azimuthal angles
-90° to 0°	$\theta \in [0, \pi/2]$	$\phi \in [3\pi/2, \pi/2)$
0° to 90°	$\theta \in [0, pi/2]$	$\phi \in [pi/2, 3\pi/2)$

For the one-axis plots, the chosen axis lies along the x-axis and runs through lenses (and photodiodes) 2, 4, and 6. Light enters through each of the 7 lenses and can fall on up to 7 photodiodes for a total of 49 lens-photodiode pair FOVs. Angles on the x-axis span -90° to 90° with its connection to the global spherical co-ordinates shown in Table 4.2.

Table 4.2: 2-D angles for fixed ϕ

Angles	Zenith angles	Azimuthal angle
-90° to 0°	$\theta \in [0, \pi/2]$	$\phi = 0$
0° to 90°	$\theta \in [0, pi/2]$	$\phi = \pi$

Figure 4.13 is the one-axis photodiode outputs for the scenario in Figure 4.12. The color coding is consistent between the plots and helps to illustrate that the photodiode outputs for the system configuration chosen simultaneously includes different smaller FOVs.

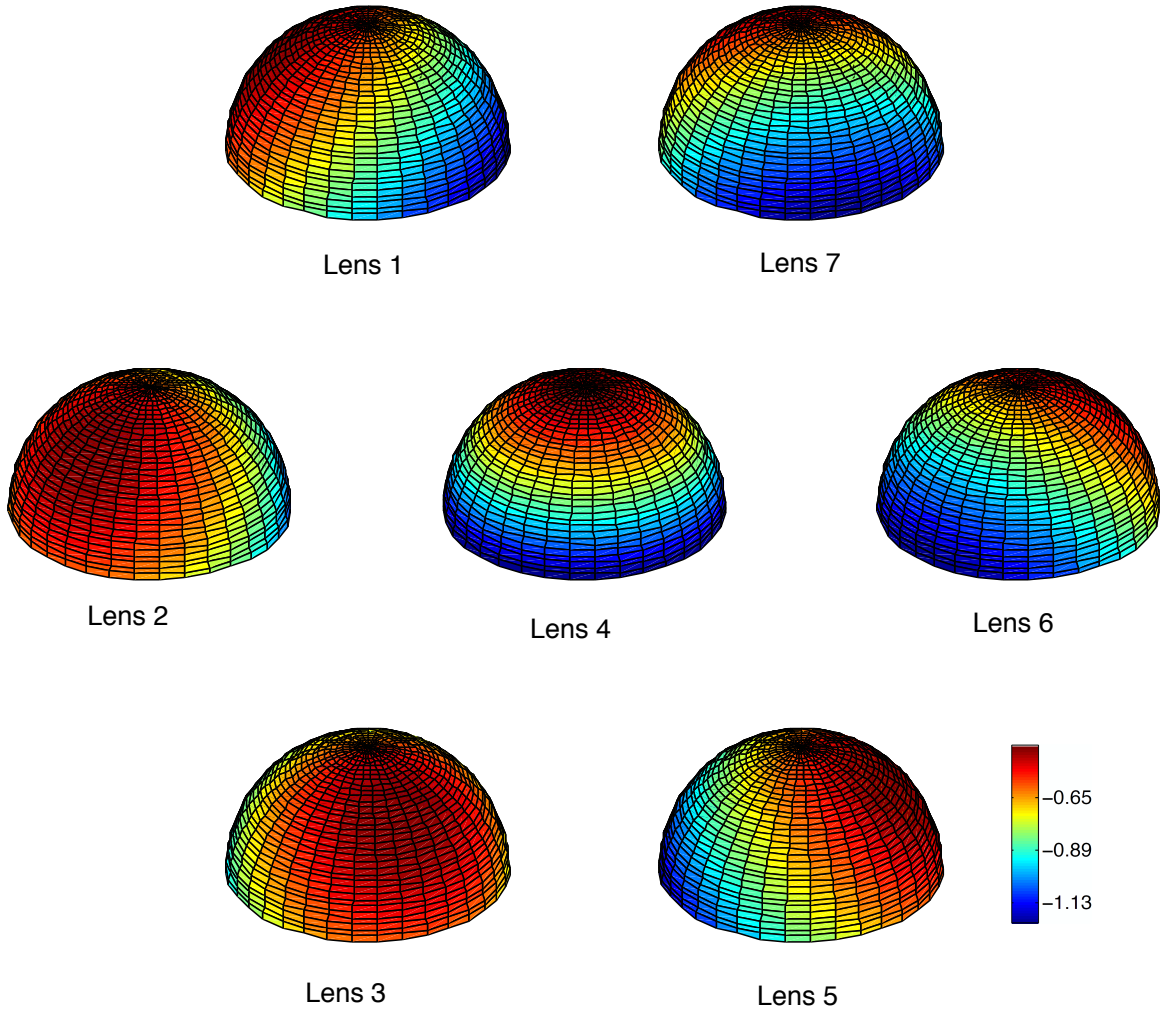

Figure 4.5: Sensitivity of each lens to solid angles in three-dimensional space. (Graphs are positioned according to lens numbering and arrangement.) This plot validates the arrangement and configuration of the lenses to cover (for a zenith angle, $\theta = \pi/2$) sensitivities to a solid angle, $\Omega = 2\pi$ steradian. Note that this is without consideration of the photodiode array positioning and hence regardless of the receiver arrangement.

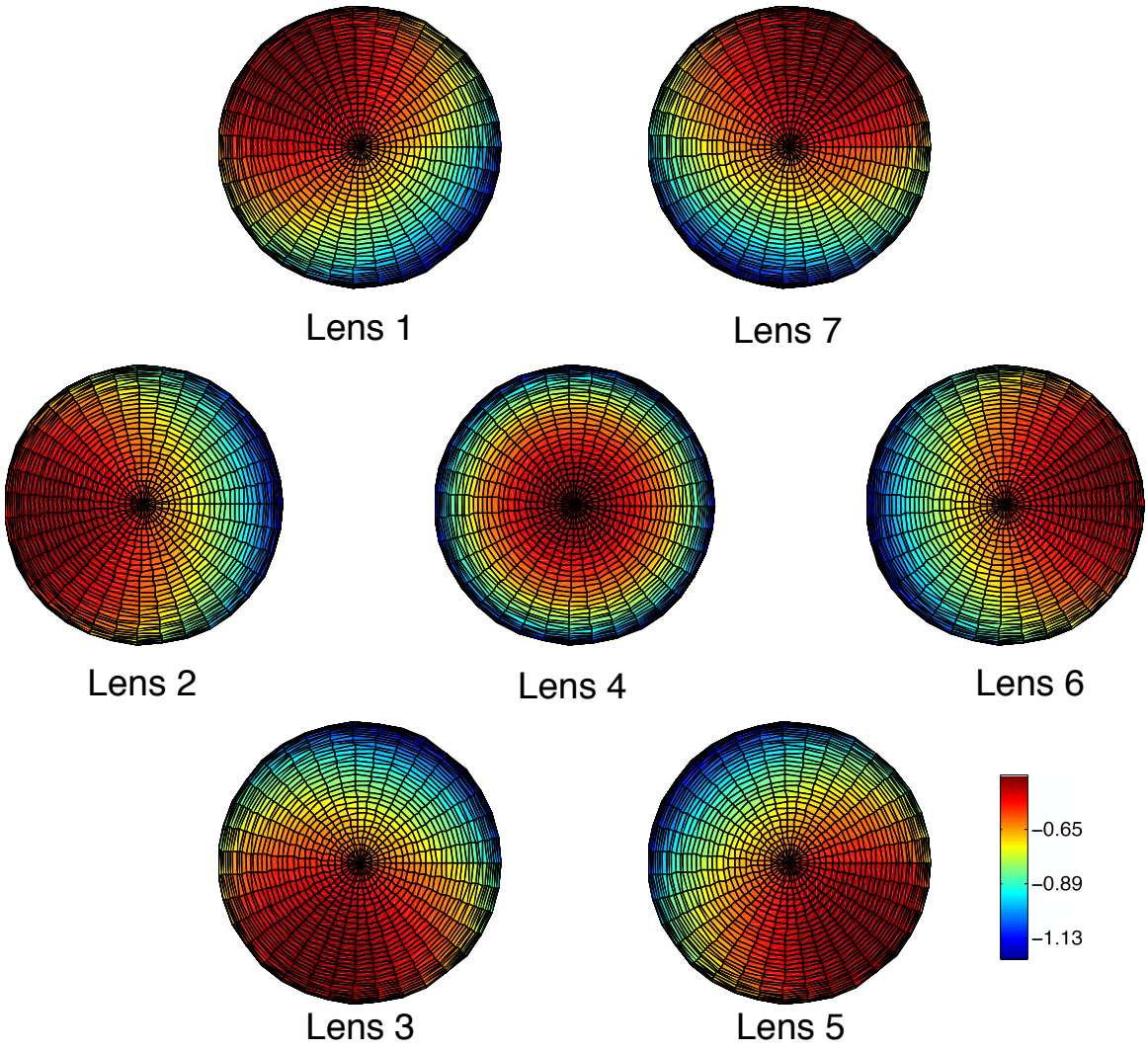

Figure 4.6: Top view of sensitivity of each lens to solid angles in three-dimensional space (previous plot). (Graphs are positioned according to lens numbering and arrangement.) This plot validates the arrangement and configuration of the lenses to cover (for a zenith angle, $\theta = \pi/2$) sensitivities to a solid angle, $\Omega = 2\pi$ steradian. Note that this is without consideration of the photodiode array positioning and hence regardless of the receiver arrangement.

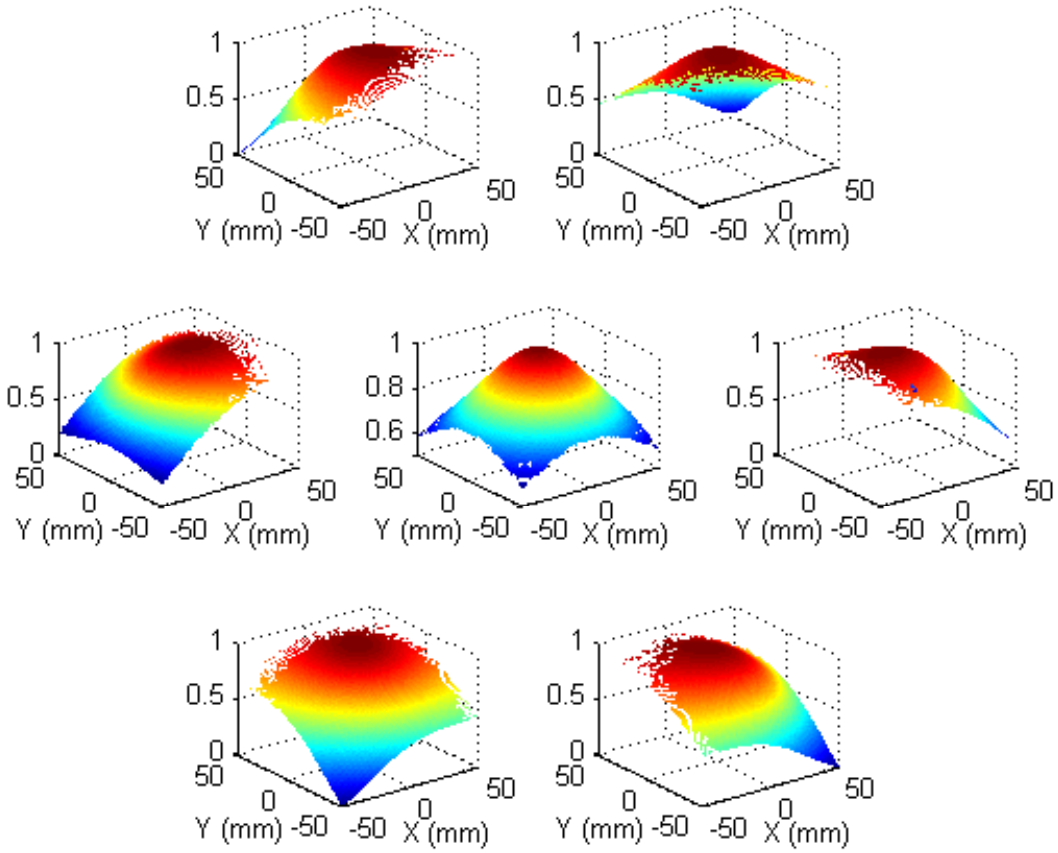

Figure 4.7: Visualizing focal points (x-y plane) and their corresponding intensities (z-axis) underneath each lens. (Graphs are positioned according to lens numbering and arrangement.) x-y plane is a 50 mm x 50 mm receiver plane underneath lens array with (0,0) centered underneath and 40 mm below the middle lens.

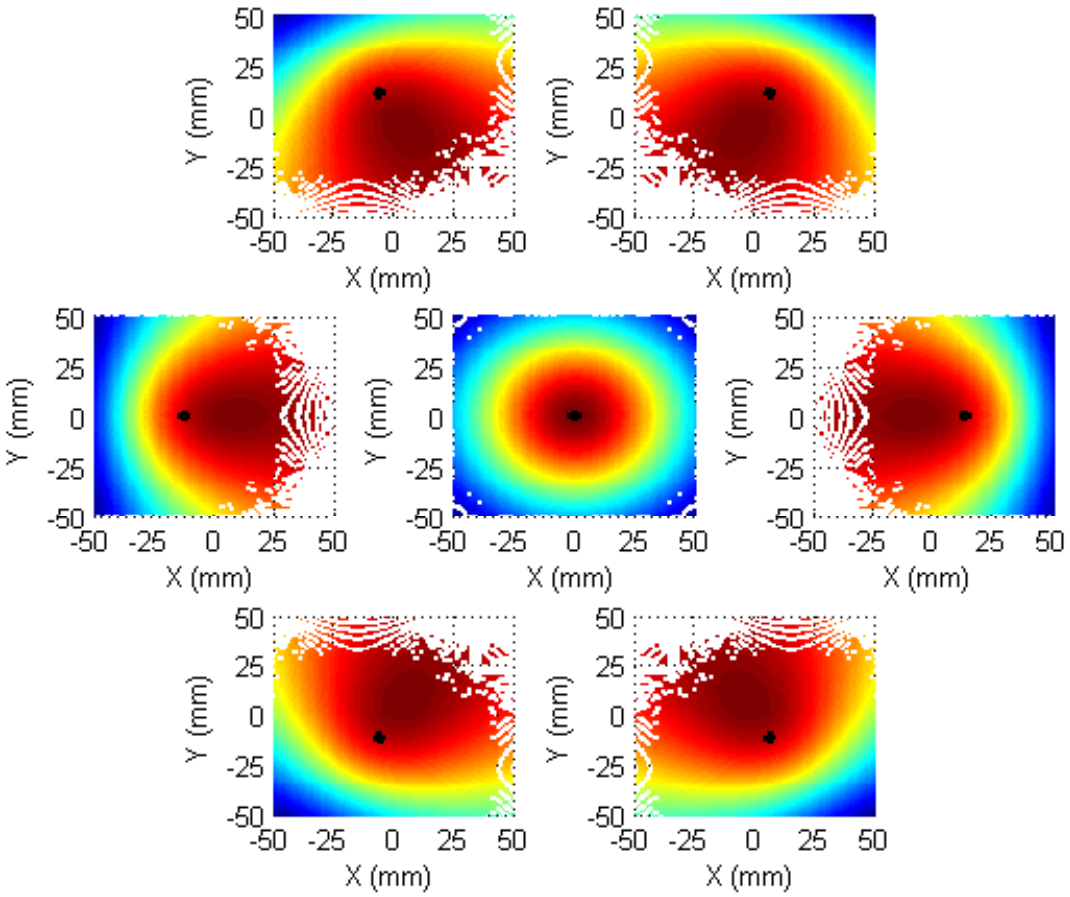

Figure 4.8: Top-view of visualizing focal points (x-y plane) and their corresponding intensities underneath each lens. (Graphs are positioned according to lens numbering and arrangement.) x-y plane is a 50 mm x 50 mm receiver plane underneath lens array with (0,0) centered underneath and 40 mm below the middle lens. Overlaid on each plot is the position of the target photodiode corresponding to that lens.

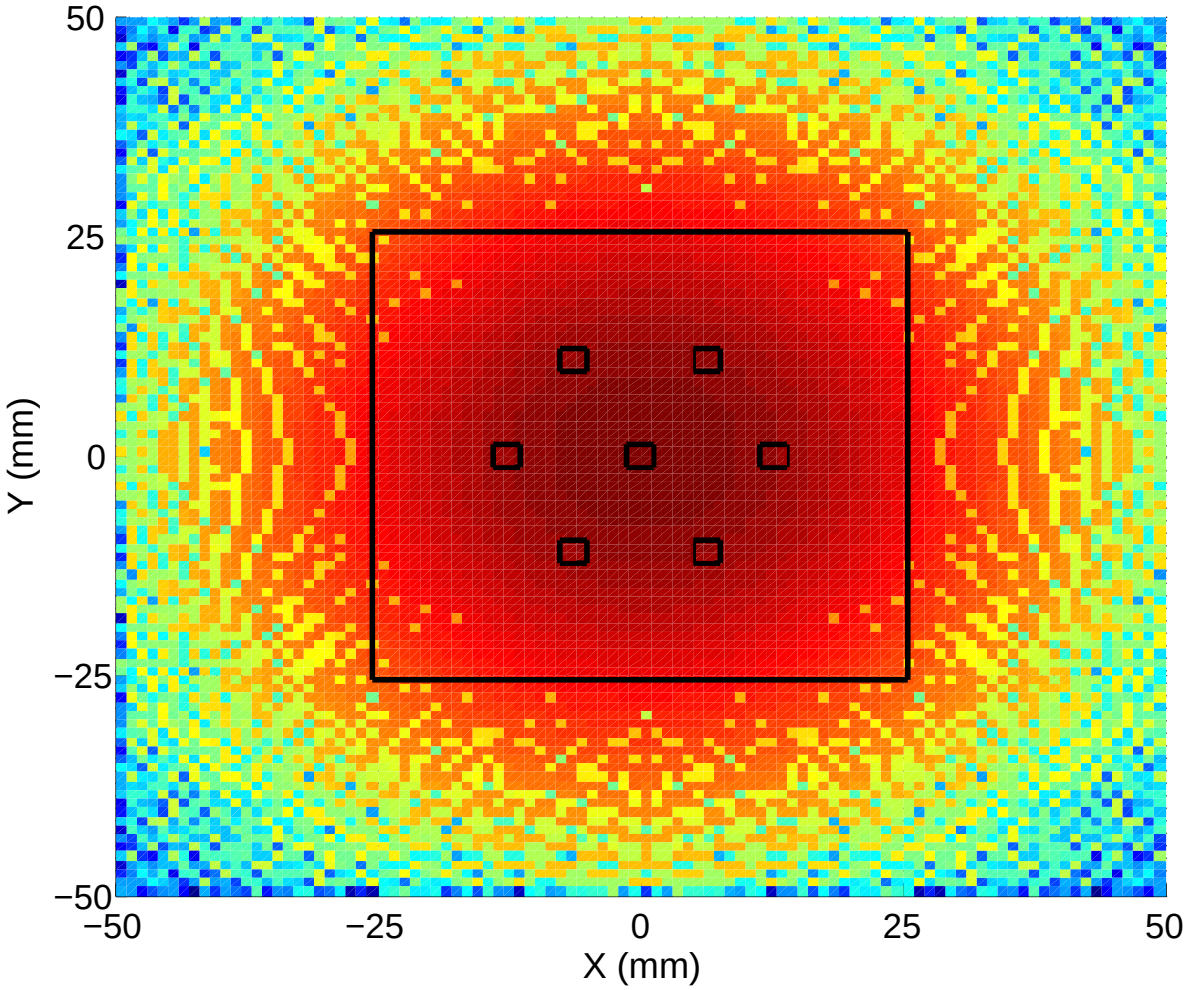

Figure 4.9: Top-view of visualizing combined receiver plane with summation of focal points (x-y plane) and their intensities. x-y plane is a 50 mm x 50 mm receiver plane underneath lens array with (0,0) centered underneath and 40 mm below the middle lens. Overlaid on the plot is the photodiode array placement. The goal of this plot is to suggest and validate positioning of photodiodes to maximize light collected while also maximizing separation between photodiodes. In this simulation light is incident on the lens-photodiode array from *all* angles. Note, in particular that the position and orientation of the lenses generates a superposition, that generates a wider area on the receiver plane, but without a noticeable local maxima for each lens.

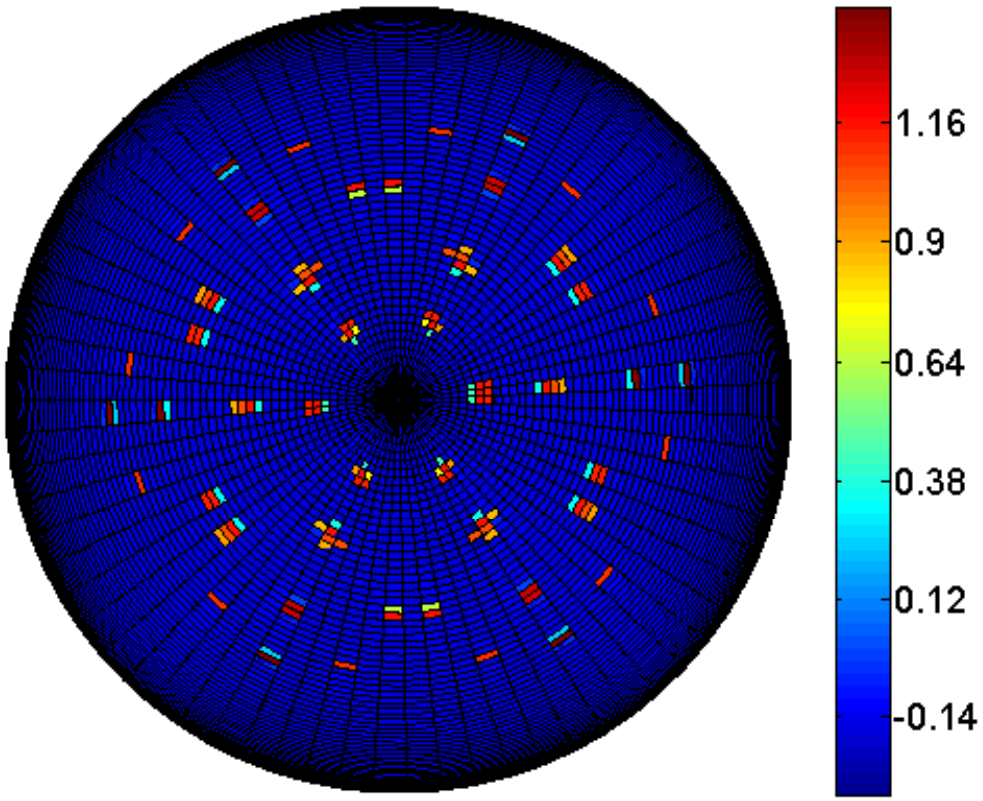

Figure 4.10: Top-view of spherical projection of solid angles subtended by each lens-photodiode pair field of view (FOV). Light enters through each of the 7 lenses and can fall on up to 7 photodiodes for a total of 49 lens-photodiode pair FOVs. Middle FOV is not visible due to overlapping of contour mapping. Units on this plot are normalized intensities.

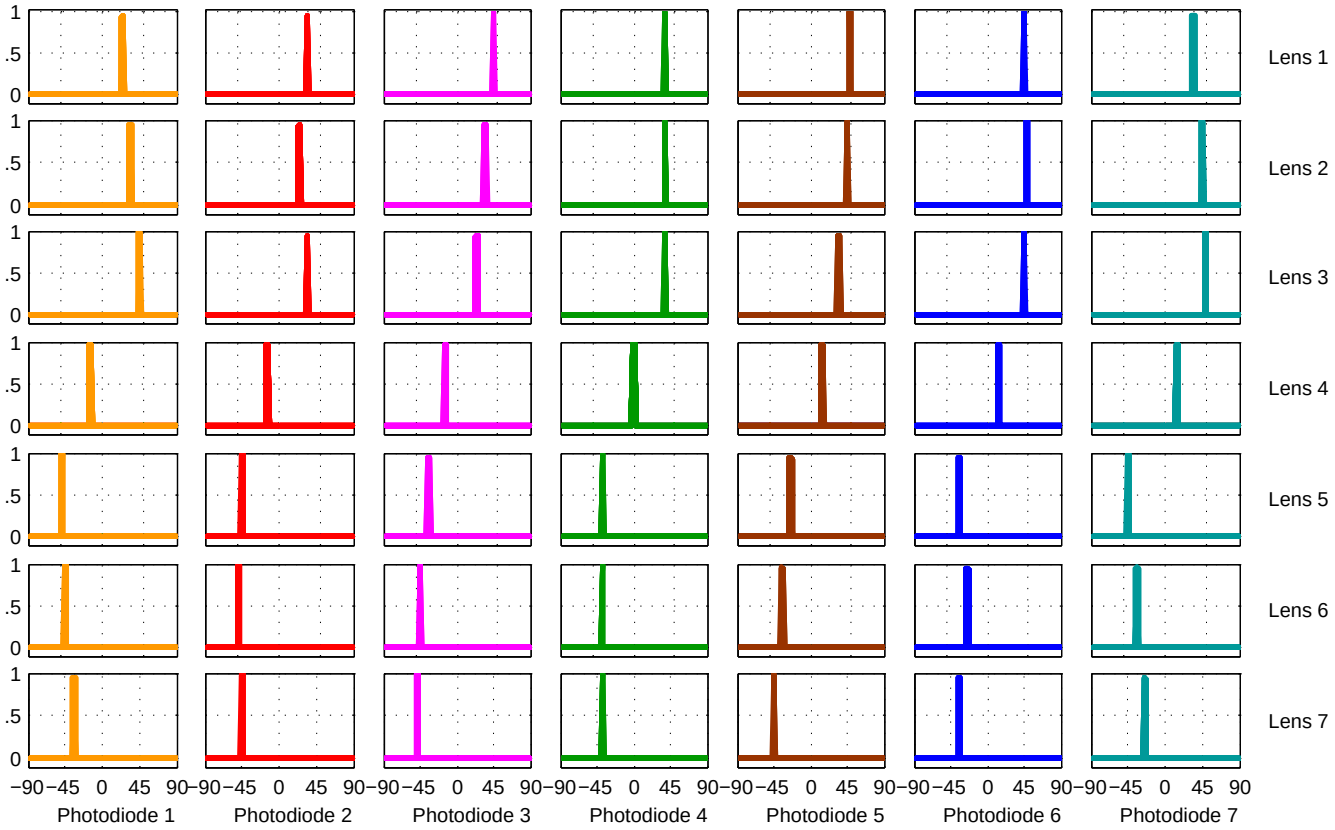

Figure 4.11: Field of view (FOV) plots for all 49 lens-photodiode pairs. Light enters through each of the 7 lenses and can fall on up to 7 photodiodes for a total of 49 lens-photodiode pair FOVs. Angles on x-axis span -90° to 90°. Angles -90° to 0° correspond to zenith angles $\theta \in [0, \pi/2]$ for all azimuthal angles $\phi \in [3\pi/2, \pi/2)$. Angles 0° to 90° correspond to zenith angles $\theta \in [0, \pi/2]$ for all azimuthal angles $\phi \in [\pi/2, 3\pi/2)$. Y-axis shows normalized intensities.

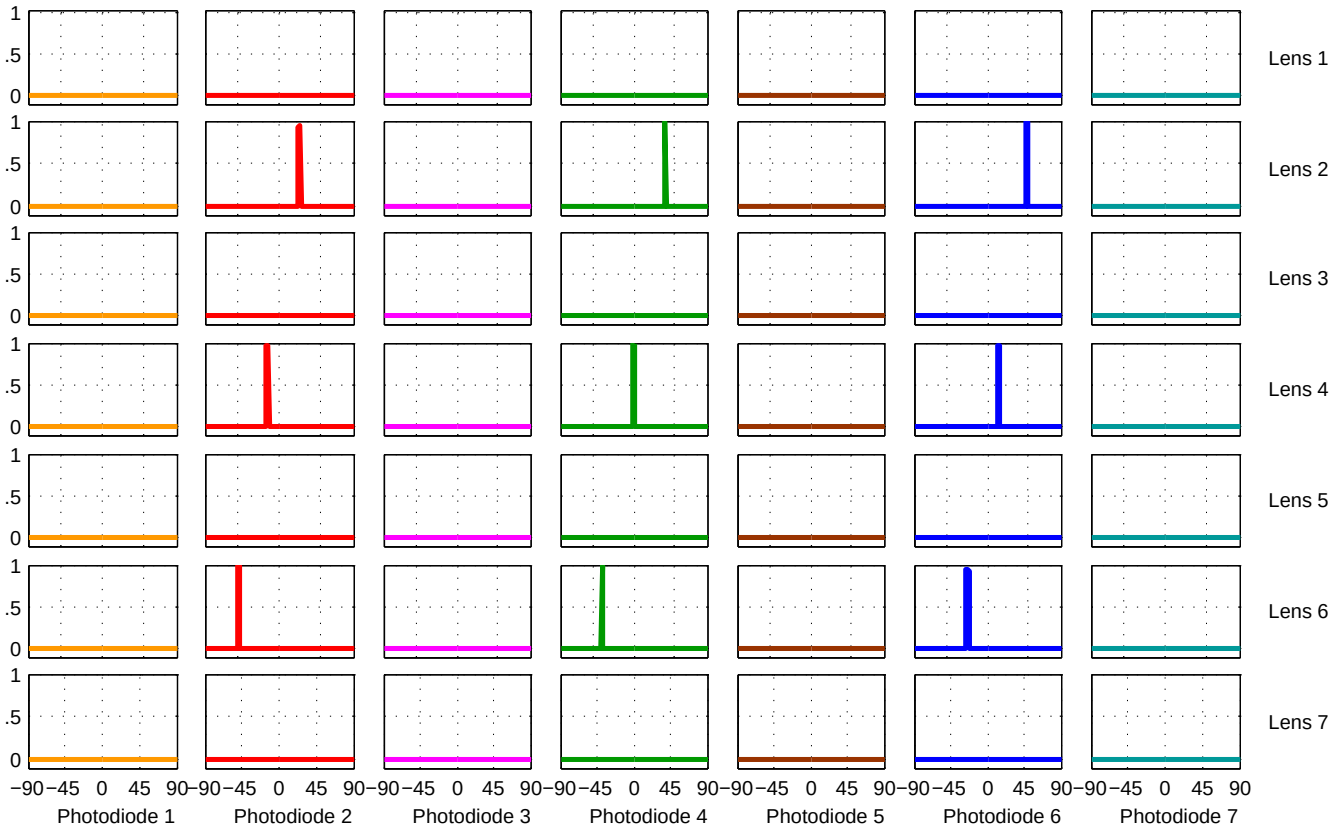

Figure 4.12: One-axis field of view (FOV) plots for all 49 lens-photodiode pairs. The chosen axis lies along the x-axis and runs through lenses (and photodiodes) 2, 4, and 6. Along this axis, light enters through each of the 3 lenses and can fall on up to 3 photodiodes. Angles on x-axis span -90° to 90°. Angles -90° to 0° correspond to zenith angles $\theta \in [0, \pi/2]$ for a fixed azimuthal angle $\phi = 0$. Angles 0° to 90° correspond to zenith angles $\theta \in [0, \pi/2]$ for a fixed azimuthal angle $\phi = \pi$. Y-axis shows normalized intensities.

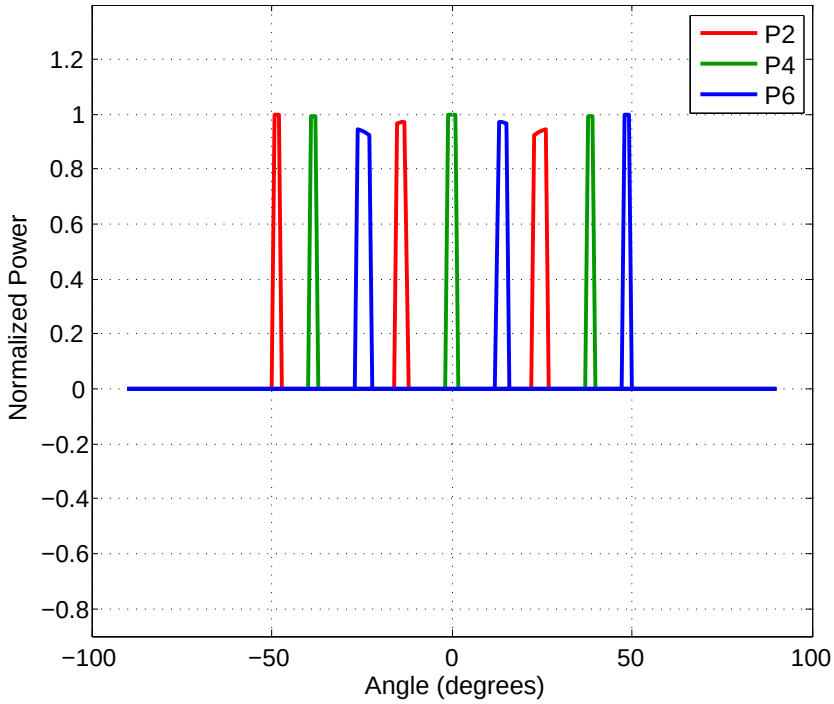

Figure 4.13: One-axis field of view (FOV) plots for 3 photodiodes along that axis. The chosen axis lies along the x-axis and runs through lenses (and photodiodes) 2, 4, and 6. Angles on x-axis span -90° to 90°. Angles -90° to 0° correspond to zenith angles $\theta \in [0, \pi/2]$ for a fixed azimuthal angle $\phi = 0$. Angles 0° to 90° correspond to zenith angles $\theta \in [0, \pi/2]$ for a fixed azimuthal angle $\phi = \pi$. This plot corresponds to the photodiode outputs for the scenario in Figure 4.12. Color codes for the photodiodes remain the same. Y-axis shows normalized intensities.

Chapter 5

Experiments and Applications of Smart Transmitters and Receivers

This chapter shows all of the in-air and in-water experiments of the 7-channel segmented transmitter and the 7-channel lens-photodiode array receiver. The experiments also serve as demonstration for some of the capabilities of the new smart front-end. The chapter is organized as follows, separated into the different experiments conducted:

1. Characterization of the Lens-photodiode Array
2. Angle of Arrival Estimation
3. Backscatter Estimation
4. Diversity Combining
5. Multi-user with CDMA and SDMA

5.1 Characterization of the Lens-photodiode Array

Experiments were first conducted to characterize the responsivity of the prototype receiver's lens-photodiode array as a function of the incident light, and in turn derive its FOV. Experiments were conducted for the receiver pointed in all directions in a 2π steradian and intensities were observed at all photodiode outputs stored as a function of the spherical co-ordinates (θ, ϕ) with $0 \leq \theta \leq \pi/2$ and $0 \leq \phi \leq 2\pi$. A pan and rotate system was constructed using digital servos and was used to point the array towards a constant, expanded, white light source. The seven amplified photodiode outputs were digitized using a simultaneous 8-channel digitizer. Four separate experiments were then conducted for four different lens-photodiode separations, 40, 50, 60, and 70 mm. The experimental setup and results are detailed in this section.

5.1.1 Experiment Description

The primary goal of this section is to understand the behavior of the prototype lens-photodiode array. The primary performance parameter that is to be characterized is the responsivity of the receiver as a function of the direction that light falls on it from. This in turn describes the field of view (FOV) of the device. This is an important metric since expanding FOV has been the primary design goal of this device.

The lens-photodiode array was previously modeled in MATLAB and simulation results were obtained. One of the limitations of the model is being unable to accurately predict the spread of the focal point into a conic section as the separation between the lens-array and the photodiode-array is increased or decreased. A thorough characterization of the lens-photodiode array will also help us understand how the FOV changes as a function of this separation distance.

The geometry used throughout this section is first described. The two-dimensional FOV is defined as the the responsivity of the device to all angles θ from -90 to 90 degrees as observed from the middle lens, 4. In this case, a single one-axis slice of the lens-photodiode array along the axis that lies along the photodiodes 2, 4, and 6 is used. It is to be noted that this is symmetric along the axis that lies along photodiodes 3, 4, and 7 as well as the axis that lies along the photodiodes 5, 4, and 1.

In the three dimensional case, the spherical co-ordinates are described by (θ, ϕ) as observed from the middle lens 4. In this case, theta ranges from 0 to 90 degrees, for all ϕ ranging from 0 to 360 degrees. The geometry is illustrated in the figure below. This range of theta and phi corresponds to a solid angle of 2π steradian.

For the purpose of characterization, a constant, expanded beam of light needs to be shined on the receiver from all points in this 2π steradian. It is easier to keep the light source fixed as the receiver is pointed in all (θ, ϕ) in the 2π steradian. To this end, a pointing mount is constructed to pan and rotate the lens-photodiode array.

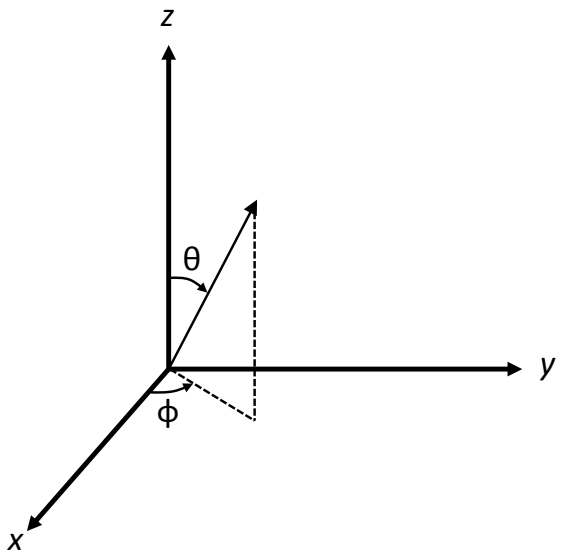

Figure 5.1: Geometry used for characterization.

5.1.2 Pan and Rotate System

The pan and rotate system holds and points the lens-photodiode array in all (θ, ϕ) for a total solid angle of 2π steradian. It is constructed using two digital servos. The first, base servo, acts as the pan servo and can pan θ' from -90 to 90 degrees. The next, plate servo, acts as the rotate servo and can rotate through ϕ' from 0 to 180 degrees. Together (θ', ϕ') corresponds to all (θ, ϕ).

Table 5.1: Mapping between pan and rotate ranges and characterization geometry ranges.

θ'	ϕ'	θ	ϕ
$[0, 90]$	$[-90, 89]$	$[0, 90]$	$90 \leq 180 \leq 269$
$[-90, 1]$	$[-90, 89]$	$[1, 90]$	$270 \leq 360 \leq 89$

Both servos used are of the same type and model, the AX-12A series from Dynamixel. This particular servo was chosen for its high angular resolution of 0.29° and high holding torque of 16.5 kg.cm at 12 V. The servos also have a high no load speed of 59 rpm (0.196s/60°) and a range of 300°. Additionally, each servo provides feedback for position, temperature, load, and voltage. These parameters allow the lens-photodiode array to be characterized with high resolution in a repeatable manner.

The servos are controlled by a PC running LabVIEW software that interfaces through a

serial port. The LabVIEW program points the lens-photodiode array in a pre-determined pattern where it sweeps through θ' from -90° to 90° in increments of 1°, while sweeping through ϕ' from 0° to 180°, for each θ', in increments of 1°.

The lens-photodiode array is mounted to the pan and rotate system and subsequently to a 12" x 12" optical breadboard using laser cut acrylic parts. Figure 5.2 shows a perspective side image of the pan and rotate system with the 7-channel receiver and lens-photodiode array mounted to the optical breadboard and positioned on an optical table. Figure 5.3 shows a front view of the same setup. In the image, the separation between lens-array and photodiode-array is at its maximum experimented position of 70 mm.

5.1.3 Experimental Setup

The experiment is setup on an optical table for maintaining alignment throughout the duration of an experiment and between multiple experiments. The 7 receiver outputs are digitized using a National Instruments (NI) 8-channel DAQ, model no. USB-6009, which has a maximum sampling rate of 250 kSps. Although the sampling rate is low for the digitizer to be used as a communications receiver, it is ideal for power measurements used in these characterization experiments.

The total number of data points captured is $91 * 360 = 32,760$. Although the pan and rotate allows to sweep at a rate of approximately 8 data points per second, the software is intentionally slowed to collect 4 data points per second, for a total test duration of approximately 2 hours and 15 minutes. The light source has been tested to stay constant for the duration of this test and the experiments are conducted in air, on an optical table, with no other light sources present.

An initial experiment is conducted without the lens array in front of the photodiodes. The purpose of this test is to characterize the FOV of the photodiode array alone. Four separate experiments are conducted after that, with the lens array over the photodiode array. For each of these four experiments, four different separations between the lens array and the photodiode array (receiver plane) are characterized, ranging from 40 mm to 70 mm in increments of approximately 10 mm each.

For all experiments, the output of each photodiode is separately amplified using a DC-coupled receiver. The seven outputs of the receiver front-end is digitized by an NI USB-6009 250 kSps digitizer. At each position, 100 data points are sampled at a sampling rate of 1 kSps and averaged and recorded for all seven outputs, along with the current θ' and ϕ'.

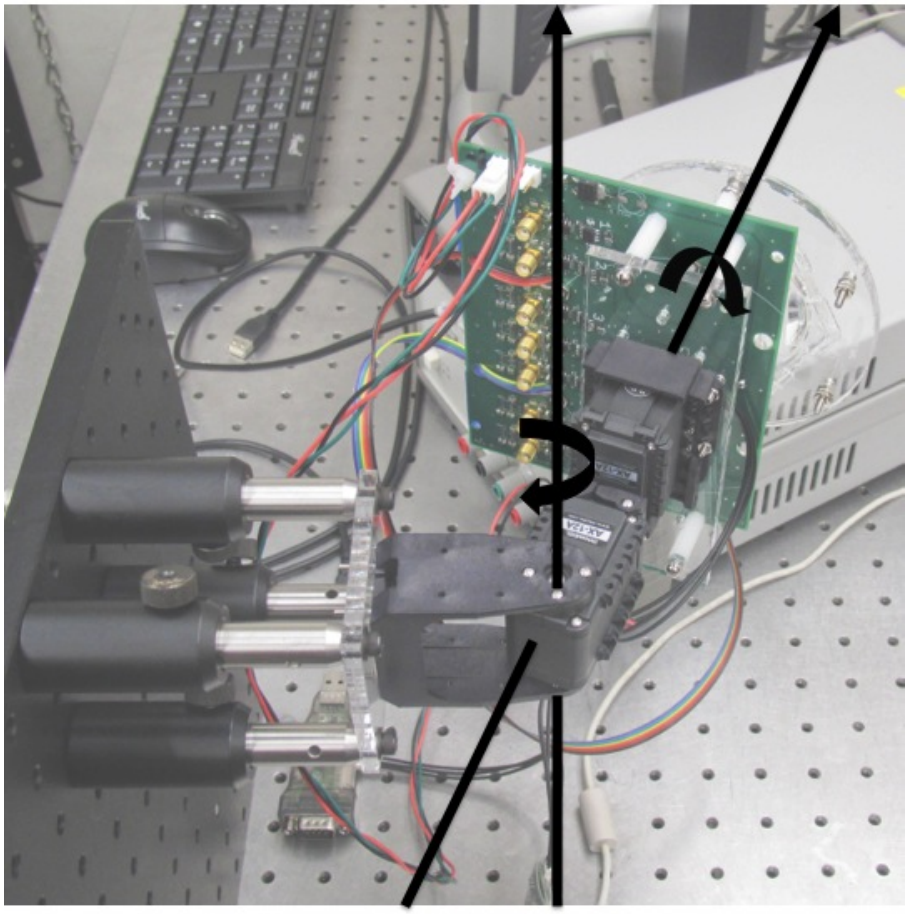

Figure 5.2: Perspective side view image of pan and rotate system with 7-channel receiver and lens-photodiode array mounted. Overlay shows axes of rotation.

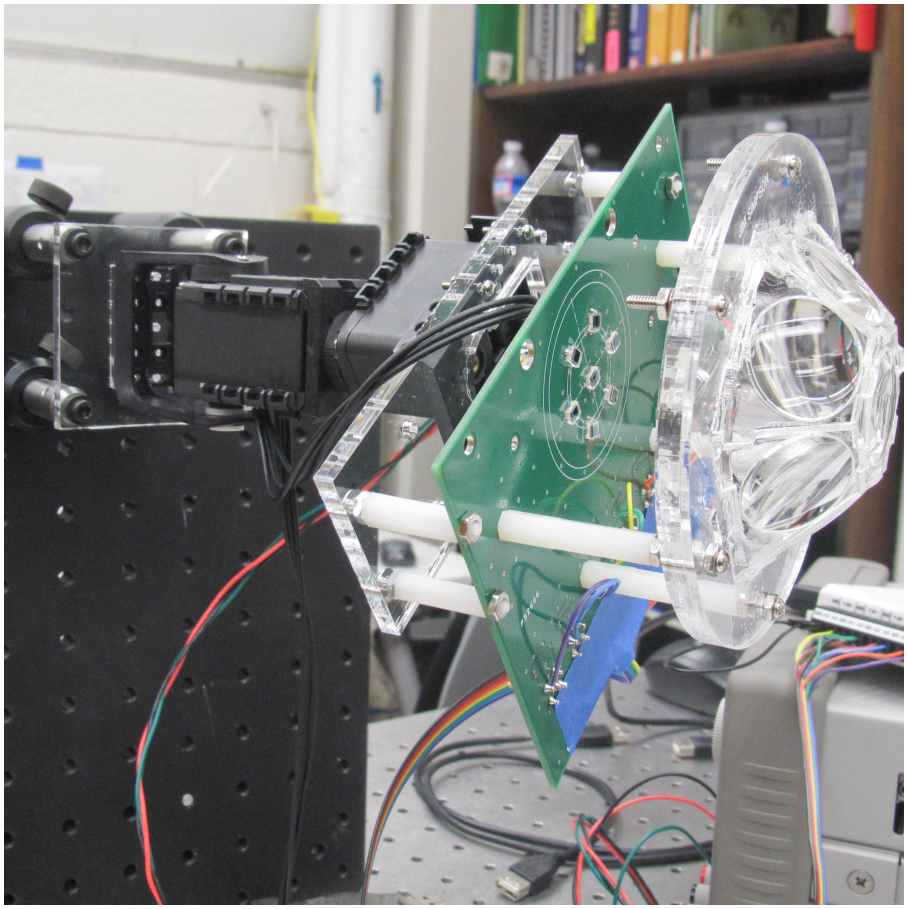

Figure 5.3: Front view of pan and rotate system with 7-channel receiver and lens-photodiode array mounted. Separation between lens-array and photodiode-array is at its maximum experimented position of 70 mm.

Figure 5.4: NI USB-6009 digitizer.

Table 5.2: List of characterization experiments.

Experiment Number	Lens-photodiode Separation
Exp_A0	No lens array
Exp_A1	40 mm
Exp_A2	50 mm
Exp_A3	60 mm
Exp_A4	70 mm

5.1.4 Experimental Results

The following plots outline the major results from the characterization of the lens-photodiode array receiver. Figures 5.5 through 5.8 show images of the spot sizes for each of the experiments A_1 through A_4. Figures 5.9 though 5.13 show the two-dimensional single-axis field of view (FOV) for each of the experiments A_0 through A_4. The combined FOV is also plotted in spherical co-ordinates. Figures 5.14 through 5.18 show the top-view of the three-dimensional FOV in spherical co-ordinates for each of the experiments A_0 through A_4. An analysis of the results are included after the plots in Section 5.1.5.

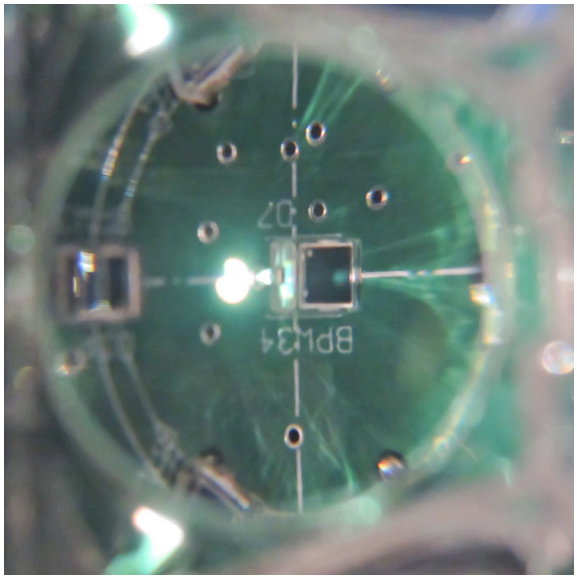

Figure 5.5: Image of exp_A1 spot size. Note that the spot size is chosen to be slightly less than the active area of each photodiode.

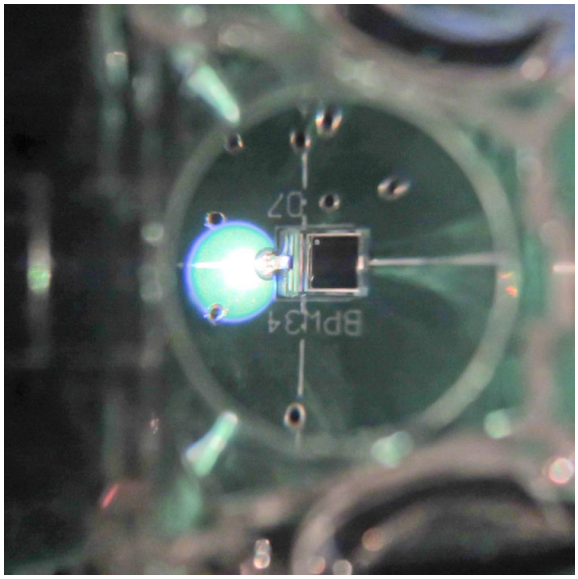

Figure 5.6: Image of exp_A2 spot size. Note that the spot size is chosen to be slightly more than the active area of each photodiode.

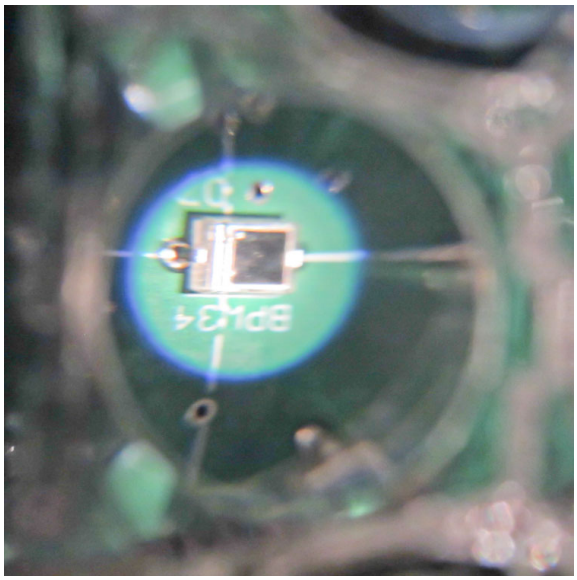

Figure 5.7: Image of exp_A3 spot size. Note that the spot size is chosen to be approximately the inside-to-inside gap of the photodiodes such that the spot enters the next photodiode as it leaves one.

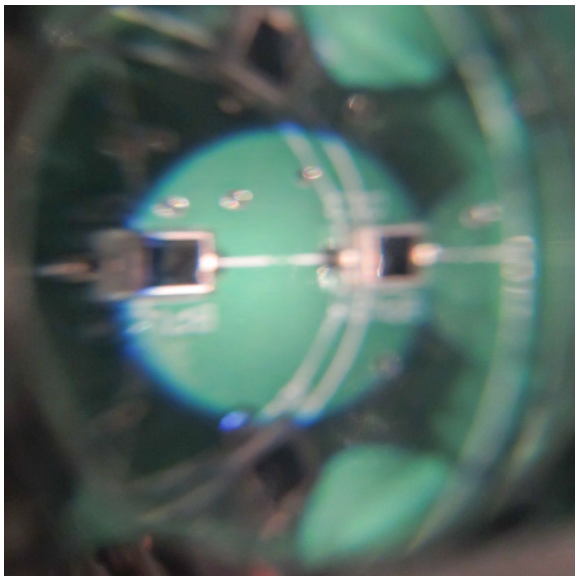

Figure 5.8: Image of exp_A4 spot size. Note that the spot size is chosen to be approximately the outside-to-outside gap of the photodiodes such that the spot always includes at least one photodiode.

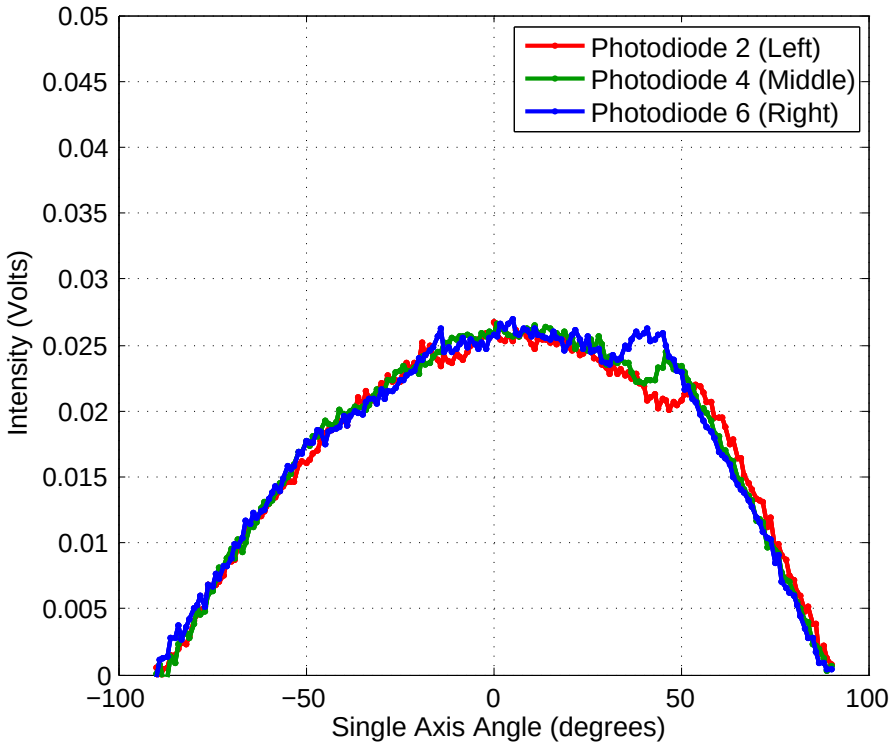

Figure 5.9: Two-dimensional single-axis FOV for Exp_A0: No lens array.

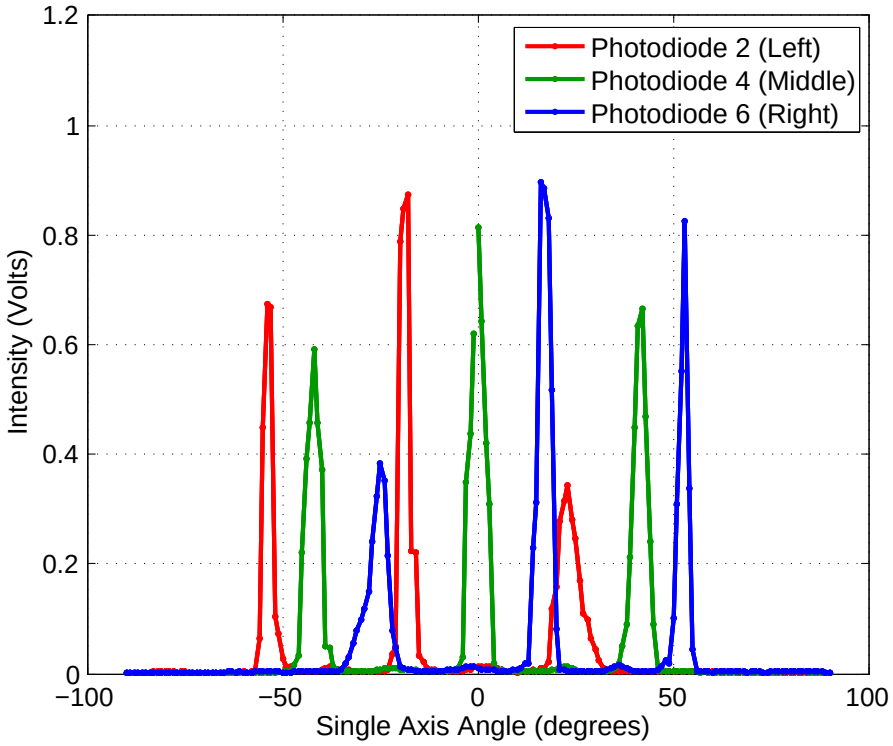

Figure 5.10: Two-dimensional single-axis FOV for Exp_A1: Lens-photodiode separation = 40 mm.

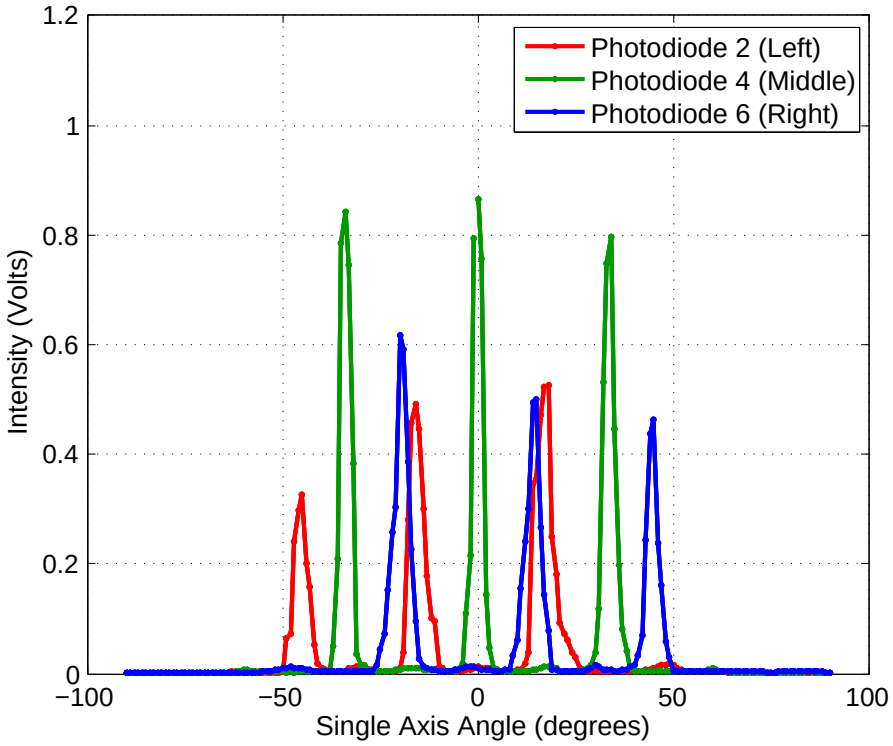

Figure 5.11: Two-dimensional single-axis FOV for Exp_A2: Lens-photodiode separation = 50 mm.

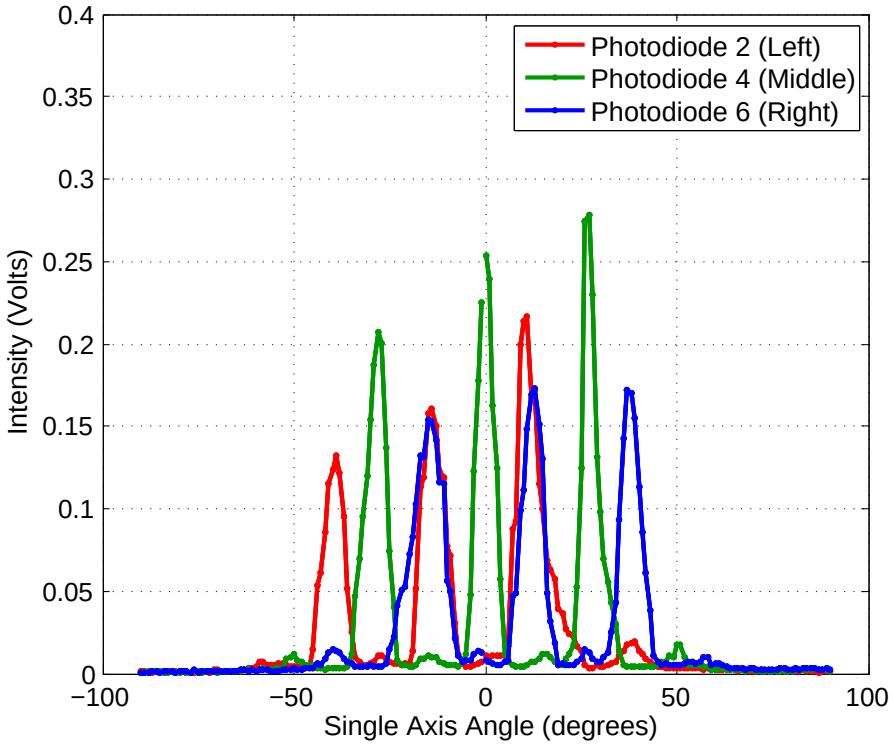

Figure 5.12: Two-dimensional single-axis FOV for Exp_A3: Lens-photodiode separation = 60 mm.

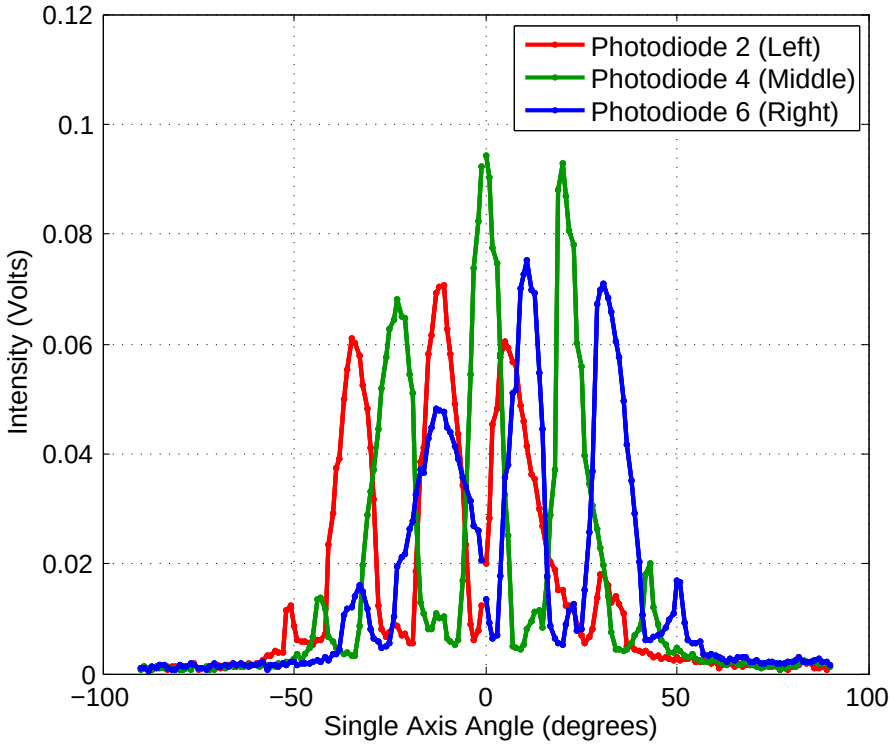

Figure 5.13: Two-dimensional single-axis FOV for Exp_A4: Lens-photodiode separation = 70 mm.

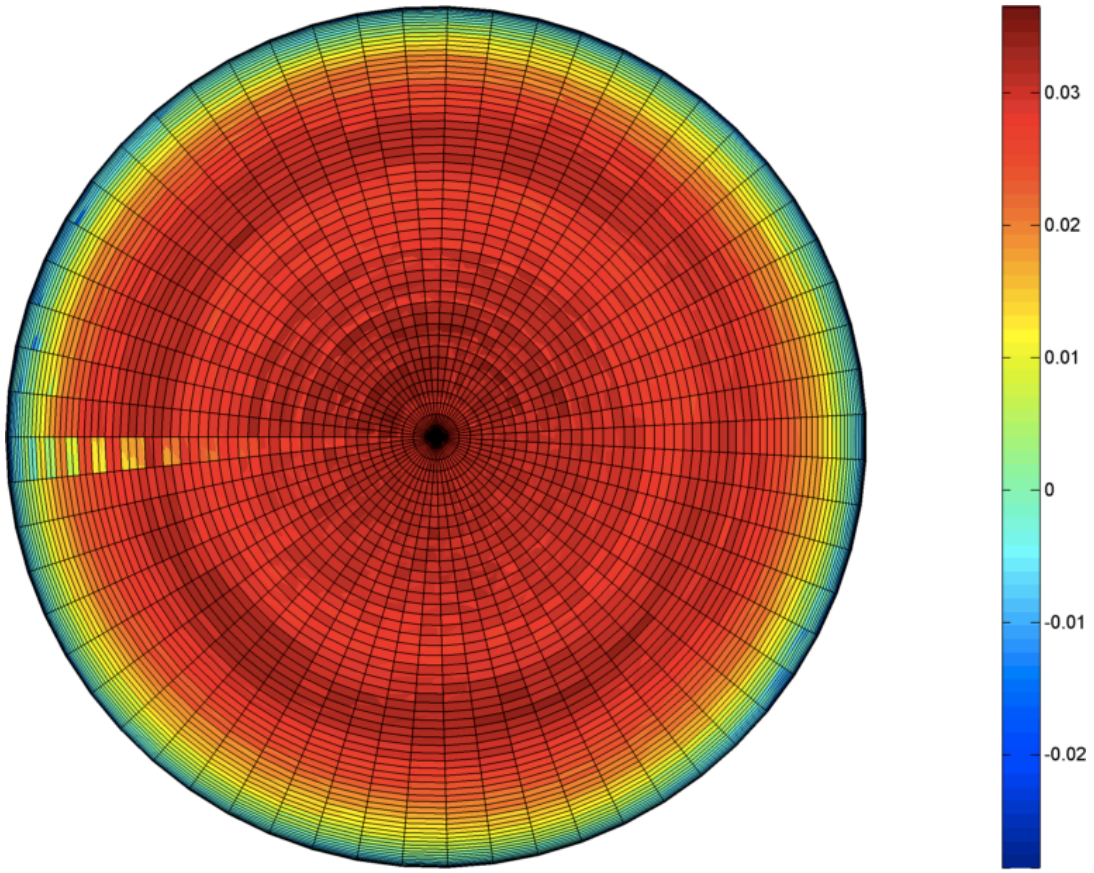

Figure 5.14: Top-view of three-dimensional FOV in spherical co-ordinates for Exp_A0: No lens array. $\theta = 0°$ lies at the center and increases outwardly till $\theta = 90°$ at the edge of the hemisphere. $\phi = 0°$ points south and increases clockwise. $\phi = 180°$ points north.

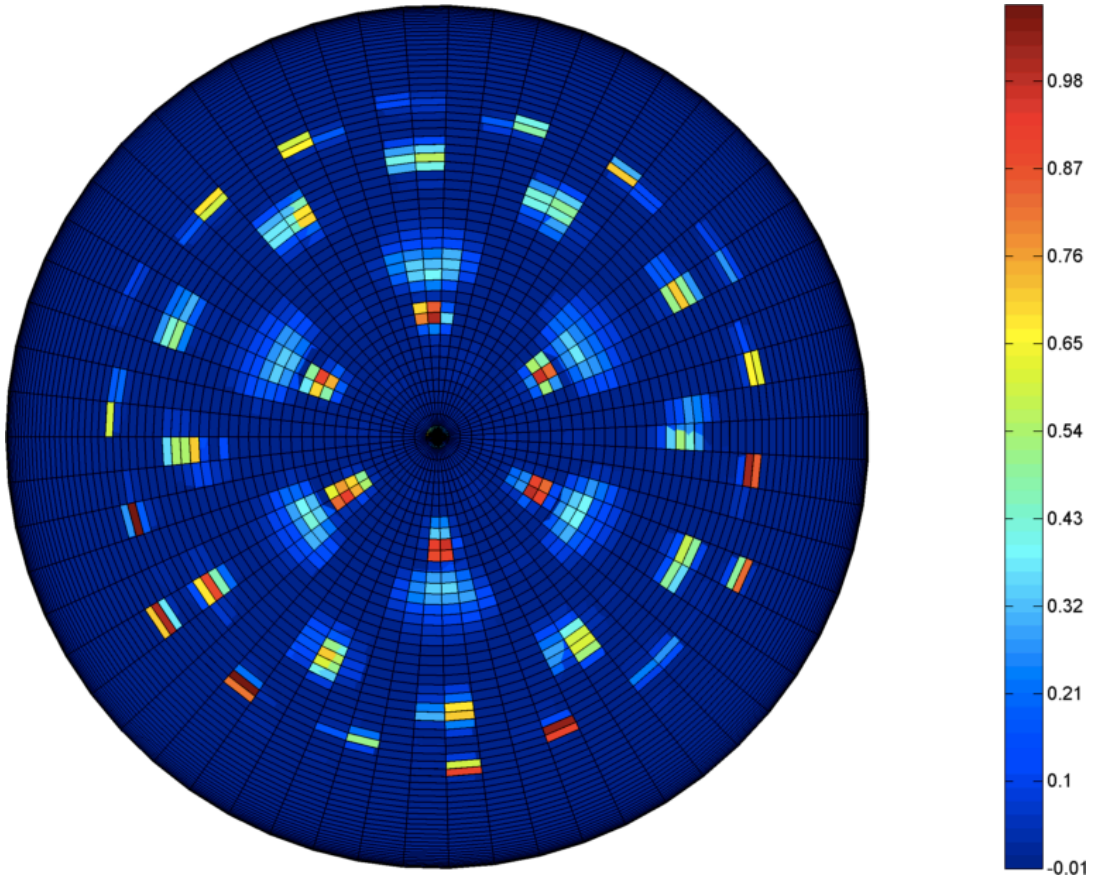

Figure 5.15: Top-view of three-dimensional FOV in spherical co-ordinates for Exp_A1: Lens-photodiode separation = 40 mm. $\theta = 0^\circ$ lies at the center and increases outwardly till $\theta = 90^\circ$ at the edge of the hemisphere. $\phi = 0^\circ$ points south and increases clockwise. $\phi = 180^\circ$ points north.

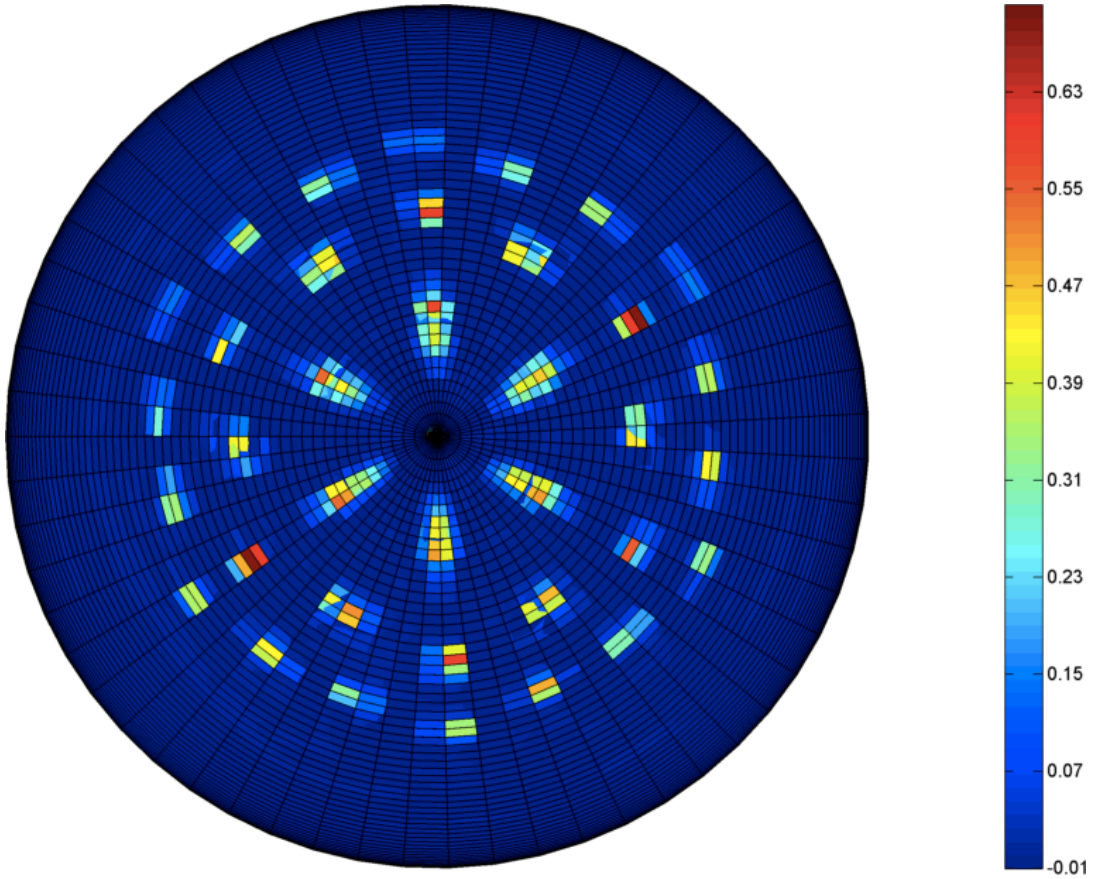

Figure 5.16: Top-view of three-dimensional FOV in spherical co-ordinates for Exp_A2: Lens-photodiode separation = 50 mm. $\theta = 0^\circ$ lies at the center and increases outwardly till $\theta = 90^\circ$ at the edge of the hemisphere. $\phi = 0^\circ$ points south and increases clockwise. $\phi = 180^\circ$ points north.

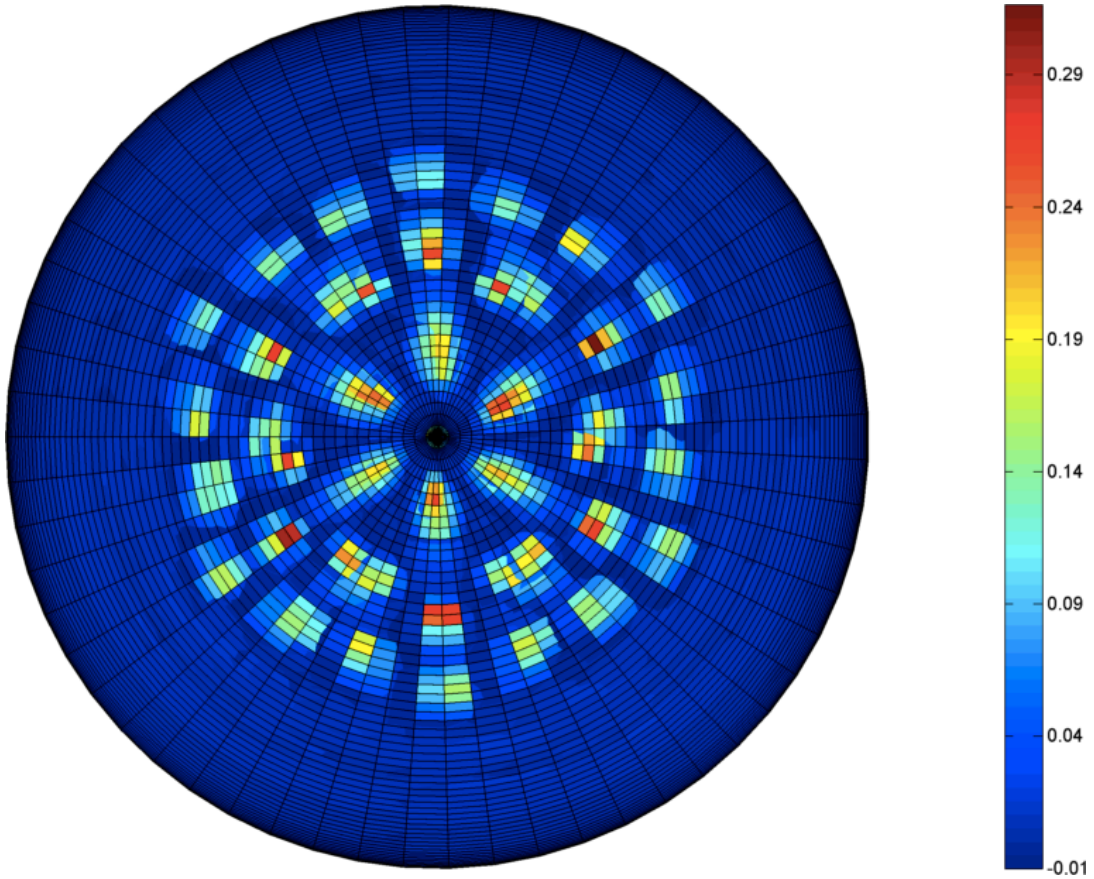

Figure 5.17: Top-view of three-dimensional FOV in spherical co-ordinates for Exp_A3: Lens-photodiode separation = 60 mm. $\theta = 0^\circ$ lies at the center and increases outwardly till $\theta = 90^\circ$ at the edge of the hemisphere. $\phi = 0^\circ$ points south and increases clockwise. $\phi = 180^\circ$ points north.

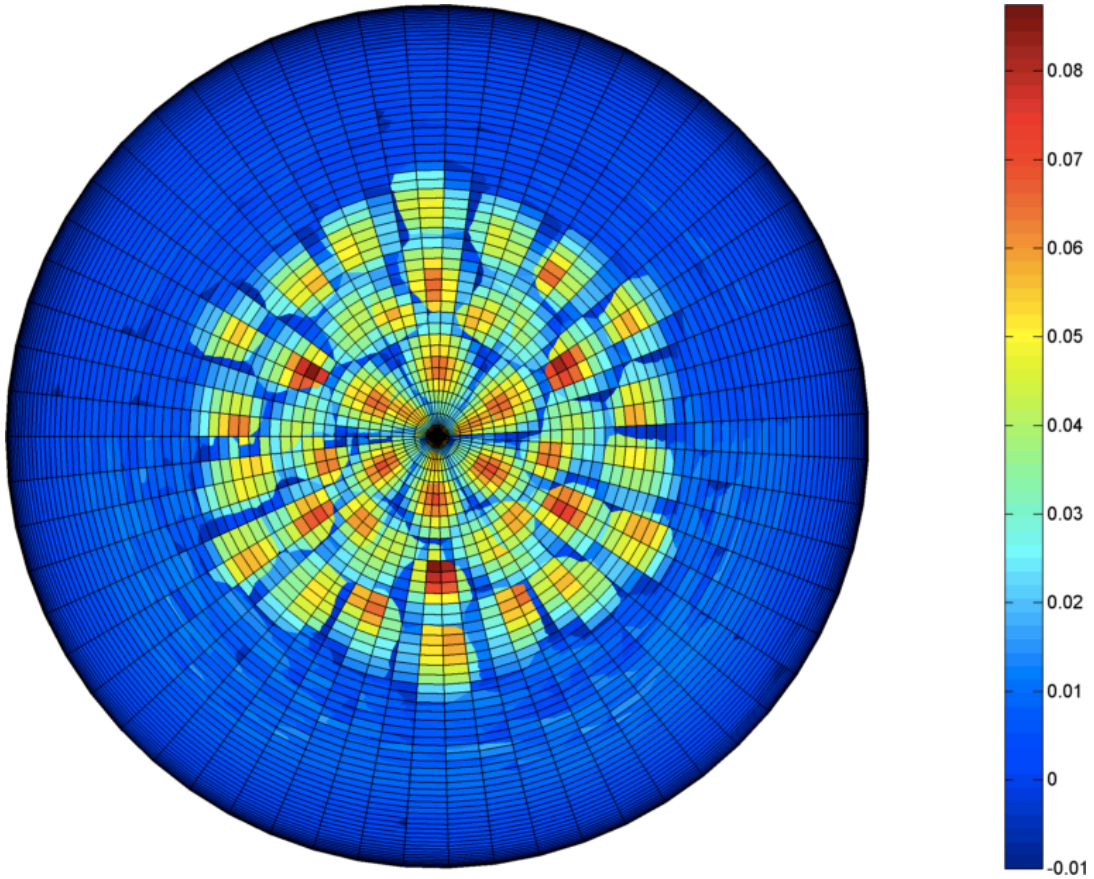

Figure 5.18: Top-view of three-dimensional FOV in spherical co-ordinates for Exp_A3: Lens-photodiode separation = 60 mm. $\theta = 0^\circ$ lies at the center and increases outwardly till $\theta = 90^\circ$ at the edge of the hemisphere. $\phi = 0^\circ$ points south and increases clockwise. $\phi = 180^\circ$ points north.

5.1.5 Characterization Analysis

The primary results obtained from the characterization experiments for the lens-photodiode array is the field of view (FOV) for the five experimental scenarios previously discussed. Each of these scenarios change the separation between the lens array and the photodiode array in increments of 10 mm. This separation determines the distance between the focal points of each lens and the position of the receiver plane. As this separation increases, the focal points de-focus into their projections on the receiver plane (photodiode array) that take shape as conic sections.

This process effectively widens the FOV of each individual lens-photodiode pair, the combination of which starts off as individual FOVs and then widens to overlap each other. Exp_A0 is a baseline experiment with no lens-array mounted. Exp_A1 has a separation that results in a spot size formed between the middle lens (lens 4) and the middle photodiode (photodiode 4) of approximately slightly less than the active area of the photodiode. Exp_A2 has a separation that results in a spot size of approximately slightly more than the active area of the photodiode. Exp_A3 has a separation that results in a spot size of approximately the inside-to-inside gap between the photodiodes such that the spot enters the next photodiode as it leaves one. Exp_A4 has a separation that results in a spot size of approximately the outside-to-outside gap between the photodiodes such that the spot always includes at least one photodiode. Figures 5.5 through 5.8 show images of the spot sizes for each of the experiments A_1 through A_4.

Since visualizing the resultant FOV in (θ, ϕ) is easier along one-axis of the lens-photdiode array, cross-sectional, two-dimensional, single-axis FOV plots are generated. Figures 5.9 though 5.13 show the two-dimensional single-axis field of view (FOV) for each of the experiments A_0 through A_4. The combined FOV is also plotted in spherical co-ordinates. Figures 5.14 through 5.18 show the top-view of the three-dimensional FOV in spherical co-ordinates for each of the experiments A_0 through A_4. The three-dimensional plots help visualize the segmented individual FOV in different directions, which illustrates the core feature of the lens-photodiode array. As the separation distance increases, notice each individual FOV widen, but at the expense of an overall decreased FOV.

The smaller separation distance of 40 mm gives the maximum total FOV at $\sim$120°, and the larger separation distance of 70 mm gives the least total FOV at $\sim$90°. However, the increased total FOV comes at the expense of larger gaps between the individual FOVs. By the same mechanism, smaller gaps between the individual FOVs and more overlap between the individual FOVs is achieved at the expense of decreased total FOV.

The difference in total power at the receiver between each of these scenarios is also analyzed. This illustrates the trade-off between increased FOV overlap and decreased total power.

5.2 Angle of Arrival Estimation

Angle of arrival estimation involves estimating the direction of arrival of the incident light based on the relative output powers observed at each photodiode. The preliminary algorithm explored here uses the uniqueness of the relationship between the photodiode outputs to potentially extract the angle of arrival.

The approach taken is based on a look-up table traversal generated using characterization data previously collected. Effectively, the seven receiver outputs at each instant are sorted and compared against all possible receiver output patterns. The angle corresponding to the best match is chosen as the estimated angle. The best match is defined as, and obtained by, the look-up table location that is the closest match for the channel with the most power, followed by the next most power and so on. The experimental setup, ad hoc algorithm, and results are detailed in this section below.

5.2.1 Experiment Description

The angle of arrival estimation allows the 7-channel lens-photodiode array based receiver to predict the direction of incident light on the lens array using the receiver outputs. Although the focus of the segmented wide field of view receiver design is to increase the field of view without increase in noise, the uniqueness of the receiver outputs to the direction of incident light allows one to potentially extract the angle of arrival. In essence, the characterization of the receiver in the previous section allows one to visualize this property.

The approach taken to estimate angle of arrival is based on a look-up table traversal generated using characterization data previously collected. Effectively, the seven receiver outputs at each instant is compared against a table of angle of arrivals and their corresponding output patterns. The actual implementation of this algorithm is explained in detail below.

1. At each digitizer sampling instance, we define each of the photodiode output channels to have power:
$$\mathbf{P} = [P_1, P_2, \cdots P_7] \tag{5.1}$$

2. where the indices represent the corresponding photodiode index number and is stored as:
$$\mathbf{I} = [1, 2, \cdots 7] \tag{5.2}$$

3. The first step in the algorithm is to sort the photodiode outputs based on their power.
$$\mathbf{P}, \mathbf{sorted} = [P_n, min \leq \cdots \leq P_n, max] \tag{5.3}$$

4. and the corresponding new ordering of indices is stored in $\mathbf{I}, \mathbf{sorted}$.

5. This sorted order of index numbers is converted to a decimal number and stored in $r_{\mathbf{I},\mathbf{sorted}}$ as:

$$r_{\mathbf{I},\mathbf{sorted}} = \sum_{i=1}^{7} \left(\mathbf{I}, \mathbf{sorted}(i)) * 10^{7-i}\right) \tag{5.4}$$

6. Previously, an array of all possible permutations of seven items has been generated and each of those orders converted to a decimal representation number in a similar fashion and stored in the array $\mathbf{C}$.

7. We then find the best match, as previously described, as the location n, such that:

$$\min_{n} |\mathbf{C}(n) - r_{\mathbf{I},\mathbf{sorted}}| \tag{5.5}$$

8. The angle is then extracted from the look up table as:

$$\hat{\theta} = \mathrm{LUT}(n) \tag{5.6}$$

The look-up table was previously generated using characterization data, where the angle of arrival is known, to assign an angle to each of the valid permutation orders. Note:

- The permutation of 7 items such that order matters and without repetition is $7! = 5040$ and correspondingly the size of the array $\mathbf{C}$ containing is 5040. This is also the maximum size of the LUT.

- The single-axis angle estimated in degrees belongs to the range $[-90, 90]$ and has 181 elements with angular resolution of 1°.

- As expected, the order of sorted photodiode indexes are non-unique, in which instance multiple possible angles are mapped to the same order. However, measured characterization data reveals this scenario to be less common.

- When such as event is observed in use, currently, the algorithm uses the first assigned angle to that order. It is possible to assign confidence levels to estimates in the future and improve the estimator performance.

- The performance of the estimator can also be increased by considering previous photodiode outputs or estimator outputs in addition to the current instantaneous output.

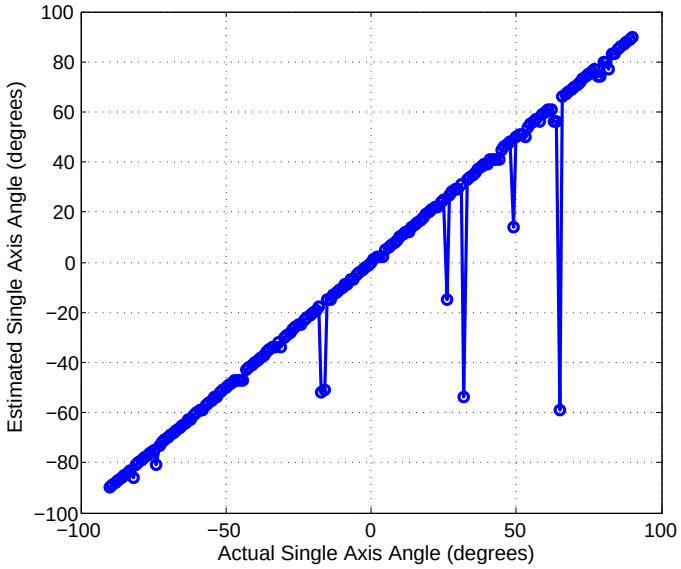

Figure 5.19: Estimates (y-axis) vs. actual (x-axis) angle of arrival for Exp_A1: Lens-photodiode separation = 40 mm using look-up table (LUT) algorithm. See plot below for error metrics.

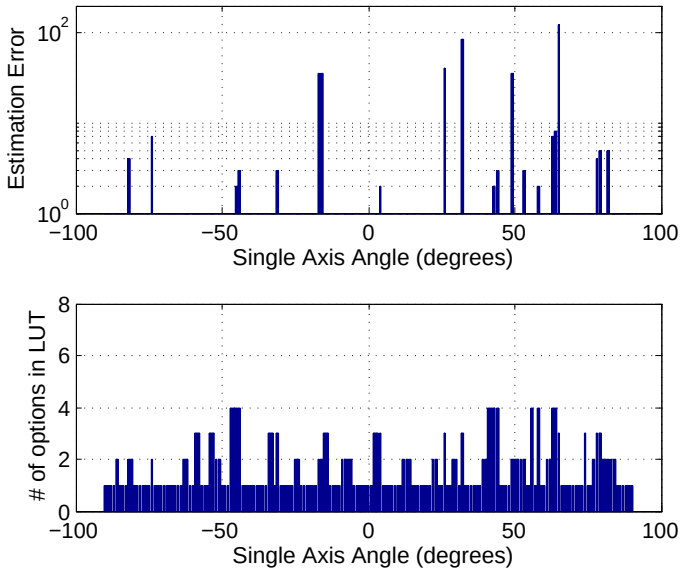

Figure 5.20: Absolute estimate error (top plot) and number of options in LUT, both as a function of actual angle of arrival for Exp_A1: Lens-photodiode separation = 40 mm.

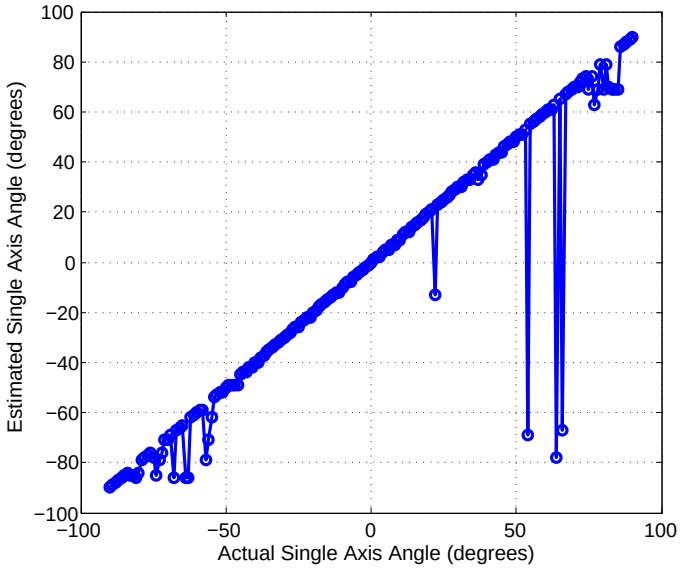

Figure 5.21: Estimates (y-axis) vs. actual (x-axis) angle of arrival for Exp_A2: Lens-photodiode separation = 50 mm using look-up table (LUT) algorithm. See plot below for error metrics.

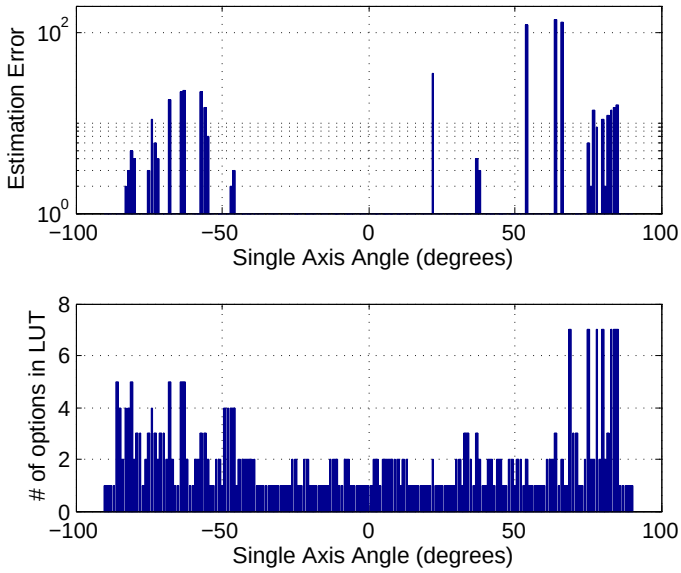

Figure 5.22: Absolute estimate error (top plot) and number of options in LUT, both as a function of actual angle of arrival for Exp_A2: Lens-photodiode separation = 50 mm.

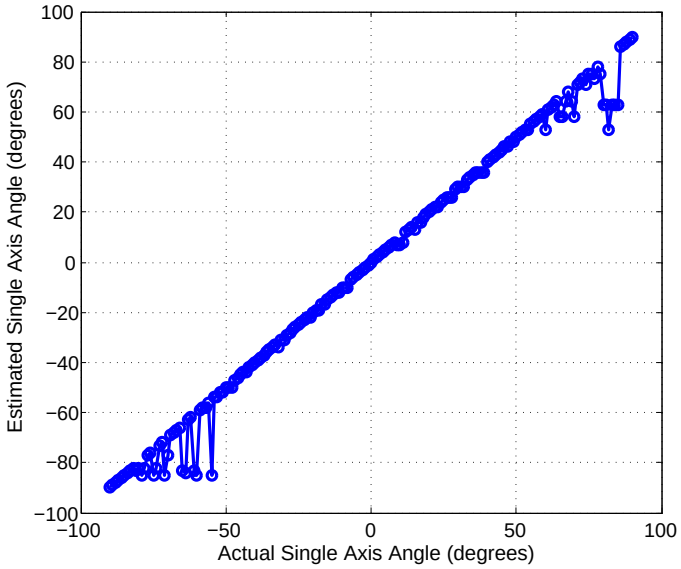

Figure 5.23: Estimates (y-axis) vs. actual (x-axis) angle of arrival for Exp_A3: Lens-photodiode separation = 60 mm using look-up table (LUT) algorithm. See plot below for error metrics.

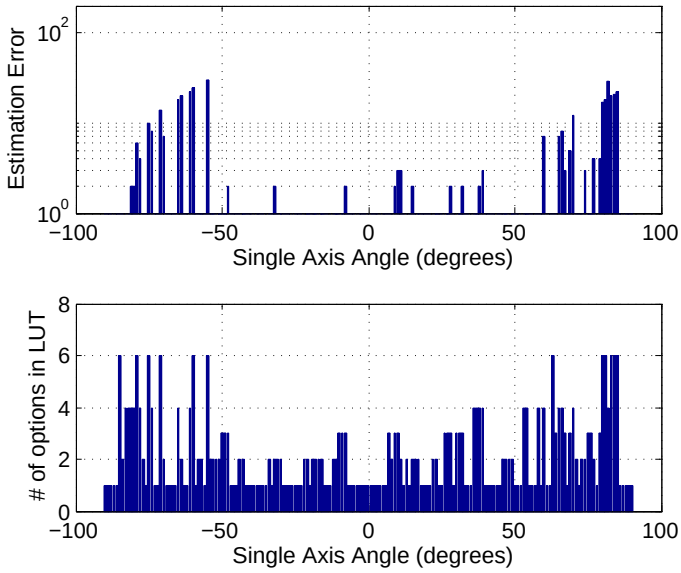

Figure 5.24: Absolute estimate error (top plot) and number of options in LUT, both as a function of actual angle of arrival for Exp_A3: Lens-photodiode separation = 60 mm.

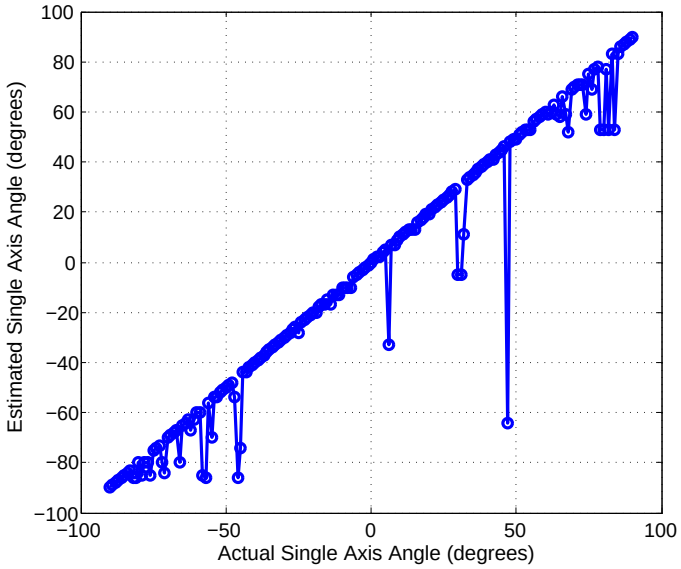

Figure 5.25: Estimates (y-axis) vs. actual (x-axis) angle of arrival for Exp_A4: Lens-photodiode separation = 70 mm using look-up table (LUT) algorithm. See plot below for error metrics.

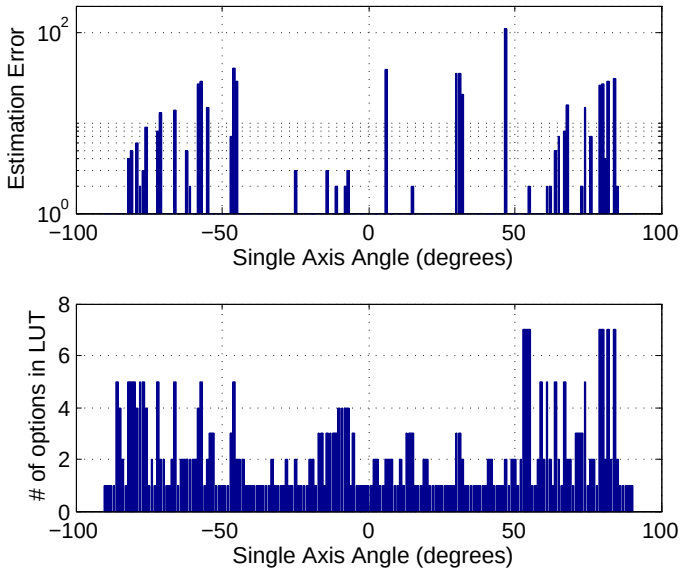

Figure 5.26: Absolute estimate error (top plot) and number of options in LUT, both as a function of actual angle of arrival for Exp_A4: Lens-photodiode separation = 70 mm.

5.2.2 Experimental Results

Look-up tables have been generated for each of the different lens-photodiode separation distances characterized previously. As as baseline performance metric, the algorithm is applied to the same data and it's performance and errors metrics generated.

Figures 5.19 through 5.25 shown the estimator performance in each of those experimental scenarios. The plots contain estimated angles vs. the known actual angles. Errors show as deviations from the ideal linear curve.

Figures 5.20 through 5.26 show the magnitude of the error and is plotted alongside the number of angles possible for each angle.

While the design allows for a LUT based algorithm to be used in estimating the single-axis angle of arrival with reasonable accuracy, estimating the three-dimensional spherical angle (θ, ϕ) is more complicated. One possible solution is to use an algorithm similar to Markov localization. Such an estimator would incorporate prior and posterior probabilities for the estimate, including a convolution between the measurements. Such a convolution can be intentionally introduced by rotating the receiver by a known ϕ'' between measurements. The convolution can also arise from movement of the platform the receiver is mounted to. This method is not further studied and is beyond this scope of this dissertation.

5.3 Backscatter Estimation

A smart transmitter can perform estimation of the water quality by using its backscattered return light and a co-located receiver to estimate the attenuation coefficient (channel state) of the channel at the transmitter. This technique has the advantage of knowing the water quality without relying on a back-channel for back-telemetry or even a separate instrumentation sensor. Knowing this information allows the transmitter to, for example, adaptively change its transmit power, data rate, code rate, or other parameters. The challenge to this technique is that the return beam from backscatter, depending on the attenuation coefficient of the channel, can be as low as approximately six orders of magnitude below the output power of the transmitter. To some extent, this can be solved by a few methods including, but not limited to: sending a higher power training sequence for the purpose of increasing the amount of backscattered light used for estimation, the receiver correlating the captured light to the actual data being transmitted, or even temporarily increasing the receiver gain. Techniques such as the use of a lock-in amplifier can also be used and are aided by the fact that the transmitter and the backscatter-receiver are co-located.

5.3.1 Experimental Setup

The experimental setup for backscatter estimation involves the use of a single transceiver: a transmitter and its co-located receiver. The receiver is placed approximately 8 inches beside the transmitter. Both the transmitter and its co-located backscatter-receiver are placed at the same side of the water tank. Another challenge in this experiment is in preventing any light, directly or through reflections, from the transmitter beam, from entering the receiver. This is prevented by the placement of baffles in such a way as to block any such beams. Additionally, a baseline experiment is conducted before filling the water tank to identify and characterize any such light. Also, since the transmitter and the receiver is fixed during the duration of the experiment, it is assumed for any such light to stay constant during the entire test.

Initially, a well characterized commercial-off-the-shelf transmitter and packaged Si-amplified-photodetector is used to conduct the experiment. This allows for an absolute value of the return beam to be first collected and understood. Additionally, the receiver being packaged, has the added benefit of being placed very close to and coupled through an o-ring to the window of the water tank in order to avoid any stray light from outside the water tank to enter the detector. The particular receiver used, being self-contained with the amplifier in a single shielded can, is capable of operating at up to a gain of 70 dB with a noise (RMS) of less than 740 μV and a corresponding noise equivalent power of $2.1{*}10^{-12}$ W/$\sqrt{\text{Hz}}$ at its peak responsive wavelength. The transmitter has a wavelength of 460 nm and operated at an output power of 350 mW.

During the experimentation, a transmissometer is also placed in the water tank to collect

Figure 5.27: Prototype system experimental setup outside water tank window for backscatter estimation. Picture taken before experiment with clear water in tank. Room lights are on for photographing setup.

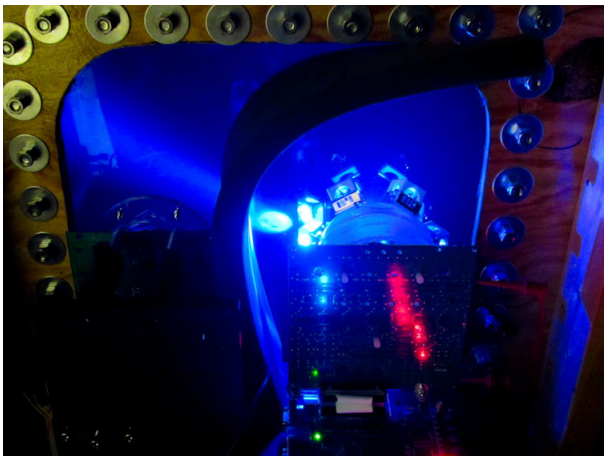

Figure 5.28: Prototype system experimental setup outside water tank window for backscatter estimation. Picture taken before experiment with clear water in tank. Some room lights are on for photographing setup.

the actual measurement of attenuation coefficient of the channel at each data point collected during the progression of the experiment. The experiment starts in clear water. The output power from the receiver is collected as the attenuation coefficient of the channel is increased. Attenuation coefficient is increased with the addition of Maalox, a commercial antacid. Clear municipal water has an attenuation coefficient of $\sim$0.5 m^{-1}. Maalox is added in increments of $\sim$25 ml and data collected at each increment. A sump pump in the water tank mixes the added Maalox to a homogeneous state. The experiment continues till $\sim$350 ml of Maalox at which point the attenuation coefficient reaches a value of $\sim$10 m^{-1}.

Experiments were then conducted using the prototype 7-channel transmitter and 7-channel receiver. The gain of the prototype receiver is significantly lower than that of the PDA100A. Hence the range of light collected is much lower.

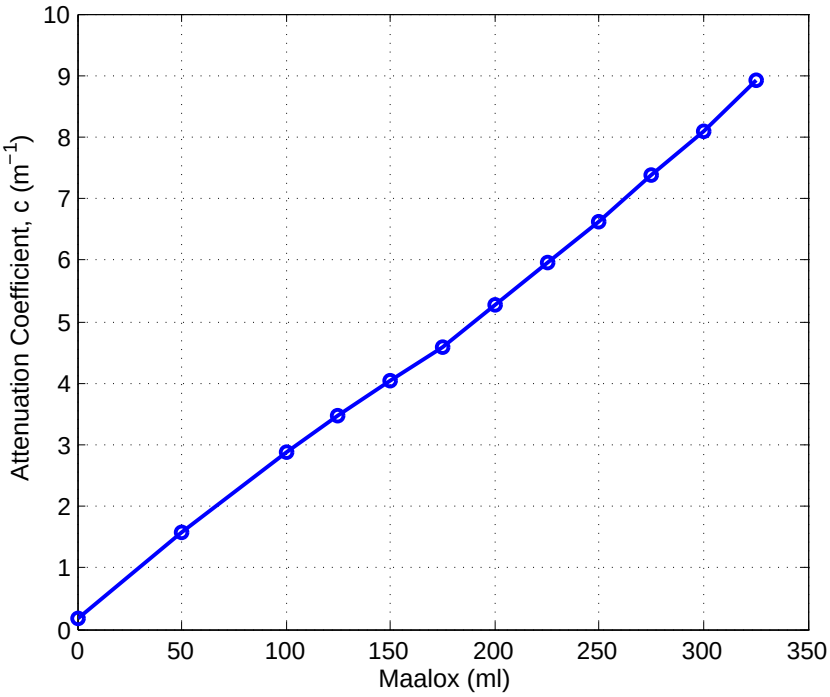

Figure 5.29: Measured attenuation coefficient using the transmissometer as Maalox was added in increments of 25 ml for Exp_B1.

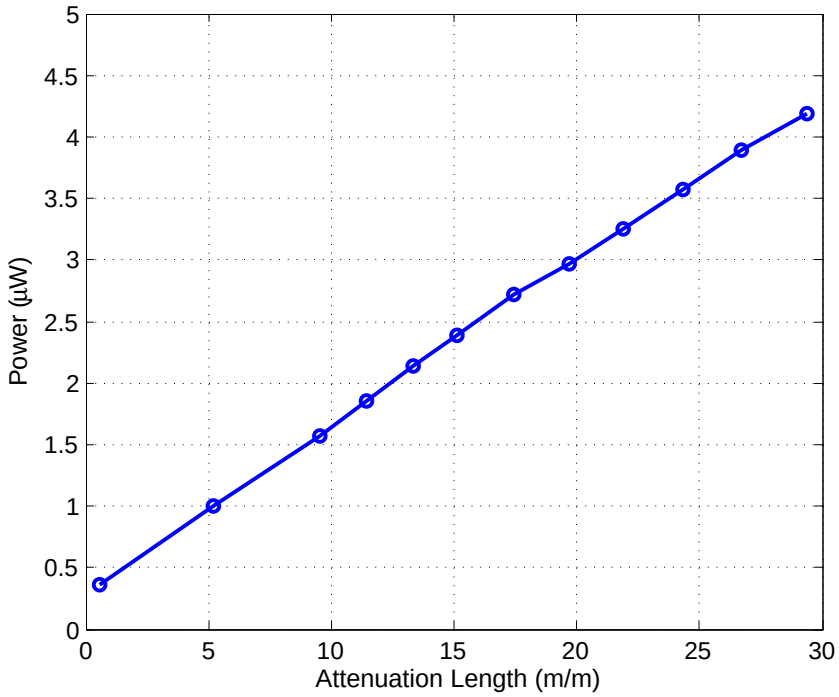

Figure 5.30: Backscatter optical power observed by the commercial-off-the-shelf (COTS) receiver for Exp_B1 plotted as a function of attenuation length calculated from transmissometer measurements. The use of the COTS receiver allows to measure an absolute value of the return light collected.

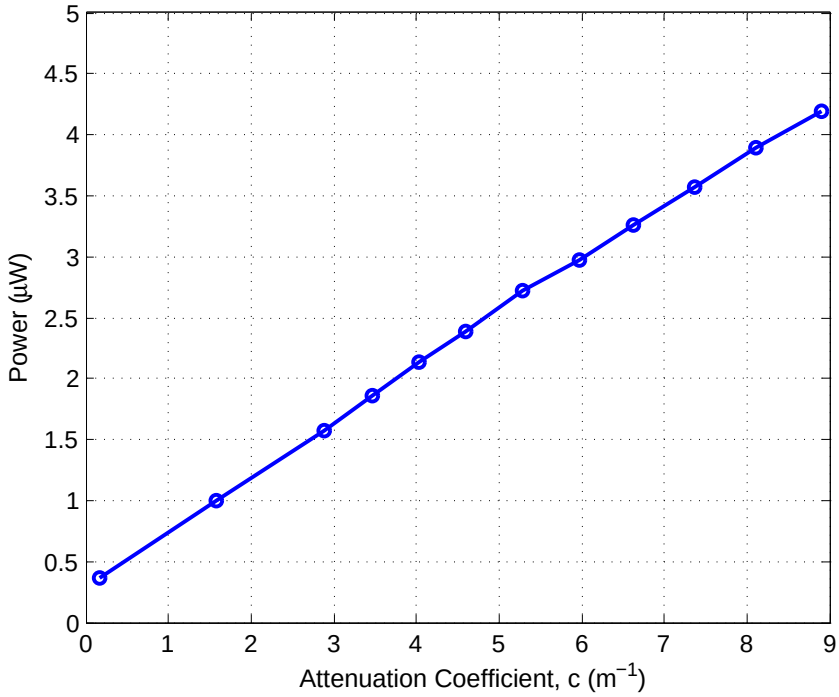

Figure 5.31: Backscatter optical power observed by the commercial-off-the-shelf (COTS) receiver for Exp_B1 plotted as a function of attenuation coefficient measured from transmissometer. The use of the COTS receiver allows to measure an absolute value of the return light collected.

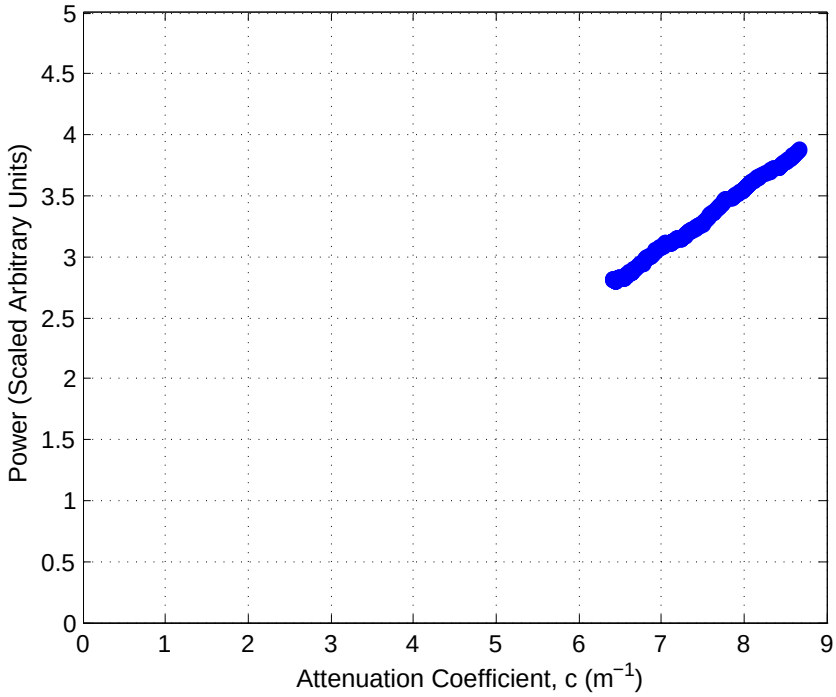

Figure 5.32: Backscatter optical power observed by the prototype 7-channel transmitter and receiver for Exp_B2 plotted as a function of attenuation coefficient measured from transmissometer.

5.3.2 Experimental Results

Figures 5.29 through 5.31 plots the results for Exp_B1, which used the commercial-off-the-shelf (COTS) hardware and Figure 5.32 plots the results collected using the prototype 7-channel transmitter and receiver.

For both experiments, Figure 5.29 plots the relationship between the measured attenuation coefficient using the transmissometer as Maalox was added in increments of 25 ml in order to validate the known linear relationship between the two. For Exp_B1, the measured backscatter power is plotted as a function of the transmissometer-measured true attenuation coefficient in Figure 5.31 and as a function of the corresponding attenuation length in Figure 5.30. The comparable plot of measured backscatter power as a function of the transmissometer-measured true attenuation coefficient for Exp_B2 is shown in Figure 5.32. This plot does not provide an absolute value for the measured backscatter. However, the x-axis limits are maintained between the two plots for comparison.

The results provide a measure of the integral of the full range of backscattering angles. However, no attempt is made to extract an actual backscattering coefficient from these measurements. Such measurements are technically difficult [75]. Exact measurements, although required for an instrumentation device, are not necessary for some schemes of adaptive communication. An instrumentation device would also have a small or no separation of distance between the light source and the detector. However, the relationship to attenuation coefficient is linear and, after calibration, can be used to set the output power of the transmitter in order to compensate for water conditions.

5.4 Diversity Combining

Diversity combining is the process of combining the multiple outputs from the receiver front-end in order to provide a single improved signal for processing. The two types of combining techniques investigated here are equal gain combining (EGC) and selection combining (SEL). In a typical communications system over a fading channel, the multiple receivers typically observe copies of the same signal with time-varying power levels. However, in the case of this particular receiver front-end introduced in this paper, the receiver front-end is analogous to an angular diversity system. As such, it is not always desirable to sum all receiver outputs together with equal gain as one would with EGC.

5.4.1 Experimental Setup

For the purposes of quantifying the detrimental effects of EGC, an experiment was conducted using a single 7-channel transmitter and a single 7-channel receiver, both of which were stationary during the duration of the experiment. First, the receiver channel pointed towards the transmitter was considered. From that point, other receiver channels, not oriented towards the transmitter, were added incrementally, until all seven channels were considered.

5.4.2 Processing

The digitized signals from the receiver output is saved on a computer for offline processing. The received signals are processed in MATLAB. The steps involved in processing are described below. One of the limitations of the experiment was the 2-channel digitizer. In the absence of a digitizer capable of digitizing all 7 outputs of the receiver prototype, at a fast enough sampling rate, the symmetric property of the assembly is taken advantage of. The output form the middle channel and one of the side channels are digitized. In software, the remaining 5 side channels are either assigned to an active channel or an inactive channel. Active or inactive is based on whether a transmitter was pointed towards that channel or not. The steps taken in processing the collected data is as below. The blind SNR estimation algorithm used operates on the downsampled output of a matched filter.

1. Diversity combining: Based on the inputs, the desired method is used to combine the different receiver outputs in to a single signal for the rest of the receiver to process.

2. Matched Filter: The received signal is correlated with a pulse shape matched to the rectangular pulses at the transmitter used in on-off-keying. The output of the matched filter is normalized by the energy of the pulse shape.

3. Downsample: The output of the matched filter is downsampled at the optimal point.

4. Normalization: The matched filter output is normalized by removing any DC bias.

5. SNR Estimation: The second and fourth moments of the normalized matched filter output is used to obtain an SNR estimate.

6. Hard Detector: Additionally, the soft detection bits are hard limited to obtain the received bits.

7. BER Calculator: The received bits are compared against a copy of the transmitted bits to obtain a BER for reference.

The primary result used from the processing is the SNR estimate. A main limitation of this method is the range of values for which the SNR estimator is accurate. The blind SNR estimator used saturates below 10 dB. Hence another approach to compare the results is added as well. Here as take the power spectral density (PSD) of the signal to observe the noise floor. Eye-diagrams were also used in understanding the effect on an OOK modulated data.

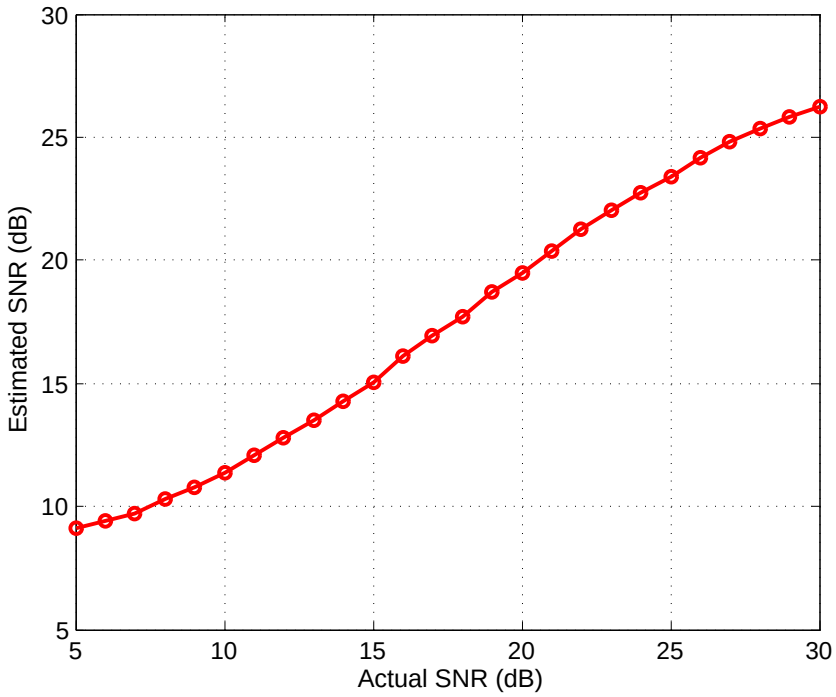

Figure 5.33: Estimate (y-axis) vs. actual (x-axis) SNR plotted to show estimator performance.

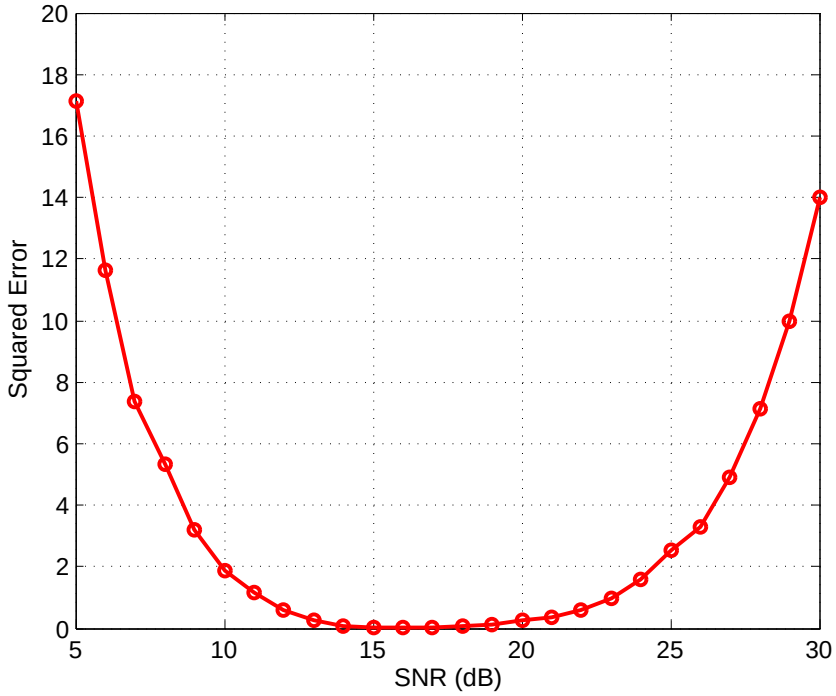

Figure 5.34: Squared error of SNR estimator to show range of reliable estimates.

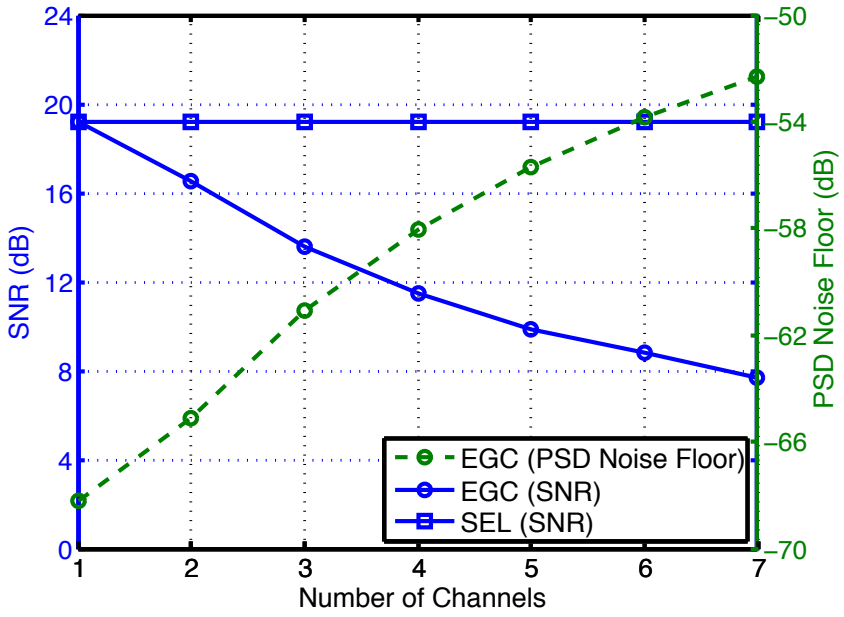

Figure 5.35: SNR and noise floor of the power spectral density (PSD), for equal gain combining (EGC) and selection combining (SEL), as the number of channels are added incrementally. Only one receiver is pointed towards and actively receiving data from the transmitter in this experimental scenario.

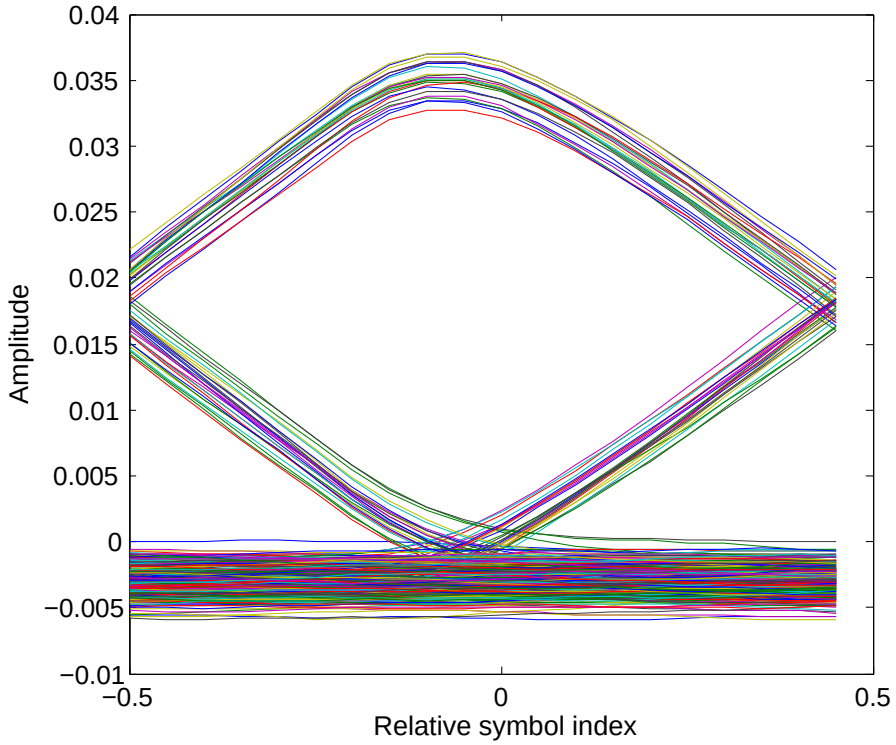

Figure 5.36: Eye diagram of received signal in high SNR (>20 dB). The prime code used for CDMA spreading does not have any 1 to 0 or 0 to 1 transitions.

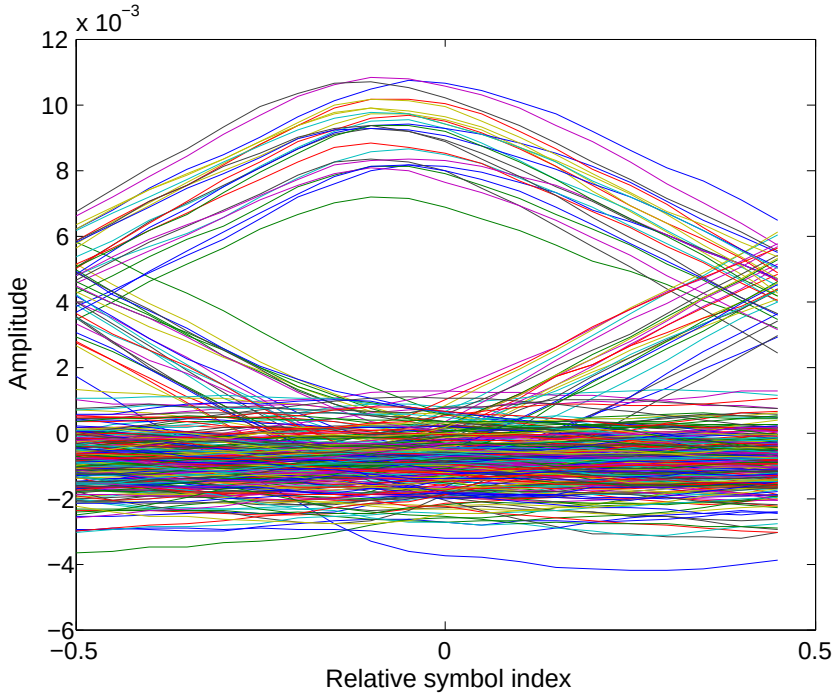

Figure 5.37: Eye diagram of received signal when EGC is used and no. of channels = 1.

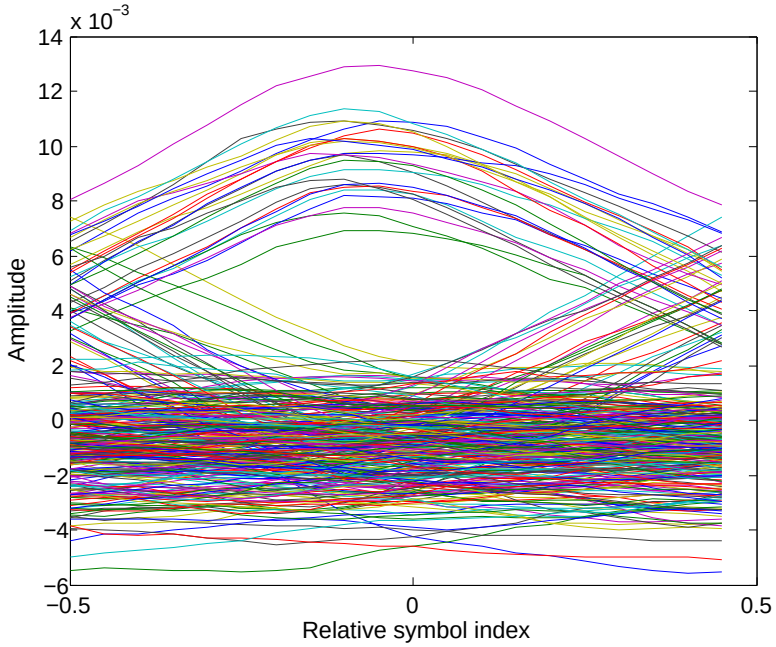

Figure 5.38: Eye diagram of received signal when EGC is used and no. of channels = 2.

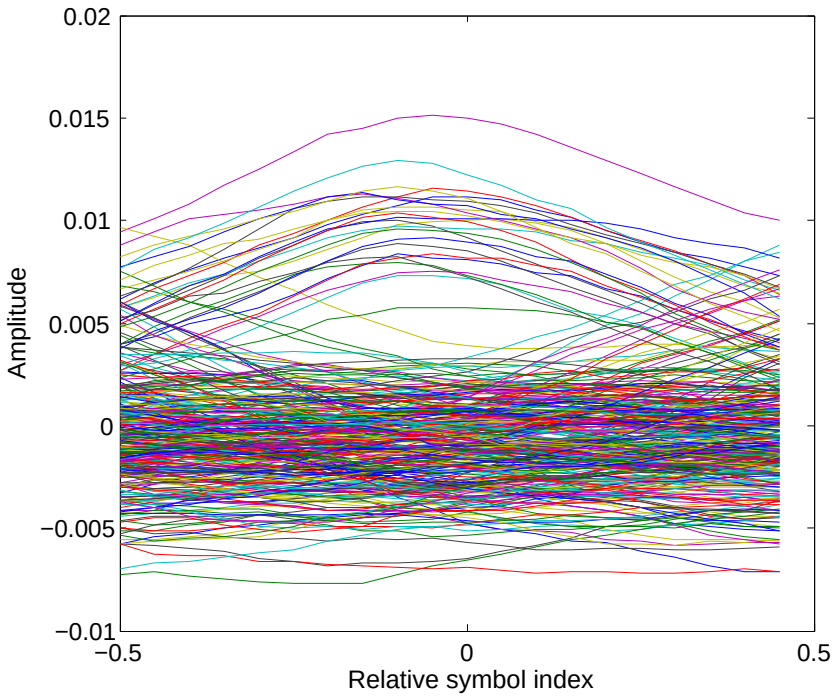

Figure 5.39: Eye diagram of received signal when EGC is used and no. of channels = 3.

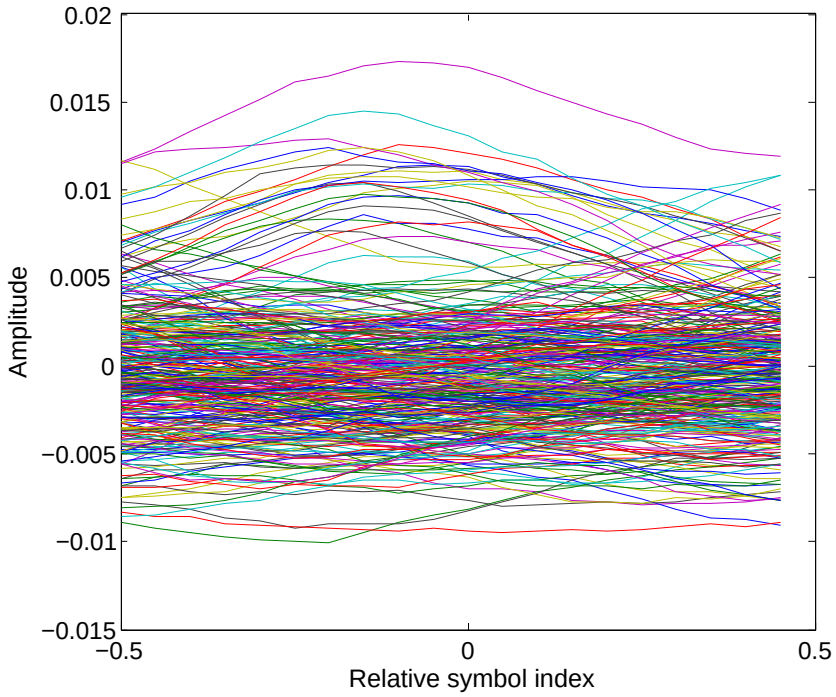

Figure 5.40: Eye diagram of received signal when EGC is used and no. of channels = 4.

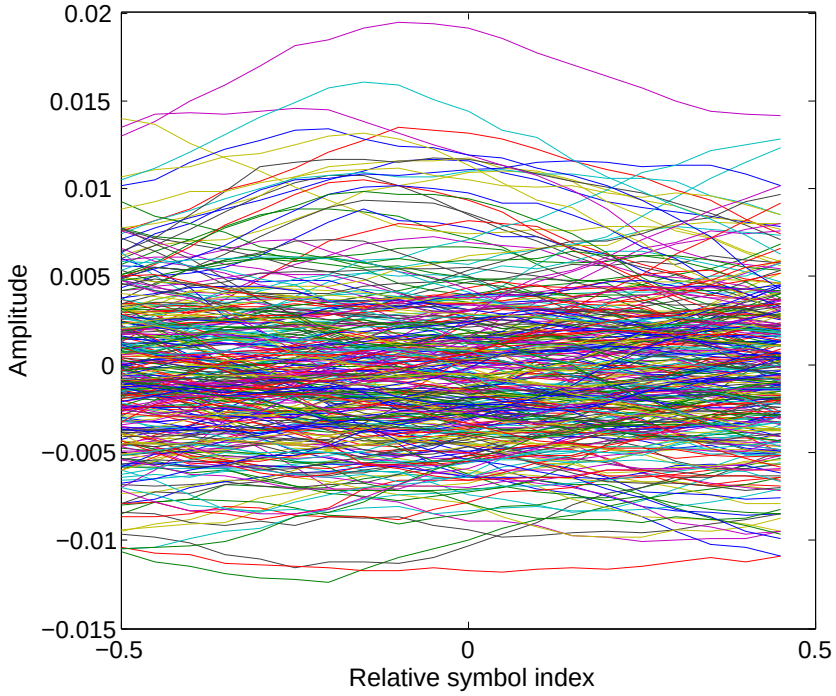

Figure 5.41: Eye diagram of received signal when EGC is used and no. of channels = 5.

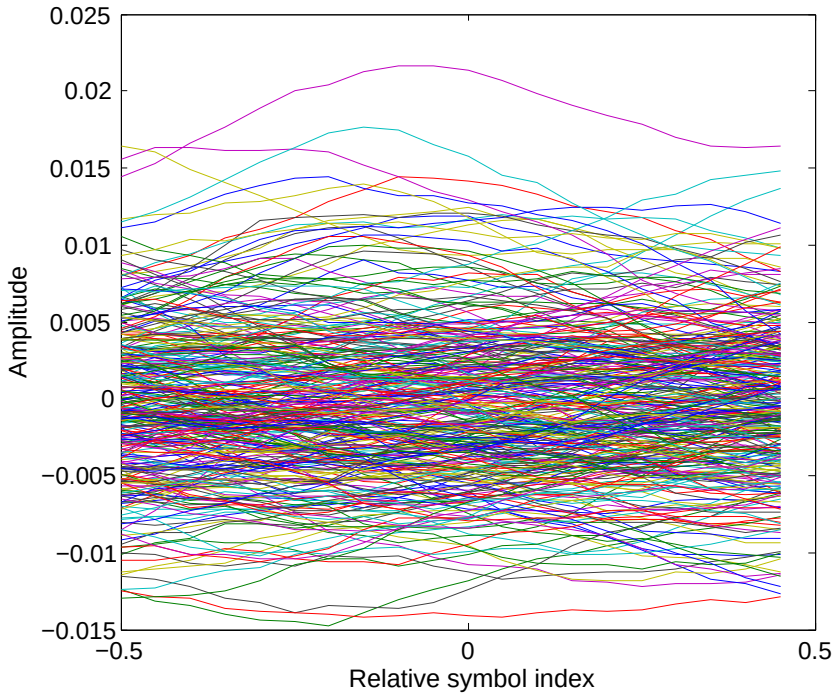

Figure 5.42: Eye diagram of received signal when EGC is used and no. of channels = 6.

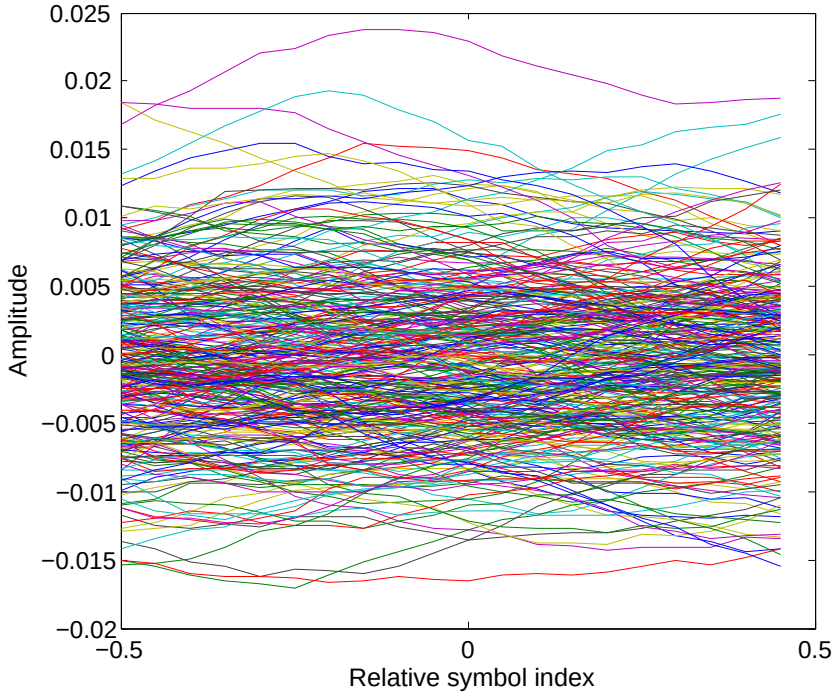

Figure 5.43: Eye diagram of received signal when EGC is used and no. of channels = 7.

5.4.3 Experimental Results

The primary result from this experiment is plotted in Fig. 5.35, which shows changes in SNR and the noise floor of the PSD, for the two different combining schemes, EGC and SEL, as the number of channels are increased from a traditional single-output system to all 7 channels in the prototype smart receiver. In all cases, only one receiver (the first one) is pointed towards and actively receiving data from the transmitter in this scenario. Hence the goal of the experiment is in managing non-active receivers using diversity combining techniques.

As expected, SEL combining always switches to the channel with the most power, while EGC gets incrementally worse as more channels are added. The term *diversity* is used loosely to imply that in a mobile situation, the channel with the most power changes as users change position. The combining technique is implemented on a packet basis and will select the ideal receiver channels as positions change. The SNR estimator used saturates below 10 dB and therefore an additional metric, the noise floor of the power spectral density of the combined signal, is also included in the figure for reference.

It is possible that in waters with very high attenuation coefficients, the multiply scattered photons typically carry more power than ballistic photons and as result will result in power at multiple receiver channels simultaneous. In this case, a more efficient combining technique such as maximum ratio combining will potentially be advantageous. More work is needed to study this scenario.

Figures 5.36 through Figure 5.43 help visualize the detrimental effects of simply summing all receiver outputs together. These plots show an eye diagram of the matched filter output as each channel is added. The opening of the eye can be seen to close as this happens.

5.5 Multiuser: CDMA and SDMA

One of the advantages of the proposed design is the spatial division multiple access (SDMA) inherent to the design. However, this is not applicable in two scenarios: first, when two or more transmitters are co-located, and second, when two or more different signals arrive at the same photodiode through two different lenses. In either case, SDMA is not applicable, and for this reason, code division multiple access (CDMA) spreading is employed at the transmitter. The codes used and their properties have been detailed in a previous section. Here, we experimentally validate simultaneous channel access using CDMA.

5.5.1 Experimental Setup

An experiment was conducted through water, with the receiver (User B) at the end of the tank, and two co-located transmitters (Users A and C) at the other end. Data was collected for the instances where only user A is transmitting, only user C is transmitting, and when both users A and C are simultaneously transmitting. The signal received at the receiver was digitized and processed with their results shown in Fig. 5.44. The results in Figs. 5.44a and 5.44b show strong correlation in the absence of interferers. Fig. 5.44c is consistent with theory as well, and shows multiple access interference (MAI) inherent to asynchronous multi-user CDMA. Although this degrades performance, a code-matched filter and multi-user detection techniques such as a decorrelating detector can be used to decouple users.

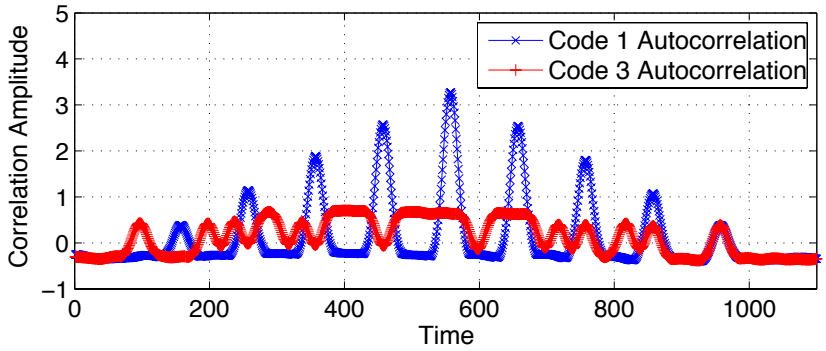

(a) User A (Code 1) *on*, User C (Code 3) *off*

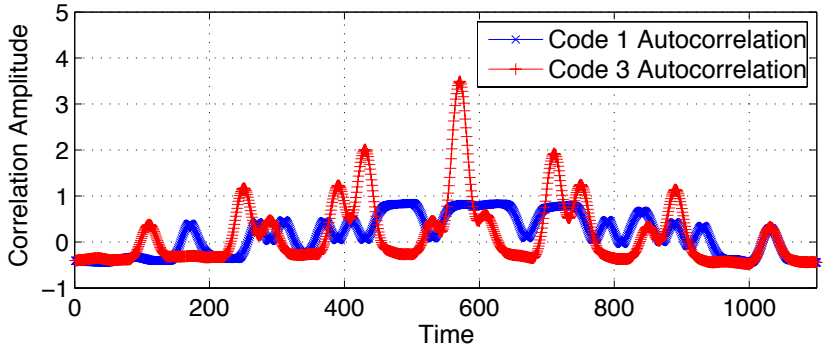

(b) User A (Code 1) *off*, User C (Code 3) *on*

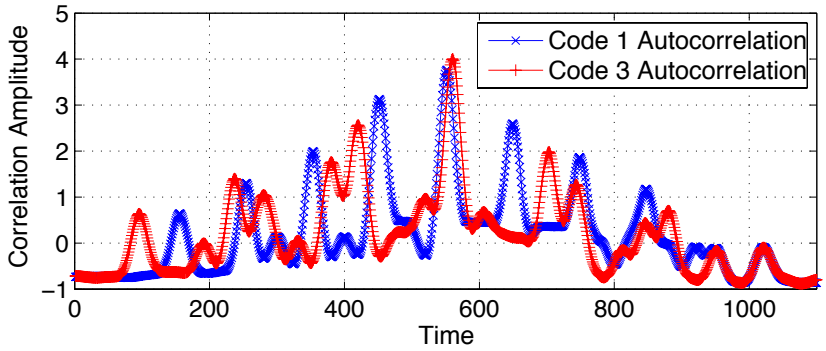

(c) User A (Code 1) *on*, User C (Code 3) *on*

Figure 5.44: Correlation of the received signal at User B from two different transmitters, User A and User C, with their outputs spread using the respective CDMA codes 1 and 3. Only User A is transmitting in (a), only User C is transmitting in (b), and both Users A and C are transmitting in (c). Graph shown is for a bit "1" spread using two different 32-chip prime codes. The bits are intentionally synchronized between the two transmitters for the sake of comparison, although synchronization between the transmitters is not required.

5.6 Discussion

Free-space optical communication is inherently line-of-sight and hence highly dependent on the field of views of, and pointing and tracking between, transmitters and receivers. The goal of this research has been to present one method of relaxing these requirements. The results show that in addition to satisfying this goal, the design is also capable of acting as a "smart" system with the additional sensing capabilities at the receiver and the control capabilities at the transmitter. The various experiments conducted in this chapter demonstrate the following:

- The characterization experiments reveal that it is possible to extend the directed FOV of a single lens-photodiode pair in multiple directions using the design described in this paper. It is also shown that, while the combined FOV has "nulls" in sensitivity, this can be mitigated by intentionally defocusing the receiver plane.

- The angle of arrival estimation algorithm presented, although preliminary, serves as a proof-of-concept that a simple pattern matching algorithm can obtain a single-axis angle of arrival. It is proposed that a more advanced precoding-based or Markov localization-based algorithm can provide a three-dimensional estimate.

- The backscatter estimation experiment demonstrates a linear relationship between the return beam intensity and channel attenuation coefficient. It is anticipated that higher level controls are required to co-ordinate the gain changes at the receiver required during this process, as well as that some calibrations are necessary to extend the laboratory tank measurements to the "real world."

- Through diversity combining experiments, it can be seen that selection combining is a better alternative to equal gain combining in an angular diversity scenario. However, it is expected that in highly scattering environments, an optimal maximum ratio combiner is desirable.

- Preliminary multi-user experiments conducted show that although CDMA is required in certain alignments of users, the design inherently acts as a spatial division multiple access system. Further experiments are necessary to verify whether, in a highly scattering environment in coordination with the CDMA coded transmitter outputs, a diversity combiner similar to techniques used in a RAKE receiver is beneficial.

5.7 Adaptive Coordination

So far we have seen the receiver capable of angle of arrival estimation, backscatter estimation, and diversity combining, in order to operate with a wide field of view (FOV) without loss in signal-to-noise ratio (SNR). The 7-channel transmitter is capable of switching its output power, data-rate, and direction. In this section, we close the loop between the receiver and the transmitter in order to demonstrate an adaptive system capable of primarily:

1. switching output direction based on estimated direction of other user, and
2. controlling output power and rate based on estimated water condition.

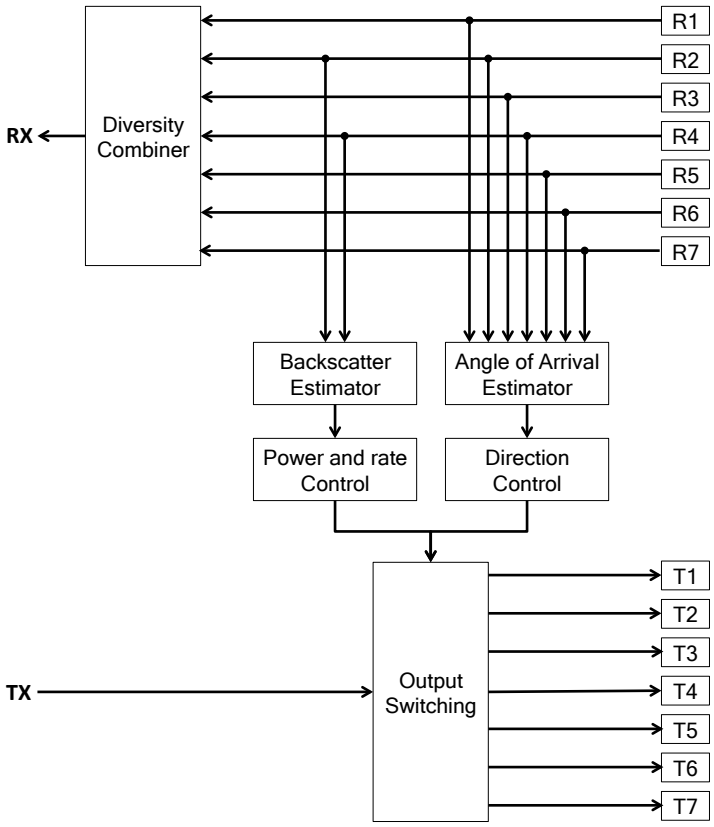

Figure 5.45: Closed-loop system architecture of smart-transceiver. The transmitter is capable of direction, output power, and rate control, based on feedback from backscatter and angle of arrival estimator at the receiver.

The block diagram shown in Fig. 5.45 takes advantage of the design and its capabilities to illustrate a closed-loop scenario. The output from the angle of arrival estimator is used by the transmitter to switch LEDs, and thus electronically beam steer its outputs. The output from the backscatter estimator is used to adjust the output power of the LEDs and, if necessary, other parameters such as the data rate and code rate. Currently, all processing takes place offline on a PC running MATLAB. However, the hardware constructed is capable of implementing this proposed closed-loop scheme on a field programmable gate array or other embedded digital signal processor. A few assumptions made for the prototype system are first mentioned.

- Since the total number of directions in the prototype transmitter output is limited to seven, the angle of arrival estimator outputs are averaged and binned in to seven states as well.
- As previously mentioned, in the absence of a simultaneous 7-channel high speed digitizer, this adaptive coordinated can only be demonstrated currently at low data rates.
- Also, being a prototype system, the loop is closed in software on a PC in post-processing. However, the capabilities exist in the prototype to be implemented in real-time.

Chapter 6

Conclusion

For short-range links, free-space optical communication is a promising alternative to acoustic and tethered communications underwater. As an example, consider an underwater sensor node that collects long term bio- and geo-physical data. Currently, such devices are recovered to offload their data before they are deployed again, which is a resource intensive task.

In the future, these underwater sensor nodes can use optical communication to wirelessly offload their data to an interrogating underwater vehicle equipped with an optical modem. Typically, where a physical connection would need to be made, the optical wireless would not require the mating of connectors for transferring the collected data. The high bandwidth of optical communications would reduce the amount of time the underwater vehicle would need to station keep over a sensor node. For sensor nodes that can harvest power from ocean currents or need to conserve power for long term operation, this also means shorter active times and ability to quickly return to its low power state.

Swarms of such sensor nodes and underwater vehicles can also use optical communication to communicate within and in between them. The directionality of free-space optical communication can be taken advantage of in situations where broadcast is not desired for security or multi-user reasons. The overarching goal of this research has been to position free-space optical communication as the physical layer enabling technology for such an ecosytem. The contributions and implications of the research is listed below, after a brief overview of the design goals.

6.1 Review of Goals

Underwater free-space optical communication is typically considered point-to-point which requires strict pointing and tracking especially on mobile platforms. This is reasonable for large systems that can afford dedicated gimbal systems. However, in some situations, compact systems are desired, which do not have the size or energy budget for sophisticated pointing and tracking.

For such situations, low-cost, compact solutions are desired. The primary goal of this research has been to relax pointing and tracking requirements inherent to free-space underwater optical communication. This goal can be divided into the design, development, and demonstration of:

- A smart transmitter that shall replace a diffuse transmitter with one that projects multiple narrow beams and electronically steer the beam within a large FOV.
- A smart receiver that shall replace a single-output fixed-FOV receiver with a segmented wide-FOV and estimate angle of arrival within that region.

Optical signals also undergo attenuation across a wide dynamic range in the underwater channel with changing water conditions. Therefore it is equally important that a smart transmitter shall also estimate the water quality and adapt accordingly in order to maintain a communications link.

6.2 Major Contributions

The major contributions of this dissertation lie in solving some of the inherent challenges of free-space optical communications such as field of view and pointing and tracking as well as some of the inherent challenges of the underwater optical channel such as quickly and wildly varying channel attenuations.

In this research we show that pointing and tracking requirements can be relaxed by using wide FOV smart receivers and transmitters with angle of arrival estimation and electronic beam steering. The angle of arrival estimated by the receiver is passed to the transmitter which can steer its output beam in that direction. The wide FOV is segmented which provides a few additional benefits. At the receiver the segmented FOV provides multiple output channels which enable the isolation of the signal bearing channel so as to null channels with background interference. The multiple channels also provide better combining techniques based on the channel conditions as well as simultaneous reception from multiple users. At the transmitter, multiple narrow output beams, as opposed to a single diffused output allows the transmitter to only transmit in the desired direction. The transmitter can also transmit separate output streams of data in different directions.

This research also shows that a smart transmitter can adapt to the wide dynamic range of optical attenuation in the underwater channel by using a new technique to estimate the water quality from backscatter measurements. The smart receiver synchronizes with and measures the backscatter from its co-located transmitter. This provides an estimate of water quality (channel state) at the transmitter. The transmitter uses this information to adapt to changing water conditions by changing its output power and rate.

Moreover, this research shows that sensing information can be collected from the communications link and not only used to improve the performance of the link but also to act as sensor data. For example, the angle of arrival estimation, in addition to providing feedback to adapt the transmitter output direction, also serves as a localization sensor. Similarly, the backscatter estimation, in addition to providing feedback to adapt the transmitter output power and rate, also serves as a water quality sensor.

Finally, the smart receivers and transmitters designed and demonstrated also employ improvements in the front-end optics and electronics. The smart receiver prototype built uses a novel lens-detector array with *n:n* correspondence between the n lenses and n detectors (optical reuse). This is an improvement over previous systems that either use a lens array or a detector array. The transmitter electronics front-end uses a new DAC-based bias-tee circuit which is ideal for driving diode lasers or LEDs at high currents in the few tens of MHz bandwidth.

6.3 Prototype Specifications

The prototype that has been constructed as part of this research serves different purposes. It acts as a demonstration of the contributing ideas of the thesis while simultaneously functioning as a characterization platform. It also shows feasibility of a low-cost and low-size, -weight, and -power platform to achieve these goals.

Demonstrating the primary focus of the research, the prototype smart receiver and transmitter has a segmented wide field of view of 90 to 120 degrees. The prototype system can also operate at a data rate as high as 10 Mbps/ch. This is limited by the use of LEDs at the transmitter and large area photodiodes at the receiver.

An array of diode lasers with opal diffusers can be used at the transmitter to increase the output data rate. A laser diode driver such as the MAX3701 from Maxim IC can support data rates as high as 400 Mbps. The smart receivers can use photomultiplier tubes as detectors in order to increase receiver responsivity and bandwidth. A photomultiplier tube such as the Hamamatsu R3809U has a bandwidth of approximately 2 GHz with a 11 mm diameter active area and sensitivity of 70 mA/W at its peak response of 430 nm. Thus all of the other aspects of the smart transmitter and receiver can be maintained while replacing the light source and detector if it is desired to operate at a higher data rate at the expense of additional resources.

The prototype system also has seven channels, which was chosen to remain within eight, a standard number of channels for COTS multi-channel digitizers and ADC ICs. Additional resources would also allow this number of channels to be increased. This would increase the resolution of the segmentation of the wide field of view at the receiver and the beam forming directions at the transmitter.

6.4 Future Work

The following is a list of some of the extensions of this dissertation.

- **Monte Carlo numerical simulation**: A Monte Carlo numerical simulation of the multiple aperture segmented-wide-FOV smart receiver is useful. Beer's law underestimates the received power in highly turbid environments. A simulation can accurately predict the power loss, especially as it relates to the multiples FOVs and aperture sizes a smart receiver is capable of switching between. Simulation can also validate performance in various misalignment scenarios.

- **Extension of angle of arrival estimation**: The angle of arrival estimation algorithm used in this dissertation is a lookup table based algorithm and only used as a proof of concept. A more rigorous angular estimation algorithm is desired for practical implementation. Such an algorithm can also benefit from using machine learning methods that take advantage of the uniqueness between the angle of incident light and the pattern formed on the receiver plane.

- **Extension of channel estimation through backscatter measurement**: Additional experiments of backscatter measurements in a laboratory environment are desired. These experiments can also include changes in channel albedo. Channel albedo can be changed by the addition of absorptive dyes in addition to scattering agents. Window effects and hysteresis effects are also potentially interesting to investigate.

- **Closing the adaptive feedback loop**: The angle of arrival information from the smart receiver can be used by the smart transmitter to beam steer its output direction. Similarly the channel estimation through backscatter measurement can be used to adjust the transmitter output power and rate. While this dissertation demonstrates these capabilities as proof of concept, additional work is required to close the adaptive feedback loop for real-time operation.

- **Smart receiver design improvements**:

  - **Number of channels**: Increasing the number of lenses and/or the number of photodiodes as well as the ratio of number of photodiodes to lenses is a natural extension of the front-end optical design. For a higher number of photodiodes, a hybrid combining technique is worth investigating where a few local photodiodes are combined in analog in order to maintain the total number of digitized signals at or less than the number of digitizer channels available.

  - **Asymmetric placements of detectors**: It is potentially useful in investigating designs that used asymmetric placement of detectors on the detector plane. This further increases the uniqueness of the correspondence between the incident light of the receiver and the pattern on the receiver plane. It is also potentially worth investigating a coded placement of detectors. Additionally, a larger number of detectors can be used, which are then sparsely sampled. The detectors that are sampled can be changed between subsequent sampling periods.
  - **Other detectors**: The detectors at the receiver can be replaced with photomultiplier tubes or other types of detectors. It is also worth investigating the use of multi-element detectors such as bi-cell, quadrant, or linear array Si PIN photodiodes. Another advantage of a segmented wide FOV that has not been investigated is the use of optical filters which is typically challenging to implement for a large aperture wide FOV receiver.

- **Smart transmitter design improvements**:
  - **Number of channels**: The number of LEDs can be increased for higher beam steering resolution. Each transmitter output address can also be shared between multiple local LEDs to increase tessellation without increasing number of output channels.
  - **Other light sources**: The LEDs can also be replaced with diode lasers with diffusers to increase the output optical power. The LEDs and/or diode lasers can also be enclosed within a diffusing dome.

- **Field tests on underwater vehicle**: Implementing the smart system on an underwater vehicle is useful in validating the benefits and understanding performance against IMU measurements obtained from the vehicle's sensors. Multiple underwater vehicles, in formation, can leverage the multi-user and sensory capabilities to test new networking schemes.

6.5 Conclusion

This dissertation demonstrates the feasibility of implementing smart transmitters and receivers for free-space underwater optical communication systems, and presents data obtained in a tank designed to simulate ocean water conditions. The smart receivers have increased field of view and the ability to estimate angle of arrival. The prototype 7-channel lens-photodiode array smart receiver constructed has a segmented total combined field of view of $\sim 120^{\circ}$. The transmitters are

quasi-omnidirectional, allow electronic switched beam steering, and with an adjacent receiver, enable estimation of water quality by measuring the optical backscatter from transmitted light.

This smart transceiver approach mitigates pointing and tracking requirements, which can be difficult for underwater platforms and enable adaptive communication techniques, which are expected to be useful due to the variable dynamic range of the communications signal as platforms change relative range and pose. Thus, we anticipate that implementations such as those presented techniques will be useful in enabling a physical layer for networking schemes in swarms of unmanned underwater vehicles in the future.

REFERENCES

[1] C. Pontbriand, N. Farr, J. Ware, J. Preisig, and H. Popenoe. Diffuse high-bandwidth optical communications. In *OCEANS 2008*, pages 1–4. IEEE, 2008.

[2] Brandon Cochenour, Linda Mullen, and Alan Laux. Phase Coherent Digital Communications for Wireless Optical Links in Turbid Underwater Environments. In *Oceans 2007*, pages 1–5. IEEE, 2007.

[3] M. Doniec, I. Vasilescu, M. Chitre, C. Detweiler, M. Hoffmann-Kuhnt, and D. Rus. AquaOptical: A lightweight device for high-rate long-range underwater point-to-point communication. In *OCEANS 2009, MTS/IEEE Biloxi - Marine Technology for Our Future: Global and Local Challenges*, pages 1–6, 2009.

[4] Frank Hanson and Stojan Radic. High bandwidth underwater optical communication. *Applied Optics*, 47(2):277, January 2008.

[5] William C. Cox. *A 1 Mbps Underwater Communication System Using a 405 nm Laser Diode and Photomultiplier Tube.* M.s. thesis, North Carolina State University, Raleigh, NC, 2007.

[6] Jim A. Simpson. *A 1 Mbps Underwater Communications System using LEDs and Photodiodes with Signal Processing Capability.* M.s. thesis, North Carolina State University, Raleigh, NC, 2007.

[7] Robert L Gallagher. Laser beams hold promise for submarine communication. *EIR*, 15(30), 1988.

[8] Sherman Karp. Optical communications between underwater and above surface (satellite) terminals. *Communications, IEEE Transactions on*, 24(1):66–81, 1976.

[9] T. Wiener and S. Karp. The role of blue/green laser systems in strategic submarine communications. *Communications, IEEE Transactions on*, 28(9):1602–1607, September 1980.

[10] J.J. Puschell, R.J. Giannaris, and Larry Stotts. The Autonomous Data Optical Relay Experiment: first two way laser communication between an aircraft and submarine. In *Telesystems Conference, 1992. NTC-92., National*, pages 14–27. IEEE, 1992.

[11] Judith Bannon Snow, James P Flatley, Dennis E Freeman, Mark A Landry, Carl E Lindstrom, Jacob R Longacre, and Joshua A Schwartz. Underwater propagation of high data rate laser communications pulses. In *Ocean Optics XI*, volume 1750. SPIE, 1992.

[12] Mark Alan Chancey. *Short Range Underwater Optical Communication Links.* M.s. thesis, North Carolina State University, Raleigh, NC, 2005.

[13] Tommy Oberg, Bernt Nilsson, Niten Olofsson, Magnus Nordenvaad, and Erland Sangfelt. Underwater communication link with iterative equalization. *Oceans 2006*, (1):1–6, September 2006.

[14] A Goalie and Joel Trubuil. Channel coding for underwater acoustic communication system. *OCEANS 2006*, (Cc):3–6, 2006.

[15] Ivan B. Djordjevic. Coding for free space optical communications. *LEOS 2008 - 21st Annual Meeting of the IEEE Lasers and Electro-Optics Society*, 1:884–885, November 2008.

[16] Jing Li and Murat Uysal. Achievable information rate for outdoor free space optical communication with intensity modulation and direct detection. In *Global Telecommunications Conference, 2003.*, pages 2654–2658, 2003.

[17] William C. Cox, Jim A. Simpson, Carlo P. Domizioli, John F. Muth, and Brian L. Hughes. An underwater optical communication system implementing Reed-Solomon channel coding. In *Proc. OCEANS Conf. 2008*, pages 1–6, Quebec, Canada, 2008. Ieee.

[18] J.S. Everett. *Forward-Error Correction Coding for Underwater Free-space Optical Communication.* M.s. thesis, North Carolina State University, Raleigh, NC, 2009.

[19] Jim A. Simpson, William C. Cox, John R. Krier, and Brandon Cochenour. 5 Mbps optical wireless communication with error correction coding for underwater sensor nodes. In *Proc. OCEANS Conf. 2010*, pages 6–9, Seattle, WA, 2010.

[20] William C. Cox, Brian L. Hughes, and John F. Muth. A polarization shift-keying system for underwater optical communications. In *Proc. OCEANS Conf. 2009*, pages 1–4, Biloxi, MS, 2009. IEEE.

[21] William C. Cox, Kory F. Gray, Jim A. Simpson, Brandon Cochenour, Brian L. Hughes, and John F. Muth. A MEMS Blue / Green Retroreflecting Modulator for Underwater Optical Communications. In *Proc. OCEANS Conf. 2010*, Seattle, WA, 2010.

[22] Jim A. Simpson, Brian L. Hughes, and John F. Muth. A spatial diversity system to measure optical fading in an underwater communications channel. In *Proc. OCEANS Conf. 2009*, pages 1–6, Biloxi, MS, 2009. IEEE.

[23] N. Farr, A. Chave, L. Freitag, J. Preisig, S. White, D. Yoerger, and P. Titterton. Optical Modem Technology for Seafloor Observatories. In *Proceedings of OCEANS 2005 MTS/IEEE*, pages 1–7. IEEE, 2005.

[24] N. Farr, A. Bowen, J. Ware, C. Pontbriand, and M. Tivey. An integrated, underwater optical /acoustic communications system. In *OCEANS'10 IEEE SYDNEY*, pages 1–6. IEEE, May 2010.

[25] N. Farr, J. Ware, C. Pontbriand, T. Hammar, and M. Tivey. Optical communication system expands CORK seafloor observatory's bandwidth. In *OCEANS 2010 MTS/IEEE SEATTLE*, pages 1–6. IEEE, September 2010.

[26] I. Vasilescu, K. Kotay, D. Rus, L. Overs, P. Sikka, M. Dunbabin, P. Chen, and P. Corke. Krill: An Exploration in Underwater Sensor Networks. In *The Second IEEE Workshop on Embedded Networked Sensors, 2005. EmNetS-II.*, pages 151–152. IEEE, 2005.

[27] M. Dunbabin, P. Corke, I. Vasilescu, and D. Rus. Data muling over underwater wireless sensor networks using an autonomous underwater vehicle. In *Proceedings 2006 IEEE International Conference on Robotics and Automation, 2006. ICRA 2006.*, pages 2091–2098. IEEE, 2006.

[28] Carrick Detweiller, Iuliu Vasilescu, and Daniela Rus. An Underwater Sensor Network with Dual Communications, Sensing, and Mobility. In *OCEANS 2007 - Europe*, pages 1–6. IEEE, June 2007.

[29] M Doniec, C Detweiler, I Vasilescu, and D Rus. Using optical communication for remote underwater robot operation. In *2010 IEEE/RSJ International Conference on Intelligent Robots and Systems*, pages 4017–4022. IEEE, October 2010.

[30] Marek Doniec and Daniela Rus. BiDirectional optical communication with AquaOptical II. In *2010 IEEE International Conference on Communication Systems*, pages 390–394. IEEE, November 2010.

[31] A Laux, R Billmers, L Mullen, Brian Concannon, J Davis, J Prentice, and V Contarino. The a, b, cs of oceanographic lidar predictions: a significant step toward closing the loop between theory and experiment. *Journal of Modern Optics*, 49(3):439–451, 2002.

[32] Brandon Cochenour, Linda Mullen, Alan Laux, and Tom Curran. Effects of Multiple Scattering on the Implementation of an Underwater Wireless Optical Communications Link. In *OCEANS 2006*, pages 1–6. IEEE, September 2006.

[33] Brandon M. Cochenour, Linda J. Mullen, and Alan E. Laux. Characterization of the Beam-Spread Function for Underwater Wireless Optical Communications Links. *IEEE Journal of Oceanic Engineering*, 33(4):513–521, October 2008.

[34] Brandon Cochenour, Linda Mullen, and John Muth. Effect of scattering albedo on attenuation and polarization of light underwater. *Optics Letters*, 35(12):2088, June 2010.

[35] Linda Mullen, Brandon Cochenour, William Rabinovich, Rita Mahon, and John Muth. Backscatter suppression for underwater modulating retroreflector links using polarization discrimination. *Applied Optics*, 48(2):328, January 2009.

[36] Linda Mullen, Alan Laux, and Brandon Cochenour. Propagation of modulated light in water: implications for imaging and communications systems. *Applied Optics*, 48(14):2607, May 2009.

[37] Linda Mullen, Derek Alley, and Brandon Cochenour. Investigation of the effect of scattering agent and scattering albedo on modulated light propagation in water. *Applied Optics*, 50(10):1396, March 2011.

[38] Frank Hanson and Mark Lasher. Effects of underwater turbulence on laser beam propagation and coupling into single-mode optical fiber. *Applied Optics*, 49(16):3224–3230, June 2010.

[39] Shlomi Arnon. Underwater optical wireless communication network. *Optical Engineering*, 49(1):015001, 2010.

[40] Shlomi Arnon and Debbie Kedar. Non-line-of-sight underwater optical wireless communication network. *JOSA A*, 26(3):530–539, March 2009.

[41] Hoa Le Minh, Dominic O'Brien, Grahame Faulkner, Dominic O Brien, Lubin Zeng, Kyungwoo Lee, Daekwang Jung, and Yunje Oh. 80 Mbit/s visible light communications using pre-equalized white LED. *Communication,*, 5(September):223–224, 2008.

[42] D. O'Brien and G. Faulkner. 100-Mb/s NRZ Visible Light Communications Using a Postequalized White LED. *IEEE Photonics Technology Letters*, 21(15):1063–1065, August 2009.

[43] Kaiyun Cui, Gang Chen, Qunfeng He, and Zhengyuan Xu. Indoor optical wireless communication by ultraviolet and visible light. In *Proceedings of SPIE*, volume 7464, pages 74640D–74640D–9. SPIE, August 2009.

[44] Teresa Mengual, Borja Vidal Rodriguez, Chrysavgi Stoltidou, Sebastian Blanch, Javier Martí, Lluís Jofre, Iain McKenzie, and Juan Manuel Del Cura. Optical Beamforming Network with Multibeam Capability Based on a Spatial Light Modulator - OSA Technical Digest (CD). In *Optical Fiber Communication Conference and Exposition and The National Fiber Optic Engineers Conference*, page JThA71. Optical Society of America, February 2008.

[45] Paul F. McManamon, Philip J. Bos, Michael J. Escuti, Jason Heikenfeld, Steve Serati, Huikai Xie, and Edward A. Watson. A Review of Phased Array Steering for Narrow-Band Electrooptical Systems. *Proceedings of the IEEE*, 97(6):1078–1096, June 2009.

[46] Chulwoo Oh, Jihwan Kim, John Muth, Steve Serati, and Michael J. Escuti. High-Throughput Continuous Beam Steering Using Rotating Polarization Gratings. *IEEE Photonics Technology Letters*, 22(4):200–202, February 2010.

[47] Ke Wang, Ampalavanapillai Nirmalathas, Christina Lim, and Efstratios Skafidas. Impact of background light induced shot noise in high-speed full-duplex indoor optical wireless communication systems. *Optics Express*, 19(22):21321, October 2011.

[48] Ke Wang, Ampalavanapillai Nirmalathas, Christina Lim, and Efstratios Skafidas. 12.5 Gbps Indoor Optical Wireless Communication System with Single Channel Imaging Receiver - OSA Technical Digest (CD). In *37th European Conference and Exposition on Optical Communications*, page Tu.3.C.6. Optical Society of America, September 2011.

[49] A.P. Tang, J.M. Kahn, and K.P. Ho. Wireless infrared communication links using multibeam transmitters and imaging receivers. In *Communications, 1996. ICC 96, Conference Record, Converging Technologies for Tomorrow's Applications. 1996 IEEE International Conference on*, volume 1, pages 180–186. IEEE, 1996.

[50] J.M. Kahn, R. You, P. Djahani, A.G. Weisbin, B.K. Teik, and A. Tang. Imaging diversity receivers for high-speed infrared wireless communication. *Communications Magazine, IEEE*, 36(12):88–94, 1998.

[51] P. Djahani and J.M. Kahn. Analysis of infrared wireless links employing multibeam transmitters and imaging diversity receivers. *IEEE Transactions on Communications*, 48(12):2077–2088, 2000.

[52] J.B. Carruther and J.M. Kahn. Angle diversity for nondirected wireless infrared communication. *IEEE Transactions on Communications*, 48(6):960–969, June 2000.

[53] J. Akella, C. Liu, D. Partyka, M. Yuksel, S. Kalyanaraman, and P. Dutta. Building blocks for mobile free-space-optical networks. In *Wireless and Optical Communications Networks, 2005. WOCN 2005. Second IFIP International Conference on*, pages 164–168. IEEE, 2005.

[54] J. Akella, M. Yuksel, and S. Kalyanaraman. Error analysis of multi-hop free-space optical communication. In *Communications, 2005. ICC 2005. 2005 IEEE International Conference on*, volume 3, pages 1777–1781. IEEE, 2005.

[55] A. Sevincer, M. Bilgi, M. Yuksel, and N. Pala. Prototyping Multi-Transceiver Free-Space Optical Communication Structures. In *Communications (ICC), 2010 IEEE International Conference on*, pages 1–5. IEEE, 2009.

[56] M. Bilgi, M. Yuksel, and Nezih Pala. 3-D Optical Wireless Localization. In *Proceedings of IEEE GLOBECOM Workshop on Optical Wireless Communications (OWC)*, 2010.

[57] B. Nakhkoob, M. Bilgi, M. Yuksel, and M. Hella. Multi-transceiver optical wireless spherical structures for manets. *Selected Areas in Communications, IEEE Journal on*, 27(9):1612–1622, 2009.

[58] Nils Gunnar Jerlov. *Optical oceanography.* Elsevier oceanography series, 5. Elsevier Pub. Co.,, Amsterdam, 1968.

[59] Milton Kerker. *The scattering of light, and other electromagnetic radiation.* Physical chemistry ; v. 16. Academic Press, New York, 1969.

[60] Nils Gunnar Jerlov and E Steemann Nielsen. *Optical aspects of oceanography : [collection of the papers presented at the Symposium on Optical Aspects of Oceanography held at the Institute of Physical Oceanography in Copenhagen, 19th-23rd June 1972].* Academic Press, London, 1974.

[61] Rudolph W Preisendorfer. *Hydrologic optics.* U.S. Dept. of Commerce, National Oceanic and Atmospheric Administration, Environmental Research Laboratories, Pacific Marine Environmental Laboratory,, Honolulu, 1976.

[62] Marvin A Blizard. *Ocean optics VII, June 25-28, 1984, Monterey, California.* Proceedings of SPIE–the International Society for Optical Engineering ; v. 489. International Society for Optical Engineering, Bellingham, Wash., USA, 1984.

[63] K. S Shifrin. *Physical optics of ocean water.* AIP translation series. American Institute of Physics, New York, 1988.

[64] Curtis D Mobley. *Light and water : radiative transfer in natural waters.* Academic Press, San Diego, 1994.

[65] Richard W Spinrad, Kendall L Carder, and Mary Jane Perry. *Ocean optics*. Oxford monographs on geology and geophysics ; no. 25. Oxford University Press ; Clarendon Press, New York, 1994.

[66] Frank M. Caimi. *Selected papers on underwater optics*. SPIE milestone series ; v. MS 118. SPIE Optical Engineering Press, Bellingham, Wash., USA, 1995.

[67] Curtis Mobley. Ocean Optics Web Book, 2011.

[68] Howard Gordon. Can the Lambert-Beer Law Be Applied to the Diffuse Attenuation Coefficient of Ocean Water? *Limnology and Oceanography*, 34(8):1389–1409, 1989.

[69] D Stramski, E Boss, D Bogucki, and K Voss. The role of seawater constituents in light backscattering in the ocean. *Progress In Oceanography*, 61(1):27–56, April 2004.

[70] Sherman Karp. *Optical channels : fibers, clouds, water, and the atmosphere*. Applications of communications theory. Plenum Press,, New York, 1988.

[71] William K Pratt. *Laser communication systems*. Wiley series in pure and applied optics. Wiley, New York, 1969.

[72] Ronald G Driggers. *Encyclopedia of optical engineering*. Marcel Dekker,, New York, 2003.

[73] W.S. Rabinovich, R. Mahon, P.G. Goetz, E. Waluschka, D.S. Katzer, S.C. Binari, and G.C. Gilbreath. A cat's eye multiple quantum-well modulating retro-reflector. *IEEE Photonics Technology Letters*, 15(3):461–463, March 2003.

[74] P. Prucnal and M. Santoro. Spread spectrum fiber-optic local area network using optical processing. *Journal of Lightwave Technology*, 4(5):547–554, 1986.

[75] David Haubrich, Joe Musser, and Edward S Fry. Instrumentation to measure the backscattering coefficient b(b) for arbitrary phase functions. *Applied optics*, 50(21):4134–47, July 2011.

APPENDIX

Appendix A

Embedded Real-Time Underwater Free-Space Optical Communication System with Error Correction Coding

A.1 Introduction

We have previously developed [5, 6] a laboratory laser diode- and LED-based optical communication system. The incorporation and use of all digital signal processing and error correction coding has allowed us to extend the range and bandwidth of free-space optical communication underwater. The capabilities of these systems prove promising to an array of applications in underwater communications, especially for and between sensor nodes and underwater vehicles. The goal of this research is to develop a small, embedded, low-cost, deployable platform to demonstrate some of the features of the underwater free-space optical communication system. The following sections detail the construction of such a system and its testing in underwater environments.

The system consists of a transmitter and receiver packaged in custom pressure vessels. The transmitter is capable of sending data at 5 or 10 Mbps. A (255,223) Reed-Solomon error correction code is employed to encode the transmitted bits. This allows the system to operate at a lower signal-to-noise ratio (SNR) for a given bit-error-rate (BER). This particular code has a performance gain of ~ 4 dB at a BER of 10^{-5}. Both the transmitter and receiver interfaces to external devices using 10BASE-T ethernet.

For experimental validation, the device was placed in a 12 ft. long, 4 ft. deep indoor water

tank. A commercial antacid, Maalox, was also added to the water to set the attenuation coefficient to levels corresponding to natural waters. The system was also tested in a 25 ft. indoor water tank. Finally the transmitter was interfaced with, and mounted to, an underwater vehicle and the link was tested in a swimming pool environment.

A.2 Background

Underwater sensor nodes can have a variety of instruments collecting environmental, acoustic, and video data. As an alternative to physically retrieving the node or making a physical connection to download the data or laying cable or fiber optic to the sensor node, underwater optical wireless communications potentially offer a high-bandwidth, although relatively short-range, solution. Underwater vehicles can also relay telemetry or video information and receive command and control signals over an optical link. Such links would require low-latency, real-time operation in addition to a high bandwidth.

High power, inexpensive LEDs and diode lasers operating in the blue-green region of the optical spectrum are available and can be modulated from a few Mbps to tens of Mbps. Several groups have investigated the use of such sources for short-range underwater optical communication. Error correction coding has been shown to improve the performance of such links to extend the range and to reduce bit error rates so that the system performance can approach theoretical communication system limits.

Researchers have demonstrated successful links at 10 Mbps at over 100 m in clear ocean water. The link was implemented on an underwater vehicle to be used as a data mule to avoid physically recovering instruments to offload data [24]. Others have demonstrated the real-time remote control of an underwater vehicle using a free-space optical communication system in a swimming pool environment [29].

A.2.1 Prior Work in Underwater Free-Space Optical Communication

We have previously developed systems for underwater free-space optical communication that use laser sources and photomultiplier tubes as detectors [5] as well as LEDs and photodiodes [6], both capable of implementing digital signal processing techniques.

For laboratory testing, a 3.66 m long, 1.22 m wide, 1.22 m tall indoor water tank was constructed. Maalox, a commercial antacid was added as a scattering agent. The addition of Maalox controls the attenuation coefficient of water, while absorption can be independently controlled by adding Nigrosin dye to control the albedo [37]. During the progression of an experiment, Maalox was added in a controlled manner using a programmable syringe pump. The resulting sweep results in a reproducible relationship between attenuation coefficient and

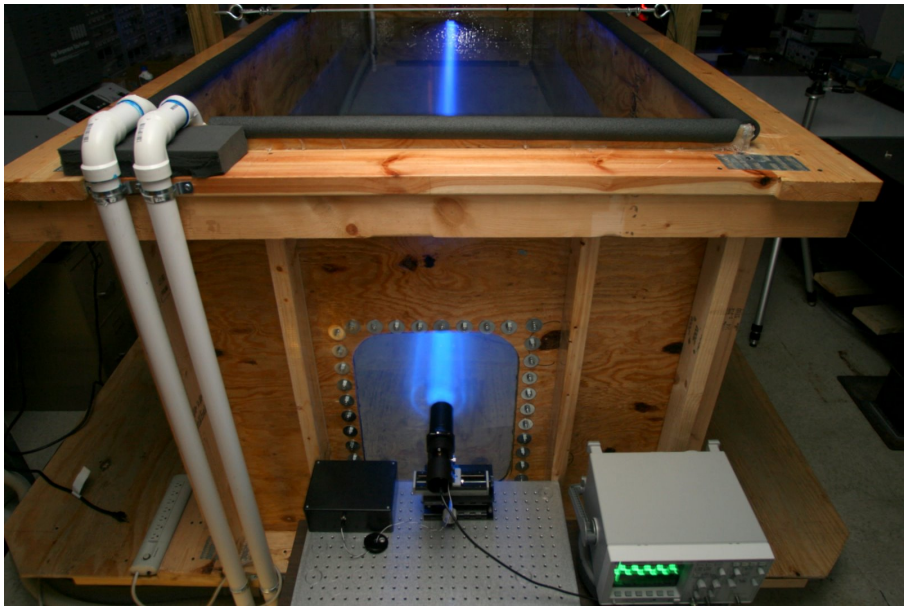

Figure A.1: 1000 gallon water tank built and used for underwater free-space optical communication experiments done at NCSU.

the electrical signal-to-noise ratio (SNR) of the received signal as shown in Figure A.2.

On compact platforms that we have built, to improve the performance of the links, forward error correction was added and theoretical and experimental performance was compared [18],[19]. Reed-Solomon, turbo, and low-density parity-check (LDPC) codes were implemented and their performance compared. The (255,129) Reed-Solomon code provides a coding gain of 2.5 dB over uncoded data at a bit-error-rate of 10^{-4}. UMTS and CCSDS turbo codes provide gains ranging from 6.8 dB to 9.5 dB for code rates ranging from 1/2 to 1/6. The DVB-S2 LDPC code provides a gain of 7.7 dB to 9.2 dB for rates from 1/2 to 1/4.

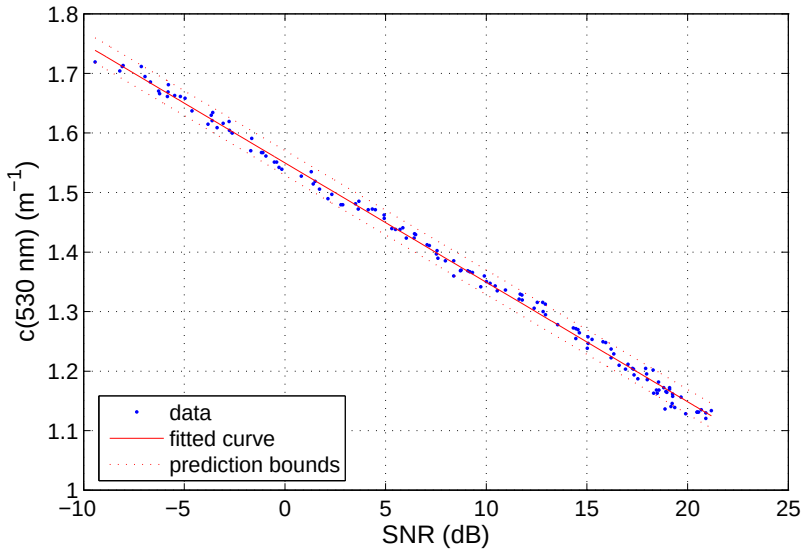

Figure A.2: Relationship between attenuation coefficient and SNR for experiments in laboratory test tank. Attenuation and albedo are controlled by introducing measured amounts of scattering particles such as liquid Maalox and Nigrosin dye to mimic ocean water.

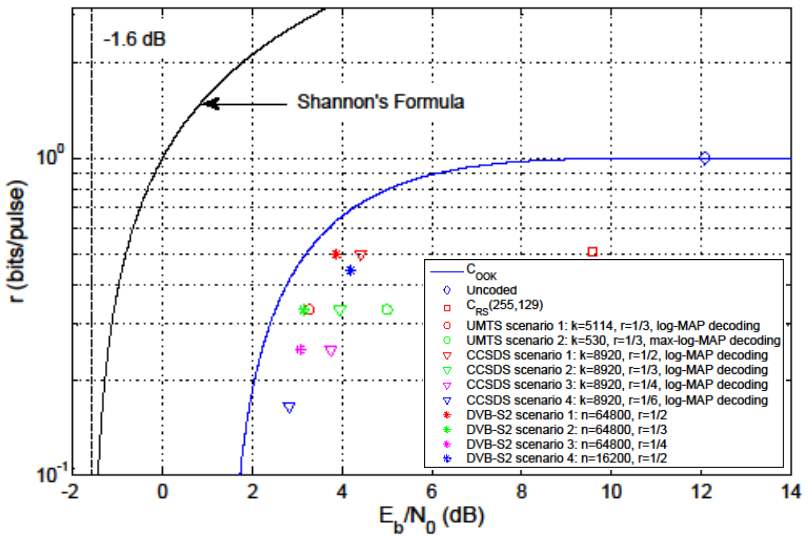

Figure A.3: Experimental performance of various error correction codes implemented for underwater free-space optical communication at NCSU as a function of code rate vs. performance in E_b/N_0 at a BER of 10^{-4}.

A.3 System Description

An FPGA-based embedded system coupled with an LED-based transmitter and a photodiode based receiver is constructed to create a testing and demonstration platform. It is also designed to be low cost and space conserving. A brief technical description of the platform is given below.

A.3.1 Transmitter

The underwater transmitter consists of all the electronics packaged within the submersible transmitter enclosure. The transmitter performs three main functions: it acts as an interface to the sensor node, performs error correction encoding, and acts as an interface to the LED transmitter. All three of these are achieved by the use of a Field Programmable Gate Array (FPGA). The FPGA used in this work is from the Altera Devices Cyclone II series. The FPGA interfaces with the data source over 10BASE-T ethernet and buffers the incoming data. The FPGA then encodes the data using a Reed-Solomon (RS) encoder for error correction coding. The data is further encoded using return to zero (RZ) and sent to the LED Driver. The LED driver uses an array of NMOS transistors to drive a high power LED. The high power LEDs used are from the CREE XR7090 series. A block diagram of the transmitter architecture is given in Figure A.4.

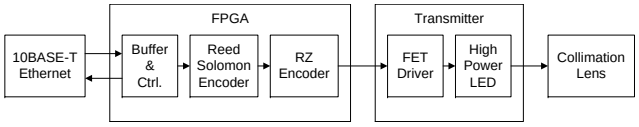

Figure A.4: Block Diagram of Transmitter.

Three separate LEDs with different wavelengths, blue (470 nm), green (525 nm), and white (with a strong peak at 470 nm), were used to conduct experiments. These LEDs could be effectively modulated at data rates as high as 5 Mbps for RZ encoded data or 10 Mbps for non-RZ data. The transmitter electronics and LED were powered using two separate battery arrays. Each array consisted of two lithium-ion polymer batteries in series providing 7.4 V at 2000 mAh. This enabled the transmitter to interface with sensor nodes without requiring power.

A.3.2 Receiver

The embedded receiver consists of a photodiode followed by a transimpedance amplifier, a variable gain amplifier, and an analog to digital converter (ADC). The output of the ADC is fed

in to an FPGA, of the same type as used at the transmitter. The ADC operates at 100 MSps, which provides a 20X oversampling for the incoming data which is at 5 Mbps.

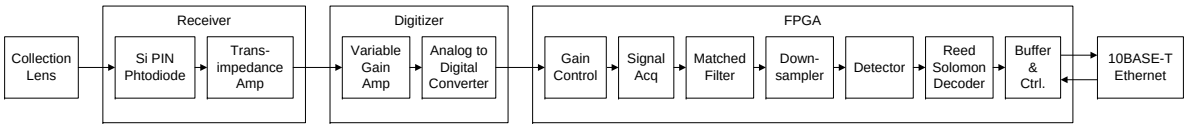

Figure A.5: Block Diagram of Receiver.

The receiver FPGA performs five important operations in sequence: A matched filter, synchronizer, downsampler, detector, and decoder. First, the matched filter is used to maximize the signal-to-noise ratio of the received data by correlating a square pulse with received pulse sequence. A symbol synchronizer then finds the optimal point to downsample the signal, followed by a thresholding detector. The detected bits are then sent to a Reed-Solomon decoder, which corrects detected errors in the data. The output data is piped out through an ethernet port. A block diagram of the receiver architecture is given in Figure A.5.

The entire receiver is powered using a single battery array consisting of two lithium-ion polymer batteries in series providing 7.4 V at 2000 mAh. Similar to the transmitter, this allows the receiver to be self-powered and only requires an ethernet connection to the interfacing device.

A.3.3 Reed-Solomon Error Correction Coding

Although more modern and efficient low-density parity-check (LDPC) codes and turbo codes have been used by the authors in underwater optical links, the Reed-Solomon (RS) code was chosen for its robustness and relative ease of implementation. Altera provides a Reed-Solomon compiler for its FPGAs that was used to generate the Reed-Solomon encoder and decoder used in this project. A RS(255,223) code was ultimately chosen for its low overhead and low resource utilization. It is a systematic code, where 223 data bytes are used to generate 32 parity bytes, which are concatenated at the end of the data to form a 255 byte coded packet. This limits the coding overhead to 1/8, but also limits the number of errors that can be corrected to 16 byte errors. Additional parameter details of this code are given in table A.1. Over a typical underwater link, in which the noise can be modeled as Additive White Gaussian Noise (AWGN), this code provides a 4 dB improvement over the uncoded data at a bit-error-rate of 10^{-5}.

With the 50 byte header attached and with 32 encoded parity bytes, 73 percent of the transmitted packet is data. When not limited by the rate of incoming ethernet data, this would correspond to a data throughput of about 3.65 Mbps when transmitting at 5 Mbps. This is sufficient for video, file transfers and other high bandwidth applications.

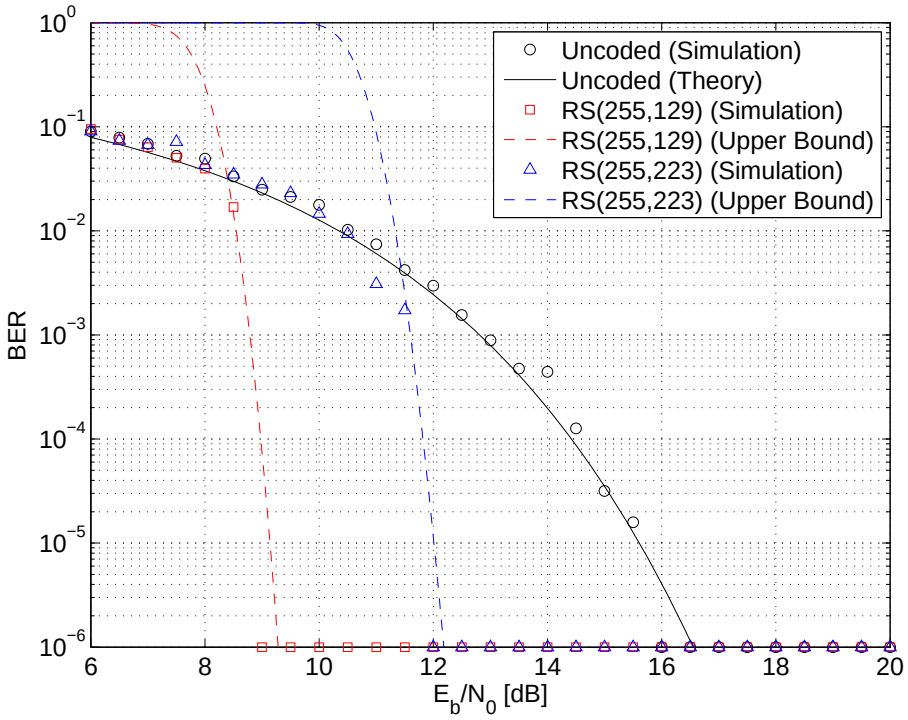

Figure A.6: The expected BER improvements for two Reed-Solomon codes are compared with uncoded performance. At a BER of 10^{-6} the RS (255,129) and RS(255,223) codes provide signal-to-noise ratio advantages of about 6 and 4 dB respectively. Note the points on the x-axis represent error rates that are 0 or less than 10^{-6}.

Table A.1: Summary of parameters for the embedded $\mathcal{C}_{RS}(255, 223)$ RS

Parameter	**Value**
No. of bits per symbol	8
No. of symbols per codeword	255
No. of check symbols per codeword	32
Field polynomial	285
First root of polynomial generator	217
Root spacing in generator polynomial	1

A.3.4 Ethernet Implementation

Ethernet was added to the transmitter and receiver FPGAs to improve its interface compatibility. The FPGA boards do not have a dedicated MAC/PHY chip, but a soft-core was implemented in Verilog on the FPGAs to emulate the minimum functionality. The soft-core also implements the three necessary protocols: Ethernet, IP, and UDP. UDP was chosen for its ease of use and to keep the soft-core complexity minimal. UDP payloads can be as few as 18 bytes to as high as 1500 bytes. However, since every incoming UDP packet is encoded to form a coded RS packet, the UDP payload per ethernet packet is limited and fixed to 223 bytes.

A.3.5 Signal Acquisition

The receiver is constantly sampling the output of the photodiode. However it needs synchronization information regarding the arrival and beginning of a packet to begin processing. The transmitter helps the process by carefully choosing its 50 byte header. The first 25 bytes of this header are non-return-to-zero (NRZ), and the last 25 bytes are return-to-zero (RZ) to match that of the payload. The NRZ pulse widths are thus twice as wide as those of the RZ pulses. Since the modulation depth decreases as a result of modulating the LEDs at 5 Mbps, the wider pulses have a higher intensity than the narrower RZ pulses.

The first 4 bytes of the 25 byte NRZ header is a simple code sequence. The binary version of the sequence is 10010011100111111100111101110010 and is shown in Fig. A.7. The code is rich in ones and, when combined with the higher intensity of the NRZ pulses, is higher in energy.

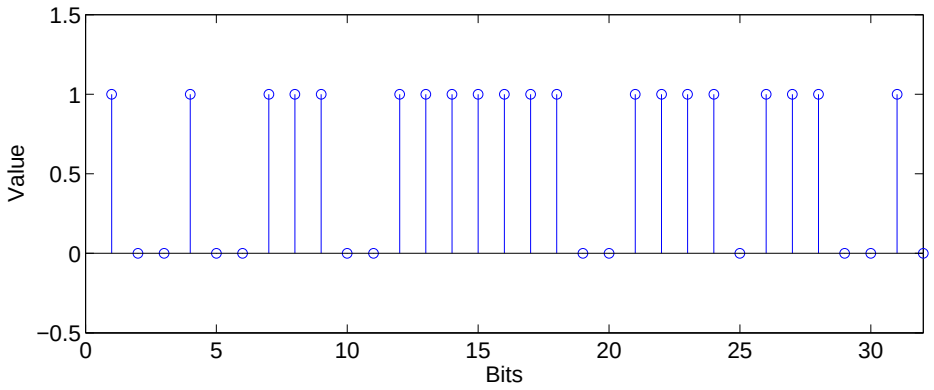

Figure A.7: First 4 bytes of NRZ header.

At the receiver, the code can be easily correlated with to acquire and synchronize the signal. However, the smaller FPGAs used do not have the required number of logic cells to implement

such a correlator. A simple workaround is implemented and described below. When the receiver is at its optimal distance and pointed towards the transmitter, the combined effect of the high energy NRZ header and the code rich in ones results in a long saturated sequence of ones corresponding to the 7 ones in the middle of the code. The receiver takes advantage of this unique pattern to synchronize. Once the receiver has acquired the signal, it looks at the next 21 bytes of the NRZ header, which is a pattern where each byte is 7 zeros followed by a one. This allows the receiver to synchronize to the start of each byte transmitted.

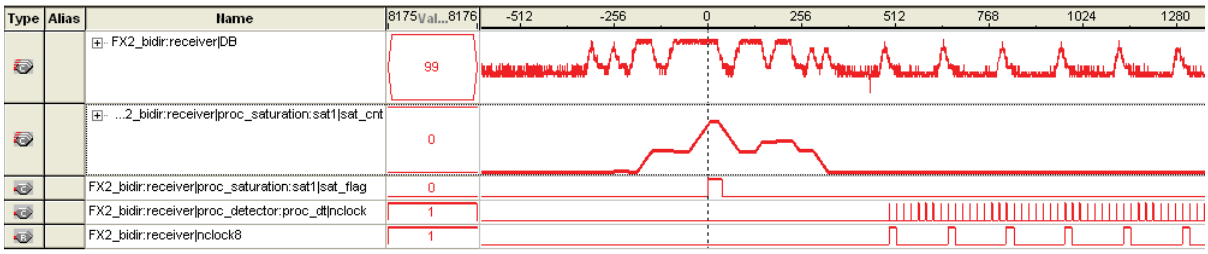

Figure A.8: Signal acquisition and clock and byte recovery. Top trace is received data from the photodiode.

The last 25 bytes of the header is a RZ sequence of ones and zeros. This allows the receiver front-end to settle to the DC level of the payload.

A.4 Low-cost Packaging

The transmitter and receiver are packaged in separate threaded-collar, molded-plastic enclosures. The transmitter is approximately 3" in diameter and 9" long. The front of the transmitter has a dome window with a LED collimation lens inside. The back window of the transmitter consists of a Fischer underwater connector for ethernet and an underwater switch to power the transmitter on and off. The switch is a DPDT switch and controls both the electronics and LED batteries.

The receiver is approximately 6" in diameter and 9" long. The receiver requires the larger size to house the larger 2" light collecting lens in the front. Similar to the transmitter, the back window of the receiver has a Fisher underwater connector for ethernet and a switch to power the receiver on and off.

Figure A.9: Transmitter packaged in a 3 inch diameter, 9 inch long threaded-collar, molded-plastic enclosure.

Figure A.10: Inside the packaged transmitter. Custom-built circuit boards house LED, drivers, FPGA, and ethernet interface.

Figure A.11: Front view of receiver packaged in a 6 inch diameter, 9 inch-long threaded-collar, molded-plastic enclosure.

Figure A.12: Back view of packaged receiver showing fischer underwater connector used for ethernet interface and power switch.

A.5 Testing on an underwater vehicle and Conclusion

Initial tests of the system were conducted in a laboratory water tank 12 ft. long, 4 ft. wide, 4 ft. tall. The system was also tested in a larger 25 ft. long water tank. Mobile tests were conducted on an underwater vehicle in a swimming pool.

Seawolf III, a competition autonomous underwater vehicle (AUV) was used for this purpose. The AUV is approximately 2 ft. wide, 4 ft. long and 1.5 ft. tall and is built on an 80/20 frame platform that enables the vehicle to be easily customized for different payloads. Propulsion is provided by two downward-pointing thrusters, two backward-pointing thrusters, and a strafing thruster. The electronics and battery are housed in a waterproof Pelican case. Computation is provided by a netbook PC which interfaces with the hardware through peripheral boards. The AUV gets its sensor information from an IMU, depth sensor, two cameras, and an acoustic array.

For our experiments, the transmitter is mounted on the vehicle and the receiver is placed at a fixed position in the pool. The transmitter interfaces with the vehicle ethernet through an ethernet switch inside the vehicle. A C program within the vehicle sends predefined UDP packets through the optical transmitter. The packets received by the optical receiver are sent to a PC that compares the data with the transmitted data.

During the test, the receiver was able to successfully receive error-free packets from the transmitter when the vehicle was oriented towards the receiver. This link was tested as far as either end of the pool, at a distance of ~ 24 yards. The test was a success, but it demonstrated some challenges of a system operating with limited field of view. Further tests need to be conducted to validate the performance of the system in less-than-optimal water conditions.

Beyond the limited field of view, the system also had challenges resulting from the small size of the FPGA. The Altera Cyclone II EP2C5 FPGA being used had 4,608 logic elements. An FPGA with a higher number of gates, would allow for: At the receiver:

- A better Reed-Solomon code, preferably an RS(255,129)
- Signal Acquisition to be improved by using a true correlator
- Signal detection and thresholding to be improved using larger averages and bin sizes for threshold calculations
- Current buffering amounts limit the UDP packet size to be no larger than the data size in one Reed-Solomon packet (223 bytes). However, UDP packets can have a payload size as high as 1500 bytes. A larger FPGA would allow better buffering to allow the use of UDP packets much larger than Reed-Solomon packet sizes.

A 5 Mbps embedded, real-time optical communication system with error-control coding for underwater vehicles and sensor nodes to offload information to the external world was

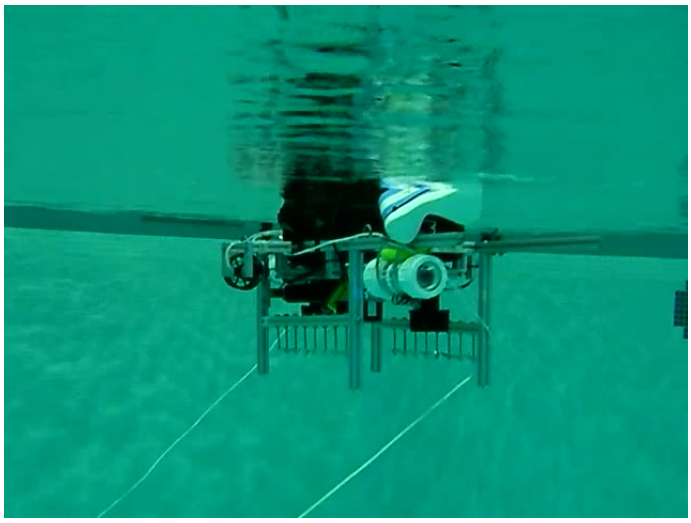

Figure A.13: Transmitter on the unmanned underwater vehicle (UUV) Seawolf III during pool test. During this test, the UUV was remotely operated and controlled to maneuver in different patterns. The patterns included 1) maintaining roll, pitch and yaw (pointed towards the receiver) while it dived, 2) maintaining roll, pitch and depth (at the same height as the receiver) as it changed yaw, and 3) maintaining roll, pitch, yaw, and depth as the UUV moved towards the receiver.

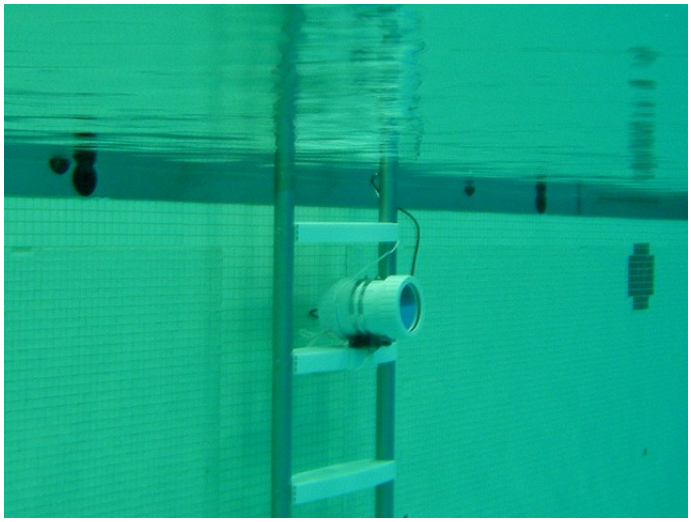

Figure A.14: Receiver mounted at pool side during pool test. During the test, the receiver was able to successfully receiver error-free packets from the transmitter when the vehicle was oriented towards the receiver (i.e., within the field of view of the receiver). This link was tested as far as either end of the pool, at a distance of up to ~ 24 yards.

implemented. The system is improved from previous versions with the addition of digital signal processing techniques including error correction coding. A small, low-cost packaging of the system has been demonstrated in laboratory underwater environments in 3- and 7- meter tanks. The system was also mounted on an unmanned underwater vehicle and communication the link tested in a swimming pool environment. Error-free data packets were successfully received from the vehicle at distances up to 22 m, the total length of the pool. Tests were conducted at data rates of 5 Mbps. Future work includes testing the system in natural waters and investigating the use of more sophisticated coding schemes, and improving the field of view of the system.